DESIGN OF A NOVEL SOUND INSULATION STRUCTURE INCORPORATING QUASI-ZERO STIFFNESS AND VACUUM CAVITY

by
Ahmet Alperen Çakmak
B.S., Mechanical Engineering, Istanbul Technical University, 2020

Submitted to the Institute for Graduate Studies in
Science and Engineering in partial fulfillment of
the requirements for the degree of
Master of Science

Graduate Program in Mechanical Engineering
Boğaziçi University
2024

ACKNOWLEDGEMENTS

I would like to thank my thesis supervisor Prof. Çetin Yılmaz for his guidance and kindness. His help and ideas have been crucial to overcoming faced challenges and perfecting the study. I would also like to thank my colleagues in Bias Mühendislik for providing me the necessary engineering tools and flexibility to pursue this study.

Finally, I would like to thank my family and friends for their love and support. I am grateful for being able to share this achievement with them.

ABSTRACT

DESIGN OF A NOVEL SOUND INSULATION STRUCTURE INCORPORATING QUASI-ZERO STIFFNESS AND VACUUM CAVITY

This thesis focuses on a novel sound insulation structure design. Existing sound insulation methods in the literature have been examined, their strengths and weaknesses have been identified. For the especially challenging low frequency sound insulation problem, a sound insulation structure incorporating quasi – zero stiffness and vacuum (impedance mismatch) has been designed.

The potential improvements of low stiffness and vacuum have been studied. Analytical solutions for sound insulation barriers have been studied. The effects of lowered stiffness and impedance mismatch on sound transmission loss performance have been investigated. Finite element analyses were carried out to obtain the potential of the proposed design. Literature research has determined the improvement rates achieved with these methods in the present day. Exceptional improvement potential in low-frequency sound insulation have been observed and the objectives of the study have been defined.

Designs incorporating low stiffness and vacuum have been developed. Finite element analyses and optimization studies have been carried out to achieve high sound transmission loss at low frequencies. Transmission loss measurements of prototypes with different vacuum ratios and stiffnesses have been carried out. The experimental results of the designed structures have been compared with finite element analyses. The potential improvements and limitations have been discussed.

ÖZET

VAKUM BOŞLUĞU VE YARI-SIFIR DİRENGENLİĞE SAHİP ÖZGÜN BİR SES YALITIM YAPISI TASARIMI

Bu tez çalışmasında özgün bir ses yalıtım yapısı tasarlanmıştır. Ses yalıtımında literatürde kullanılan yöntemler incelenip güçlü ve eksik yönleri belirlenmiştir. Özellikle iyileştirme sağlanamadığı görülen düşük frekans ses yalıtımı problemi için düşük direngenlik ve vakum (empedans uyumsuzluğu) yöntemlerinin uygulanacağı bir ses yalıtım yapısı tasarlanmıştır.

Düşük direngenlik ve vakum yöntemlerinin tasarlanacak yapıda sağlayabileceği iyileştirmeler irdelenmiştir. Ses yalıtım bariyerlerinin analitik çözümleri incelenmiş, eklenecek düşük direngenlik ve empedans uyumsuzluğunun ses iletim kaybı performansına etkileri incelenmiştir. Sonlu elemanlar analizleri ile kavramsal tasarımın potansiyeli elde edilmiştir. Literatür araştırmaları ile söz konusu yöntemler ile günümüzde sağlanan iyileştirme oranları belirlenmiştir. Özellikle düşük frekans ses yalıtımı alanında fevkalade iyileştirme yapılabileceği görülmüş ve çalışma sonucu hedefleri değerleri belirlenmiştir.

Düşük direngenlik ve vakum yöntemlerinin beraber kullanılabileceği tasarımlar geliştirilip düşük frekanslarda yüksek ses iletim kaybı elde edebilmek için sonlu elemanlar analizleri ve eniyileme çalışmaları yapılmıştır. Farklı vakum oranlarında ve direngenliklerde prototipler üretilip ses iletim kaybı testleri gerçekleştirilmiştir. Tasarlanan özgün yapıların deneysel ses iletim kaybı sonuçlarıyla sonlu elemanlar analiz sonuçları karşılaştırılmıştır. Geliştirilen tasarımların kısıtları ve olası iyileştirmeler paylaşılmıştır.

TABLE OF CONTENTS

ACKNOWLEDGEMENTS iii
ABSTRACT iv
ÖZET v
LIST OF FIGURES vii
LIST OF TABLES xiii
LIST OF SYMBOLS xiv
LIST OF ACRONYMS/ABBREVIATIONS xvi
1. INTRODUCTION 1
1.1. Literature Review 1
1.2. Research Objective and Motivation 7
2. ANALYTICAL STUDIES 8
2.1. Fundamental Acoustic Concepts 8
2.2. Transmission Loss of Solid Barriers 10
2.3. Transmission Loss by Impedance Mismatch 13
2.4. Quasi – Zero Stiffness Mechanisms 15
2.5. Convex Diaphragms 20
3. PROPOSED DESIGN 26
3.1. Acoustic Finite Element Analyses 26
3.1.1. Structurally Uncoupled Double Partition 27
3.1.2. Structurally Coupled Double Partition 32
3.2. Structural Finite Element Analyses 36
3.2.1. Truncated Conical Diaphragm 39
3.2.2. Conical Diaphragm 45
4. EXPERIMENTAL STUDIES 50
4.1. Manufactured Prototypes and Test Setup 50
4.2. Experimental Results and Validation 55
5. CONCLUSION 64
REFERENCES 65
APPENDIX A: SOUND TRANSMISSON LOSS MEASUREMENT CURVES . . . 73

LIST OF FIGURES

Figure 1.1. Sound transmission loss curve through a partition. 2

Figure 1.2. Vacuum insulated glass (VIG) topology. 5

Figure 1.3. Quasi – zero stiffness behavior. 6

Figure 2.1. Mechanical impedance of a mass – spring – damper system. 8

Figure 2.2. Sound transmission to the adjacent media. 9

Figure 2.3. Sound transmission through a partition. 10

Figure 2.4. Transmission loss of a partition - mass law (7.8 kg/m2 mass per unit area). 11

Figure 2.5. Sound transmission through a partition with stiffness. 12

Figure 2.6. Transmission loss - stiffness comparison. 13

Figure 2.7. Sound transmission through cavity with impedance mismatch. 14

Figure 2.8. Transmission loss – cavity pressure comparison. 15

Figure 2.9. Displacement transmissibility in a 1 degree of freedom system. 16

Figure 2.10. Lumped quasi – zero stiffness mechanism model. 17

Figure 2.11. Reaction forces of a tuned quasi – zero stiffness mechanism. 18

Figure 2.12. Stiffness of a tuned quasi – zero stiffness mechanism. 19

Figure 2.13. Quasi – zero stiffness mechanism parametric stiffness. 20

Figure 2.14. Pressure loaded convex diaphragms: (a) conical, (b) spherical. 20

Figure 2.15. Pressure – displacement curve of conical diaphragms for various convexity ratios. 21

Figure 2.16. Pressure – displacement curve of spherical diaphragms for various convexity ratios. 22

Figure 2.17. Conical diaphragm pressure – displacement curve. 22

Figure 2.18. Spherical diaphragm pressure – displacement curve. 23

Figure 2.19. Conical diaphragm s=0.700 mm – analysis/mathematical solution comparison. 24

Figure 2.20. Conical diaphragm s=0.777 mm – analysis/mathematical solution comparison. 24

Figure 2.21. Conical diaphragm s=0.800 mm – analysis/mathematical solution comparison. 25

Figure 3.1. Acoustic model for transmission loss analyses. 27

Figure 3.2. Mode shapes of the uncoupled partition, (a) 1st mode shape (0,1), (b) 2nd mode shape (1,1), (c) 3rd mode shape (2,1), (d) 4th mode shape (0,2). 29

Figure 3.3. Uncoupled partition – transmission loss of original plate with 1 atm and 0.2 atm cavity pressure. 30

Figure 3.4. Uncoupled partition – transmission loss of original plate with 1 atm cavity pressure and quasi-zero stiffness plate with 1 atm cavity pressure. 31

Figure 3.5. Uncoupled partition – transmission loss of original plate with 1 atm cavity pressure and zero stiffness plate with 0.2 atm cavity pressure. . 31

Figure 3.6. Mode shapes of the coupled partition, (a) 1st mode shape (0,1– OP), (b) 2nd mode shape (0,1– IP), (c) 3rd mode shape (1,1), (d) 4th mode shape (2,1), (e) 5th mode shape (0,2 – OP), (f) 6th mode shape (0,2 – IP). 33

Figure 3.7. Coupled partition – transmission loss of original plate with 1 atm and 0.2 atm cavity pressure. 34

Figure 3.8. Coupled partition – transmission loss of original plate with 1 atm cavity pressure and quasi-zero stiffness plate with 1 atm cavity pressure. 35

Figure 3.9. Coupled partition – transmission loss of original plate with 1 atm cavity pressure and quasi-zero stiffness plate with 0.2 atm cavity pressure. 36

Figure 3.10. Snap through behavior of buckled structure. 38

Figure 3.11. General view of the truncated conical diaphragm. 40

Figure 3.12. Truncated conical diaphragm dimensions. 40

Figure 3.13. Effect of diaphragm thickness on pressure – displacement curve of truncated conical diaphragm for h=2.1 mm and ri=25 mm. 41

Figure 3.14. Effect of apex height on pressure – displacement curve of truncated conical diaphragm for s=0.55 mm and ri=25 mm. 41

Figure 3.15. Effect of inner radius on pressure – displacement curve of truncated conical diaphragm for s=0.55 mm and h=2.1 mm. 42

Figure 3.16. Natural frequencies with incremental pressure loading (96.5% vacuum; 63 Hz, 550.3 Hz, 1508.5 Hz). 43

Figure 3.17. Max von Mises stress with incremental pressure loading (96.5% vacuum; 408.1 MPa). 43

Figure 3.18. Von Mises stresses of the critically loaded truncated conical diaphragm. 44

Figure 3.19. Mode shapes of the critically loaded truncated conical diaphragm, (a) 1st mode shape, (b) 2nd mode shape, (c) 3rd mode shape, (d) 4th mode shape, (e) 5th mode shape, (f) 6th mode shape. 44

Figure 3.20. Conical diaphragm general view. 45

Figure 3.21. Conical diaphragm dimensions. 46

Figure 3.22. Effect of diaphragm thickness on pressure – displacement curve of conical diaphragm for h=1.8mm. 46

Figure 3.23. Effect of diaphragm apex height on pressure – displacement curve of conical diaphragm for s=0.7mm. 47

Figure 3.24. Natural frequencies with incremental pressure loading (86% vacuum; 117.6 Hz, 1013.5 Hz, 2098.6 Hz). 48

Figure 3.25. Max von Mises stress with incremental pressure loading (86% vacuum; 298.3 MPa). 48

Figure 3.26. Von Mises stresses of the critically loaded conical diaphragm. 49

Figure 3.27. Mode shapes of the critically loaded conical diaphragm, (a) 1st mode shape, (b) 2nd mode shape, (c) 3rd mode shape, (d) 4th mode shape, (e) 5th mode shape, (f) 6th mode shape. 49

Figure 4.1.	Transmission loss measurement test setup.	50
Figure 4.2.	Close up view of Specimen 1 showing the conical shape of the diaphragm.	51
Figure 4.3.	Manufactured specimens left to right: 1, 2, 3, (a) assembled specimens, (b) disassembled specimens (top views) (c) disassembled specimens (bottom views).	52
Figure 4.4.	(a) Vacuum setup, (b) specimen vacuum application.	54
Figure 4.5.	Deformation under vacuum, (a) maximum vacuum (95%), (b) critical vacuum (70%).	54
Figure 4.6.	Specimen fitting in impedance tube sample holder.	55
Figure 4.7.	Transmission loss measurement – averaging.	56
Figure 4.8.	Transmission loss measurement – amplifier gain setting.	57
Figure 4.9.	Transmission loss measurements of Specimen 1.	58
Figure 4.10.	Transmission loss measurements of Specimen 2.	59
Figure 4.11.	Transmission loss measurements of Specimen 3.	60
Figure 4.12.	Specimen 1 – FE transmission loss analyses.	61
Figure 4.13.	Specimen 1 no vacuum transmission loss – analysis/measurement comparison.	62
Figure 4.14.	Specimen 1 critical vacuum transmission loss – analysis/measurement comparison.	62

Figure 4.15. Specimen 1 full vacuum transmission loss – analysis/measurement comparison. 63

Figure A.1. Transmission loss measurements of Specimen 1 – no vacuum. 73

Figure A.2. Transmission loss measurements of Specimen 1 – critical vacuum. . . 73

Figure A.3. Transmission loss measurements of Specimen 1 – full vacuum. 74

Figure A.4. Transmission loss measurements of Specimen 2 – no vacuum. 74

Figure A.5. Transmission loss measurements of Specimen 2 – critical vacuum. . . 75

Figure A.6. Transmission loss measurements of Specimen 2 – full vacuum. 75

Figure A.7. Transmission loss measurements of Specimen 3 – no vacuum. 76

Figure A.8. Transmission loss measurements of Specimen 3 – critical vacuum. . . 76

Figure A. 9. Transmission loss measurements of Specimen 3 – full vacuum. 77

LIST OF TABLES

Table 3.1. Natural frequencies & mode shapes of the uncoupled partition. 29

Table 3.2. Natural frequencies & mode shapes of the coupled partition. 33

Table 4.1. Specimen dimensions. 52

LIST OF SYMBOLS

c	Viscous damping coefficient
c_0	speed of sound in air
c_n	speed of sound in medium *n*
E	Young's modulus
$f_{0,n}$	n^{th} cavity resonance frequency
f_p	Fundamental resonance frequency of partition
F	Force
$F_{v,v}$	Vertical component of vertical spring force
$F_{i,v}$	Vertical component of inclined spring force
F_r	Total reaction force
h	Height
j	Imaginary unit number
k	Linear spring stiffness
k_i	Inclined spring stiffness
k_t	Total stiffness
k_v	Vertical spring stiffness
L_v	Initial length of the vertical spring
L_i	Initial length of the inclined springs
m	Mass
m_s	Surface mass
n	Positives integers
p_i	Incident wave sound pressure
p_r	Reflected wave sound pressure
p_t	Transmitted wave sound pressure
P	Distributed pressure load
P_i	Sound pressure magnitude of incident wave
P_r	Sound pressure magnitude of reflected wave
P_t	Sound pressure magnitude of transmitted wave
r	Radius

r_i	Inner radius
r_ω	Ratio of excitation frequency to natural frequency
R	Sound reflection coefficient
s	Thickness
t	Time
T	Sound transmission coefficient
TL	Sound transmission loss
u_i	Incident wave particle velocity
u_r	Reflected wave particle velocity
u_t	Transmitted wave particle velocity
w	Width
x	Output displacement
X	Output displacement amplitude
y	Input displacement
y_0	Displacement of diaphragm center
Y	Input displacement amplitude
z	Mechanical impedance
z_0	Specific acoustic impedance of air
z_n	Specific acoustic impedance of medium "*n*"
z_w	Mechanical impedance of single partition
ζ	Damping ratio
η	Ratio of height to width of quasi-zero stiffness mechanism
ρ_0	Density of air
ρ_n	Density of medium *n*
τ	Sound power transmission coefficient
ω	Angular frequency
ω_n	Natural frequency of 1DOF system

LIST OF ACRONYMS/ABBREVIATIONS

EPDM	Ethylene propylene diene monomer
FE	Finite element
HVAC	Heating, ventilation and air conditioning
IP	In phase
LSG	Laminated safety glass
OP	Out of phase
VIP	Vacuum insulated panel
VIG	Vacuum insulated glass

1. INTRODUCTION

The oscillations of a physical system around an equilibrium point are defined as vibrations. Once the vibration motion is translated to fluid particle domain, the discipline of acoustics arises which explain the creation and propagation of the sound waves we hear. Acoustic insulation has been a widely investigated topic among engineers for health and comfort reasons [1]. Engineering solutions for acoustic insulation problems require a holistic approach, examining the deeply related disciplines of vibration and acoustics [2]. In order to have an effective acoustic isolation system, both air-borne and structure-borne sound should be eliminated. Sound cannot travel in vacuum, so it can eliminate air-borne sound. However, vacuum should be contained in a structure or container and structure-borne sound can propagate through the container. To minimize structure-borne sound, a novel quasi-zero-stiffness vacuum container will be proposed.

1.1. Literature Review

Sound insulation, also known as acoustic isolation or soundproofing, is the practice of reducing the transmission of sound from one space to another. It involves the use of various materials, techniques, and manufacturing methods to minimize the impact of noise. The primary goal of sound insulation is to create quieter and more comfortable environments by reducing noise levels and preventing sound from traveling between spaces. Different materials and techniques are used to address airborne sound transmission, such as acoustic absorbers and barriers, while mitigating structure-borne sound transmission often requires damping and decoupling techniques.

Effectiveness of sound insulation is measured by different metrics, yet the main principle is similar in which the ratio of input to the output sound pressure or power levels are compared. Insertion loss is defined by the ratio of sound pressure level monitored with and without a sound insulation treatment present. Insertion loss index method is generally used in measurements of duct/pipe systems such as silencers [3, 4]. Partitions and building components on the other hand, can be investigated by sound reduction index metric in field measurement conditions [5]. For such partitions, laboratory measurements such as

impedance tube or two room methods exist. Impedance tube measurements can be employed to obtain the characteristic impedance and absorption coefficients of compatible specimens [6, 7]. Transmission loss can then be calculated, which is the ratio of incident and transmitted sound power levels of the specimen of interest. Compatibility restriction for the impedance tube method is that the specimens must comply with the geometry and size constrictions of the measuring apparatus. In the case of specimens of large size, two room measurements can be utilized [8, 9]. Similar with the impedance tube measurements, transmission loss can be calculated via the two room methods. The computed metrics for impedance tube measurements are limited to plane wave excitation while two room methods can capture the insulation performance under diffuse field excitations. Acoustic transmissibility of building components can also be measured by sound intensity [10]. Yet this method is often not favored upon the mentioned measurement methods.

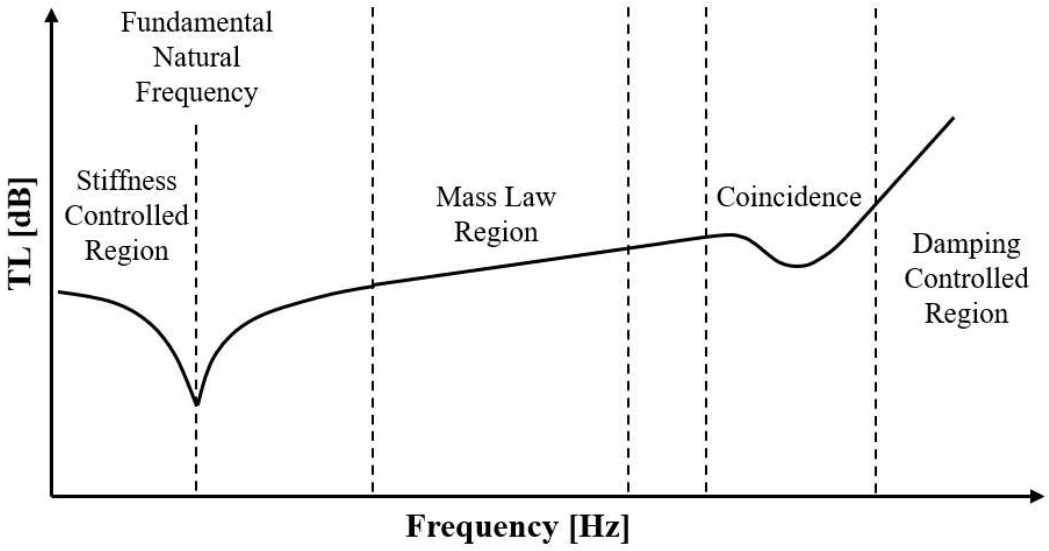


Figure 1.1. Sound transmission loss curve through a partition.

Transmission loss of a typical insulation partition is given in Figure 1.1. Three regions where different mechanisms rule over exists [11]. Low frequency region is mostly influenced by the structural response of the partition. For a solid partition, first natural frequency lies in this low frequency region. Acoustic excitations matching the first natural frequency resonates the whole partition, which decreases the insulation significantly. A solid partition can have several resonance frequencies in the low frequency region. For the frequency region above the resonant frequencies, insulation characteristics mainly rely on

mass per unit area of the partition. Acoustic insulation of a partition in this region is represented by the “mass law”. The transmission loss value increases by six dB with doubling of mass per unit area or frequency. Mass controlled region is followed by a strong dip. This is known as the “coincidence dip” and occurs due to matching wavelengths of the incident acoustic wave with the bending wave of the partition [12]. Damping property of the partition controls both the depth of this dip and transmission loss on higher frequencies. Damping also affects the sharpness of resonances in the lower frequency region.

Conventional sound reduction practices consist of heavy mass layers, damping on vibrating surfaces, and integration of absorbent materials. Adding mass to the partition reduces sound transmission through a wide range of frequencies. For building applications, mass loading can be practiced either on the entire partition or locally. Yet the physical and economic challenges of building massive partitions limit the insulation to be gained.

Using damping materials contributes to the acoustic insulation by reducing transmission due to structural responses, i.e., smaller the structural response, smaller the structure borne noise transmitted to the receiver. Damping treatments for acoustic insulation are most effective for thinner/less bulky sound barrier structures. Peak transmissibility value caused by resonance is mainly influenced by the added damping [13]. Such treatments as damping pads are used on drywalls, automotive sheet metal body parts, HVAC systems, pipelines etc. Implementing damping can also be achieved by creating a constrained layer damping. Laminated structures provide enhanced insulation capabilities compared to simple damping layer applications [14]. Since the transmission behavior of partitions rely mostly on mass effects, laminated panel applications are limited to thin plates, improving the insulation, which is only mediocre.

Absorbent materials that dissipate energy from sound waves through acoustic absorption is another treatment widely used. Sound absorbing practices can be investigated in categories of porous materials and resonator applications [15]. Sound absorbing treatments consist of closed foams like EPDM, neoprene and porous open cell foams like polyurethane foam, open cell rubber. Porous materials contribute to insulation by converting the input energy into heat energy. Sound absorbing materials can be utilized as in coating and panel fashion to reduce reverberation of cavities [11]. Porous materials are also used as

filling between partitions to enhance insulation [16, 17]. Even though sound absorbing materials operate fairly in mid to high frequencies, low frequency absorption performance remains insufficient [18]. Resonator treatments are used in conjunction to improve the low frequency attenuation performance. Resonators contribute to energy dissipation by increasing the oscillations locally at tuned frequencies, creating amplified losses. Typical applications range from micro perforated panels, Helmholtz resonators and labyrinth alike structures [19-21].

Different topologies for better performing sound isolation partitions have been researched extensively. Sandwich panel structure, which consists of two "skins" and a "core", are studied for their acoustic isolation capabilities. The idea of multilayered sound barrier in a sandwich structure fashion goes back to 1950's. G. Kurtze and B.G. Watters have examined a sandwich panel where the skins have much higher Young Modulus compared to the core and derived its total impedance [22]. J.A. Moore and R. H. Lyon have investigated sound transmission loss characteristics of different panel constructions. They have employed horizontal honeycomb patterns as the core, which lowered the wall resonance frequency and improved isolation performance [23]. The main challenge is to overcome the mass law limitation with relatively low density panel and unique designs [24]. Configurations with nonconventional face sheets and core materials are investigated [25, 26]. Sandwich panels with unique core patterns are also studied extensively [27, 28].

The difference in specific acoustic impedances, called "impedance mismatch" provide higher reflection and lower transmission. Since vacuum ideally has the specific acoustic impedance of zero, it holds great performance for sound insulation. Despite the physical challenges of creating and holding vacuum in an enclosed volume, there are several products such as "Vacuum Insulated Panels (VIP)" and "Vacuum Insulated Glass (VIG)" where vacuum is utilized to enhance insulation properties. Even though the main objective of such designs is to provide heat insulation, their sound insulation properties are also of interest.

The patent history of vacuum sealing goes back to early 1900's, yet the first scientific report on production of a vacuum glazing was published by in 1989 [29]. Since then, VIG's have become commercially available. The ISO 19916-1:2018 standard [30] has been

developed for evaluation of heat and sound insulation properties. In terms of sound insulation, VIG's do not offer substantial performance. To be more specific, it is found that both single pane, laminated safety glass (LSG) and VIG having the same mass per unit area yield similar sound reduction in the middle frequency range (250-1000 Hz). These results also match the mass law, meaning that the existence of vacuum gap does not contribute to insulation [31]. Such results can be attributed to the pillars between the glasses to ensure structural integrity shown in Figure 1.2. These pillars are the structural supports that help layers support the atmospheric pressure, but also contributing to coupling of the two layers. Since such structural coupling reduces the sound insulation ability greatly, this example illustrates the structural challenge of integrating vacuum in an insulation design [32-34].

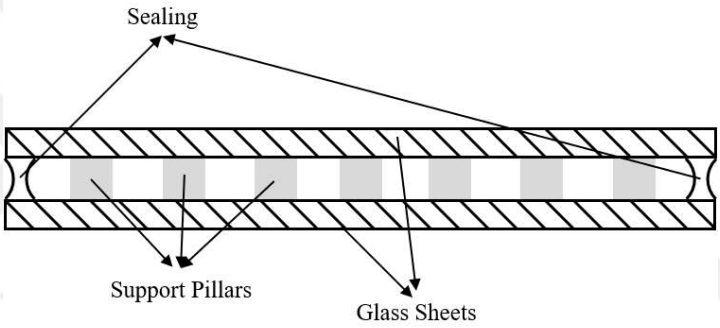


Figure 1.2. Vacuum insulated glass (VIG) topology.

VIP technology mainly aims to reduce the thermal losses in residential applications. The topology consists of a core material such as fumed silica powder, enclosed by a multi-layer envelope film and evacuated gas pressure to a few mbars. VIP's have successfully satisfied low thermal conductivity while reducing the thickness of the insulation layer. Yet the studies conducted reveal that the sound reduction of VIP's are moderate, being limited to the mass law [35, 36].

Aside from the commercialized products, there have been studies on different topologies of sound insulation systems. Considering the level of vacuum, it is found that internal pressure down to 20 kPa (80% vacuum) is required to achieve an audible difference [37]. Such determination relies on the reflection/transmission coefficient calculation. Another outcome of the study, which has already been discussed, is the supports between the layers contributing to structural coupling and reducing the sound insulation. It is challenging to design a vacuum enclosure without structural coupling that can withstand the

external pressure load due to the vacuumed cavity. There are a couple of patents on vacuum holding isolation structures, but none are supported by engineering studies [38, 39].

Quasi – zero stiffness mechanisms, which are pursued in this thesis, provide near zero stiffness at a predetermined load condition. First studies on quasi – zero stiffness mechanisms date back to 1950's for vibration isolation [40]. This non – linear stiffness behavior is presented in Figure 1.3. Quasi – zero stiffness mechanisms can be achieved by properly managed linear spring elements and tuned to have desired stiffness properties. The mathematical models show that to have near zero stiffness, the acting negative and positive stiffness must be in equilibrium at a given displacement/force level [41]. Arrangements can be made by implementing appropriate elements for the required negative and positive stiffness contributions. Using compliant parts such as buckled beams, leaf springs for negative stiffness in conjunction with linear elastic parts for positive stiffness has been shown to be a successful application [42, 43].

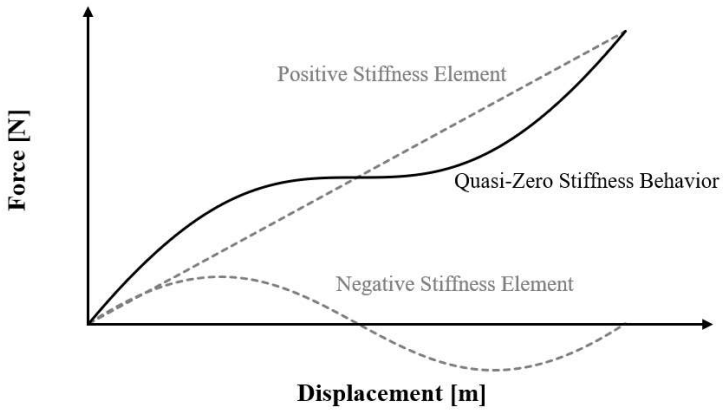


Figure 1.3. Quasi – zero stiffness behavior.

Quasi – zero stiffness vibration isolation mechanism has been worked on by a variety of researchers for vibration isolation [44-47]. These mechanisms are made up of individual positive and negative stiffness elements, providing support and vibration isolation to mechanical systems [48]. Koçak and Yılmaz successfully designed a vibration isolation mechanism based on quasi-zero stiffness mechanism [49]. The limitation of a set quasi – zero stiffness level was overcome by designing the positive and negative stiffness contributing elements with variable properties. Meng et al. have investigated the

implementation of a quasi – zero stiffness mechanism to reduce force transmissibility on robotic applications [50]. These mechanisms reduce vibration response of applied systems shifting the fundamental natural frequency towards lower frequencies whilst maintaining sufficient load bearing capacity.

Quasi – zero stiffness behavior is also practiced in elastic metamaterials. Unit cells of these elastic metamaterials are comprised of either combined or discrete compliant elements which provide positive and negative stiffness to the system. These materials can be used in single and multicellular configurations, offering application flexibility. Zhou et al. have cascaded one dimensional quasi – zero stiffness metamaterials and demonstrated that transmissibility decreases drastically with increased cells employed [51]. Zhang et al. have studied the response of metamaterial assemblies which can be tuned to a desired overall mechanical behavior [52]. Such tuned behavior offers quasi – zero stiffness and low dynamic transmissibility under multiple static load levels. The effect of changing dimensions of a designated quasi – zero stiffness cell was demonstrated by Fan et al. [53].

1.2. Research Objective and Motivation

The aim of is thesis is to design and build a novel sound insulation structure. Various sound insulation practices have been presented. Inertial amplification method has been utilized to achieve low frequency acoustic insulation [54]. Quasi-zero stiffness mechanism has been investigated to achieve low frequency waterborne sound insulation [55]. However, there is no study in the literature that utilizes both vacuum cavity and quasi-zero stiffness to achieve low frequency sound insulation. Vacuum cavity for impedance mismatch has been used in solutions such as VIP, VIG and partitions. Quasi – zero stiffness has been proposed to achieve low frequency sound isolation. In this thesis, these two methods are pursued to be applied together.

The main goal is to achieve exceptional sound transmission loss levels at low frequencies. Quasi – zero stiffness is utilized for lowering the fundamental natural frequency of the system. The impedance mismatch created by vacuum enclosure is expected to provide acoustic insulation above the mass law predictions. The design works with self-help principle [56] where the external pressure load on the system triggers the low stiffness state.

2. ANALYTICAL STUDIES

2.1. Fundamental Acoustic Concepts

Mechanical impedance of a system is defined as the complex ratio of harmonic excitation force amplitude to the complex velocity response of the system. This definition can be simplified by the physical meaning of "the velocity output resulting from a unit force input". A mechanical single degree of freedom system is shown in Figure 2.1.

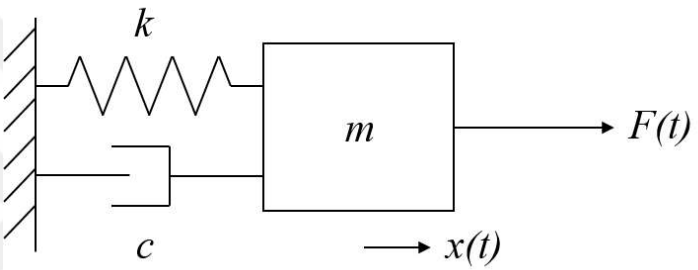


Figure 2.1. Mechanical impedance of a mass – spring – damper system.

The mechanical impedance of a single degree of freedom system is derived as

$$z = c + j(m\omega - k/\omega), \tag{2.1}$$

where m is the mass, k is the linear spring constant, ω is the angular frequency and c is the viscous damping constant. For the given system, mechanical resonance occurs as the imaginary part (reactance) of the impedance cancels out and only the real part (resistance) remains. For such angular frequency, the amplitude of the complex impedance is at absolute minimum [57].

Impedance definition can be applied to continuous systems for wave motion, just as it can be applied to the acoustic propagation. The specific acoustic impedance (characteristic impedance) is defined as the ratio of the sound pressure amplitude to the velocity. For propagating plane waves, the specific acoustic impedance can simply be written as

$$z_0 = \frac{p(x,t)}{u(x,t)} = \rho_0 c_0. \tag{2.2}$$

In acoustic reflection/transmission problems, the two main conditions that need to be satisfied for the two sides of the boundary are

$$u_i(0,t) + u_r(0,t) = u_t(0,t), \tag{2.3}$$
$$p_i(0,t) + p_r(0,t) = p_t(0,t), \tag{2.4}$$

where Equation (2.3) is the continuity of particle velocities and Equation (2.4) is the equality of total pressures (see Figure 2.2).

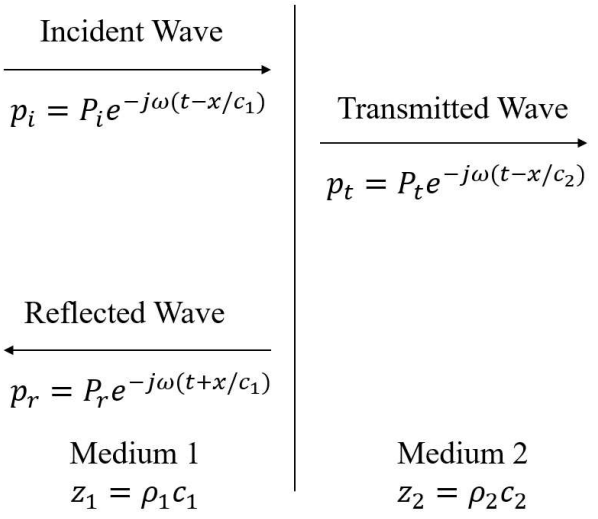


Figure 2.2. Sound transmission to the adjacent media.

The sound pressure and particle velocities can also be expressed by the relation of acoustic impedance as

$$z_1 = \frac{p_i(x,t)}{u_i(x,t)} = -\frac{p_r(x,t)}{u_r(x,t)} = \rho_1 c_1, \tag{2.5}$$
$$z_2 = \frac{p_t(x,t)}{u_t(x,t)} = \rho_2 c_2. \tag{2.6}$$

Equations (2.3-2.6) can be algebraically manipulated to obtain ratios of pressure wave amplitudes which quantify their interaction. Pressure reflection and pressure transmission coefficients can be expressed by

$$R = \frac{p_r(0,t)}{p_i(0,t)} = \frac{P_r}{P_i} = \frac{z_2 - z_1}{z_2 + z_1}, \tag{2.7}$$
$$T = \frac{p_t(0,t)}{p_i(0,t)} = \frac{P_t}{P_i} = \frac{2z_2}{z_2 + z_1}. \tag{2.8}$$

In practice, transmission properties of a medium are defined by the power transmission coefficient given as:

$$\tau = \frac{z_1}{z_2} T^2 = \frac{4 z_2 z_1}{(z_2 + z_1)^2}, \tag{2.9}$$

$$TL = 10 \log \frac{(z_2 + z_1)^2}{4 z_2 z_1}. \tag{2.10}$$

This derivation belongs to the case where the sound wave propagation is normal to the boundary (normal incidence). From Equation (2.10), it can be deduced that greater the difference between impedances of two media, smaller the power transmission coefficient gets. This particular situation is called "impedance mismatch" which grants lower transmission and higher reflection.

2.2. Transmission Loss of Solid Barriers

Sound transmission through a solid can be solved by considering its mass per unit area. The assumption here is that the partition does not have any stiffness. As the incident pressure wave reaches the solid boundary, it harmonically oscillates in the direction of propagation (see Figure 2.3). There forms reflected and transmitted pressure waves. The continuity of pressures on either side of the solid boundary are investigated by Newton's Second Law as

$$(P_i + P_r) - P_t = -m_s \omega^2 Y. \tag{2.11}$$

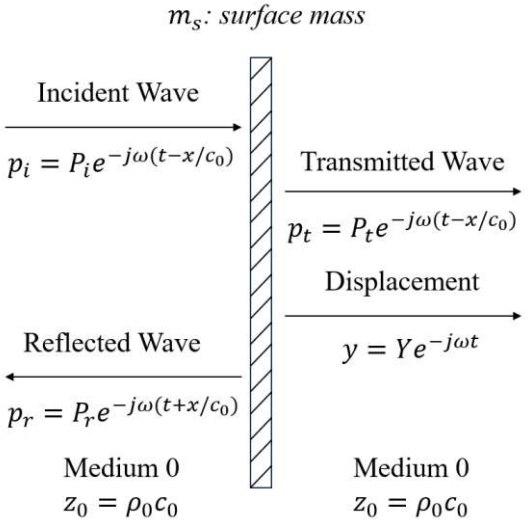


Figure 2.3. Sound transmission through a partition.

The second requirement that is the continuity of velocities can be expressed by the velocity of the solid boundary and velocity of the transmitted wave particle. This requirement is given as

$$\frac{P_t}{z_0} = -j\omega Y. \tag{2.12}$$

From Equation (2.11) and Equation (2.12), pressure transmission coefficient and power transmission coefficient can be derived respectively by

$$\frac{P_t}{P_i} = \frac{2\rho_0 c_0}{-j\omega m_s + 2\rho_0 c_0}, \tag{2.13}$$

$$\tau = \frac{(2\rho_0 c_0)^2}{(\omega m_s)^2 + (2\rho_0 c_0)^2}. \tag{2.14}$$

With the defined power transmission coefficient, transmission loss through a solid boundary can be obtained as [13]

$$TL = 10 \log\left[1 + \left(\frac{\omega m_s}{2\rho_0 c_0}\right)^2\right]. \tag{2.15}$$

Equation (2.15) implies that the sound transmission through a solid is inversely proportional to the mass of the partition and frequency of the excitation. The derived relation is also known as the mass law formula. It is important to point out that all the derived formulations are for the case of normal incidence, which means the propagation of sound waves are in the form of plane waves and normal to the boundary. Transmission loss for normal incidence (0°), field incidence (0° - 78°) and random incidence (0° - 90°) are compared in Figure 2.4 [58].

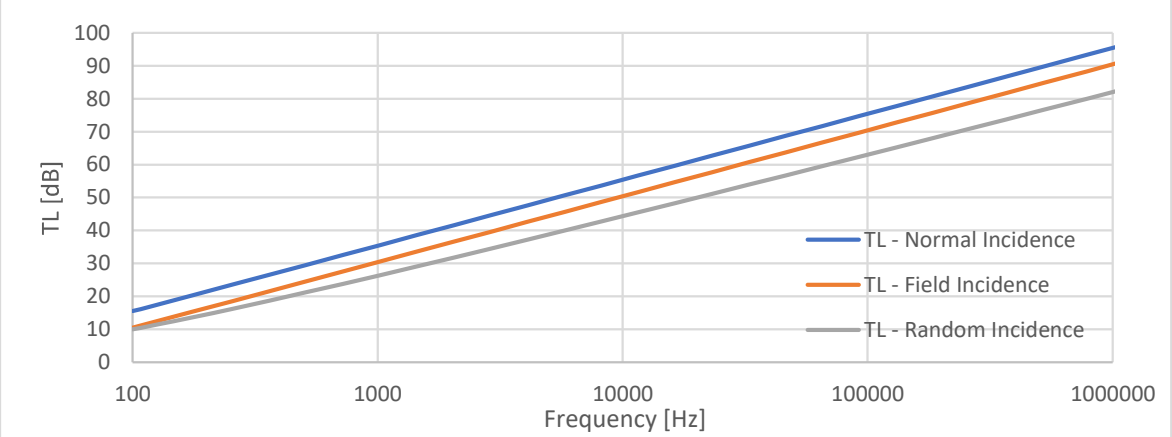


Figure 2.4. Transmission loss of a partition - mass law (7.8 kg/m^2 mass per unit area).

Unlike the previously investigated ideal case, solid boundaries between media such as partitions have stiffness and damping properties. This more general case can be investigated by assuming the partition to be a single degree of freedom system as shown in Figure 2.5. Power transmission coefficient for such partitions can be derived by applying Newton's Second Law as

$$\tau = \frac{(2\rho_0 c_0)^2}{(\omega m_s - k/\omega)^2 + (2\rho_0 c_0 + c)^2}. \tag{2.16}$$

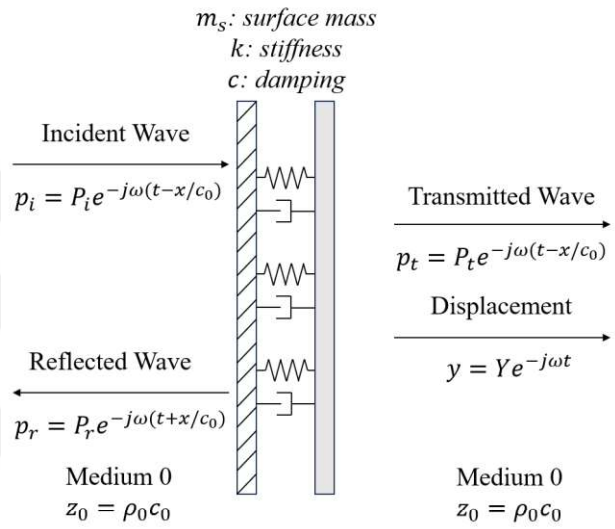


Figure 2.5. Sound transmission through a partition with stiffness.

It can be seen tin Equation (2.16) that there is a single resonance frequency for the single degree of freedom system [13]. The above power transmission coefficient is sufficient to provide insight of transmission behavior of a single panel in low to mid frequencies. The transmission loss curve acquired by the above relation is given in Figure 2.6. At the fundamental resonance frequency "f_p" insulation performance decreases significantly. In Figure 2.6, calculated transmission loss for two plates varying stiffness is shown. The curves are both generated for a partition with density of 7800 kg/m^3 and thickness of 1 mm (7.8 kg/m^2 mass per unit area). The stiffness value of the high stiffness plate was chosen to acquire the first fundamental mode frequency at 1 kHz, which is a good estimate for a 100 mm diameter plate. The low stiffness plate was tuned to have the fundamental frequency at 200 Hz. Transmission loss is higher in the lower stiffness plate after 730 Hz. Hence, once a target frequency is set (e.g. 730 Hz) transmission loss characteristics of a plate can be improved by simply lowering its fundamental frequency. Even though there is only one

resonance frequency in the investigated model, studies indicate that the fundamental natural frequency is the most contributing one to transmission loss [59].

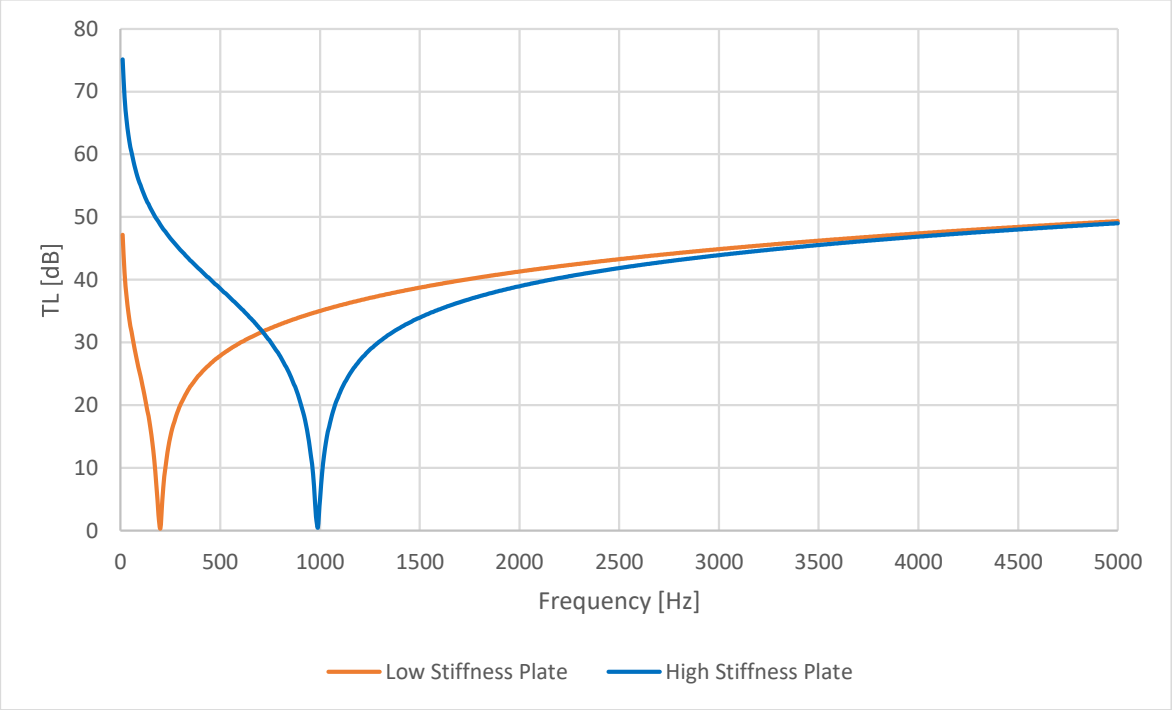


Figure 2.6. Transmission loss - stiffness comparison.

2.3. Transmission Loss by Impedance Mismatch

So far, the sound transmission between adjacent media with different specific acoustic impedances and transmission through a partition has been investigated. The proposed design consists of an enclosed volume acting as a vacuum cavity. Vacuum cavity is employed to utilize impedance mismatch between the incident&transmitted media and the partition media. Such transmission can be examined by the problem of sound travelling through media with different acoustic impedances. In the model given in Figure 2.7, propagating wave travels through the medium 0, passes medium 1 (cavity media) and reaches medium 0 again. The cavity media here presents the vacuumed enclosure with different acoustic impedance than air media. Power transmission coefficient for this model is calculated as

$$\tau = \frac{1}{1 + \frac{1}{4}\left({}^{z_1}/_{z_0} - {}^{z_0}/_{z_1}\right)^2 sin^2\left({}^{\omega}/_{c_0} W\right)}. \tag{2.17}$$

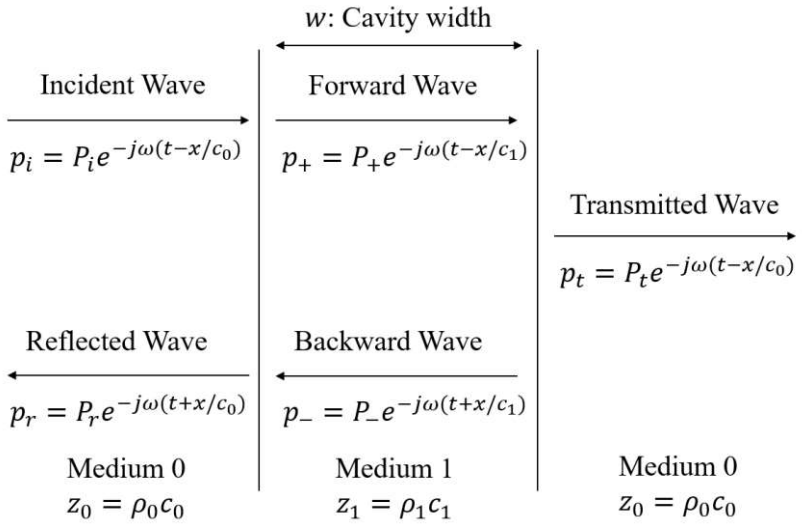


Figure 2.7. Sound transmission through cavity with impedance mismatch.

Equation (2.17) depicts that there are frequencies which the incident energy will be fully transmitted. These excitation frequencies can be called the cavity resonance frequency "$f_{0,n}$". The mathematical expression of cavity resonance frequencies for normally incident excitation is calculated in as

$$f_{0,n} = \frac{c_0}{2w} n. \tag{2.18}$$

Figure 2.8 depicts transmission loss change expected by changing the properties of the cavity medium. The proposed model consists of the air media divided by a 50 mm cavity in between. The absolute pressure of the cavity medium, as explained in Chapter 2, influences the cavity impedance by the change in density. Two major effects are observed by reducing air pressure from 1 atm to 0.01 atm:

- TL enhancement obtained by the added unit vacuum at each step, increases with the increased vacuum level.
- The cavity resonance dip becomes narrower and less significant.

Keeping in mind that given solution completely neglects the structural coupling between partitions, great enhancement is to be expected by maintaining a vacuum cavity between solid partitions.

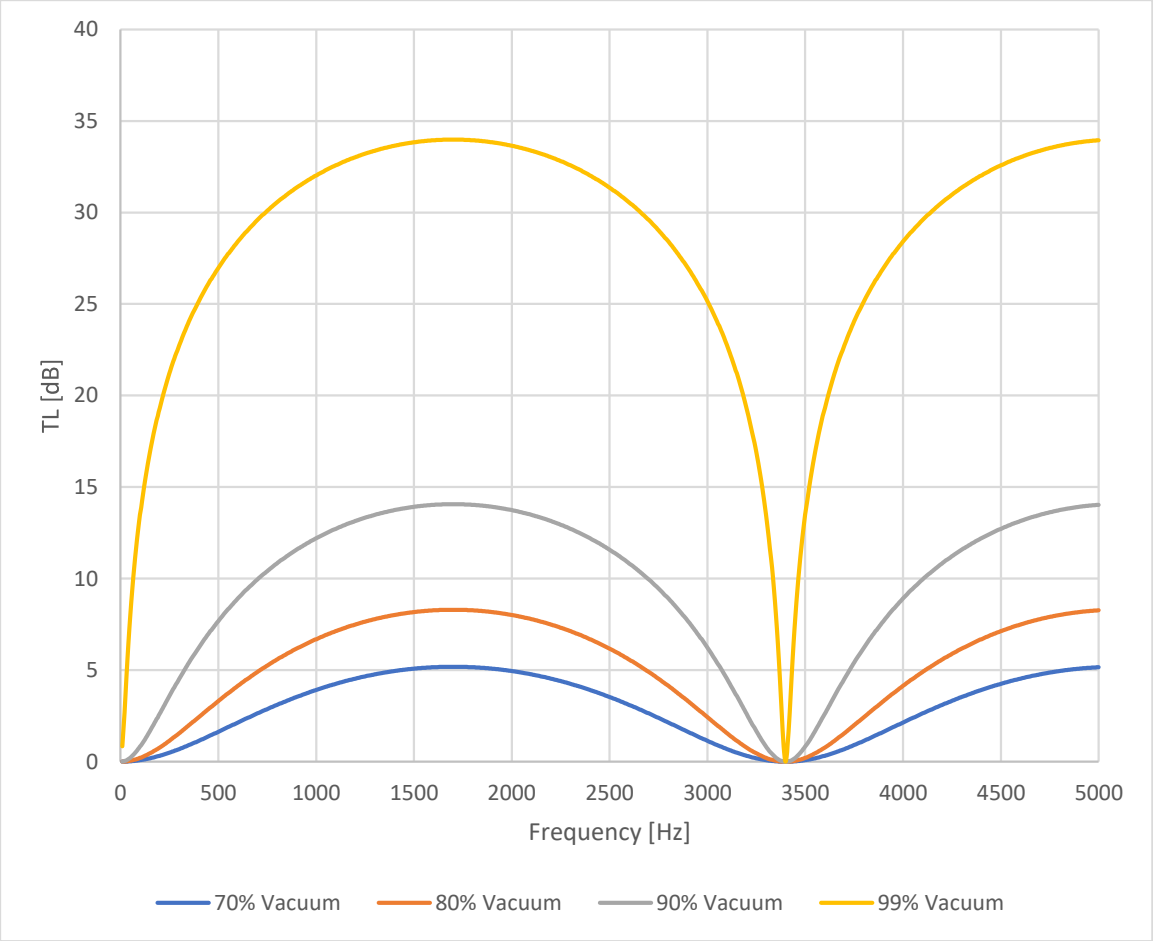


Figure 2.8. Transmission loss – cavity pressure comparison.

For a better representation of the proposed structure, a model with two partitions and a cavity media in between can be investigated. This structure is called a "Double-Leaf Partition" and analytical solution is derived by London [60]. However, the derived solution only covers the case which the cavity media is of same impedance as the incident and transmitted media. Therefore, the effect of impedance mismatch by the vacuumed cavity cannot be investigated.

2.4. Quasi – Zero Stiffness Mechanisms

For a single degree of freedom system (see Figure 2.9), the harmonic response to unit input decreases exponentially for excitations above the natural frequency. The decreasing response ensures decrease in both displacement amplitudes and force levels inserted.

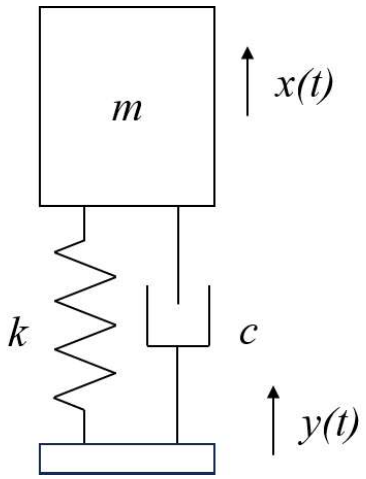


Figure 2.9. Displacement transmissibility in a 1 degree of freedom system.

Displacement transmissibility for a single degree of freedom system is derived by solving the dynamic equilibrium equations as [61]:

$$\omega_n = \sqrt{\frac{k}{m}}, \tag{2.19}$$

$$r_\omega = \frac{\omega}{\omega_n}, \tag{2.20}$$

$$\zeta = \frac{c}{2\sqrt{km}}, \tag{2.21}$$

$$\frac{X}{Y} = \sqrt{\frac{1 + (2\zeta r_\omega)^2}{(1 - {r_\omega}^2)^2 + (2\zeta r_\omega)^2}}. \tag{2.22}$$

This principle has long been used for vibration isolation in variety of systems. Lowering stiffness of the coupling parts/agents is practiced to alter the natural frequency of the system of interest. With lowered stiffness, the displacement under static load increases. This relation draws the limit of the low stiffness application since the low stiffness coupling parts/agents also have low load bearing capacities. This limitation can be overcome by incorporating nonlinear stiffness elements. Such nonlinear stiffness elements exhibit high stiffness under low displacements and low stiffness at a certain displacement, which provides the static load bearing capacity and low stiffness during operation. These systems are called “quasi – zero stiffness mechanisms” shown in Figure 2.10.

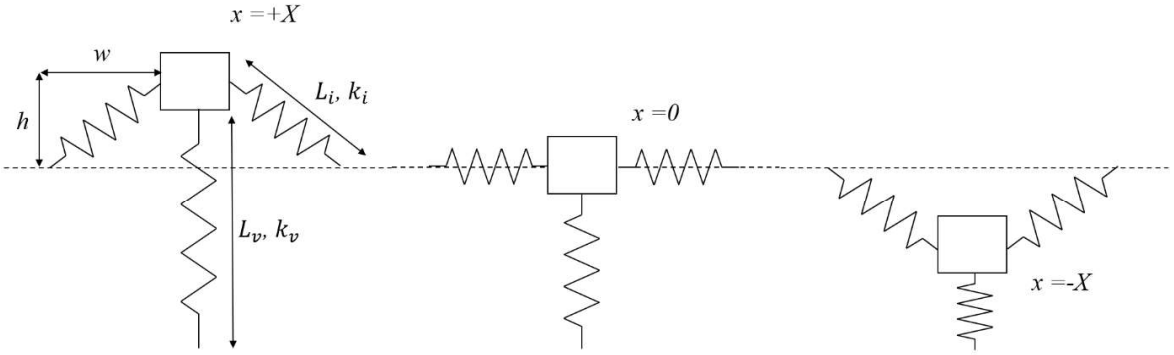


Figure 2.10 Lumped quasi – zero stiffness mechanism model.

Mechanical properties of the quasi – zero stiffness mechanism is derived herein. The mechanism consists of two inclined and one vertical linear springs. Inclined springs have the initial length of L_i and stiffness of k_i. Vertical spring has the initial length of L_v and stiffness of k_v. Initially, the mechanism at rest with the springs carrying no load. Here x depicts the vertical position of the joint. When the connecting joint is forced downwards, springs are compressed by ΔL_i and ΔL_v, given as

$$\Delta L_i = \sqrt{x^2 + w^2} - \sqrt{h^2 + w^2}, \tag{2.23}$$

$$\Delta L_v = x - h. \tag{2.24}$$

The total reaction force acting on the joint is calculated by summing the vertical forces of the springs. The spring forces and the total reaction forces calculated as

$$F_{i,v} = 2k_i x\left(\frac{\sqrt{x^2 + w^2} - \sqrt{h^2 + w^2}}{\sqrt{x^2 + w^2}}\right), \tag{2.25}$$

$$F_{v,v} = k_v(x - h), \tag{2.26}$$

$$F_r = -\left(F_{i,v} + F_{v,v}\right) = -2k_i x\left(\frac{\sqrt{x^2 + w^2} - \sqrt{h^2 + w^2}}{\sqrt{x^2 + w^2}}\right) - k_v(x - h). \tag{2.27}$$

The vertical force on the vertical spring has a linear relationship with the joint position. On the other hand, forces due to the inclined springs has a rather complex formula because of the changing orientation as the joint is forced down. Reaction forces occurring for a tuned quasi – zero stiffness are given in Figure 2.11. As the joint is displaced down from the +1 unit distance, reaction forces of the inclined springs initially increase. As the joint is displaced further, these forces start to decrease and eventually reach 0 when the inclined springs become parallel to the ground. The load is carried by the vertical spring at this point.

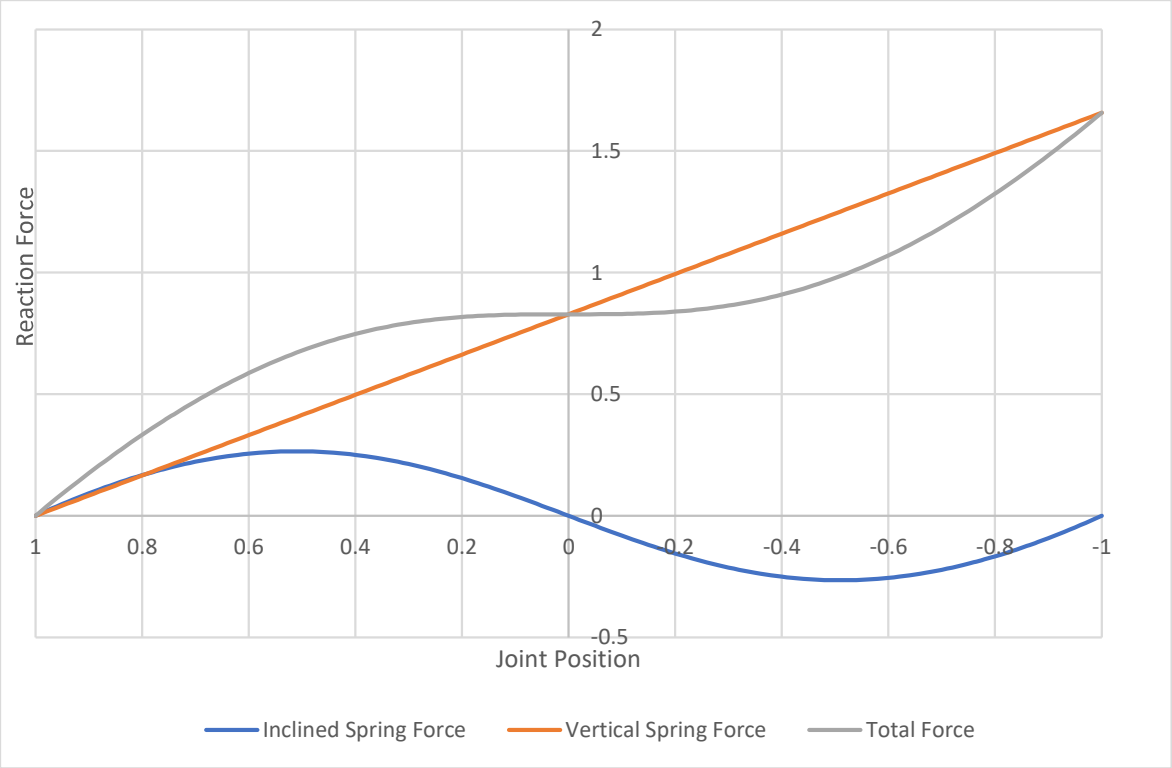


Figure 2.11. Reaction forces of a tuned quasi – zero stiffness mechanism.

The overall stiffness of the mechanism k_t is derived by differentiating overall force response by the displacement. The varying stiffness for the quasi – zero stiffness mechanism is derived as

$$\frac{dF_{i,v}}{dx} = 2k_i x w^2 \left(\frac{1 - \sqrt{h^2 + w^2}}{(x^2 + w^2)^{3/2}} \right), \tag{2.28}$$

$$\frac{dF_{v,v}}{dx} = k_v, \tag{2.29}$$

$$k_t = \frac{dF_{i,v}}{dx} + \frac{dF_{v,v}}{dx} = 2k_i x w^2 \left(\frac{1 - \sqrt{h^2 + w^2}}{(x^2 + w^2)^{3/2}} \right) + k_v. \tag{2.30}$$

In order to obtain zero stiffness, the Equation (2.30) needs to be solved to yield 0 at the displacement x=0. This relation is given by

$$\frac{1 - \sqrt{h^2 + w^2}}{w} = -\frac{k_v}{2k_i}. \tag{2.31}$$

Based on this relation; initial height, width, stiffness of the vertical and inclined springs all need to be chosen accordingly to achieve near zero stiffness. Stiffness of the tuned mechanism by the joint position is given in Figure 2.12.

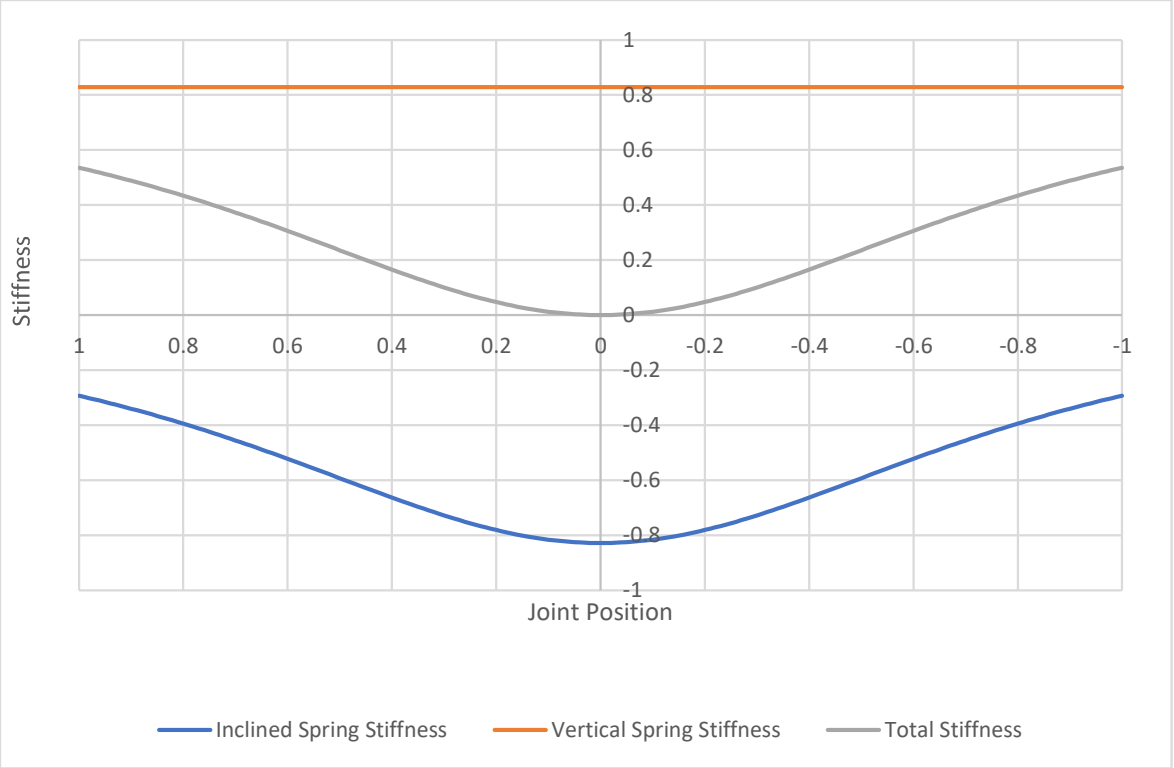


Figure 2.12. Stiffness of a tuned quasi – zero stiffness mechanism.

There are certain considerations to be taken into account for a quasi – zero stiffness mechanism to isolate vibrations successfully. Quasi – zero stiffness mechanisms provide near zero stiffness and thus vibration isolation for limited displacement/force level. This point will be called quasi – zero stiffness level. Such initial displacement/force insertion is what conditions the mechanism to exhibit near zero stiffness with applied excitation. This displacement/force level must be tuned to match the load on the system so that the system can get to the near zero stiffness state by the load on itself. It is also known that the near zero stiffness behavior is limited to certain range of oscillations around the quasi – zero stiffness level. This range can be influenced by the design of negative and positive stiffness elements [61, 62]. In Figure 2.13, total vertical stiffness (normalized by inclined stiffness) curves for different dimension ratios ($\eta = h/w$) are given. Smaller the ratio gets, wider range for near zero stiffness behavior is obtained. The system could exhibit higher stiffness with the increased excitation amplitudes if the range of the quasi – zero stiffness is not considered, reducing the effectiveness of the vibration isolation.

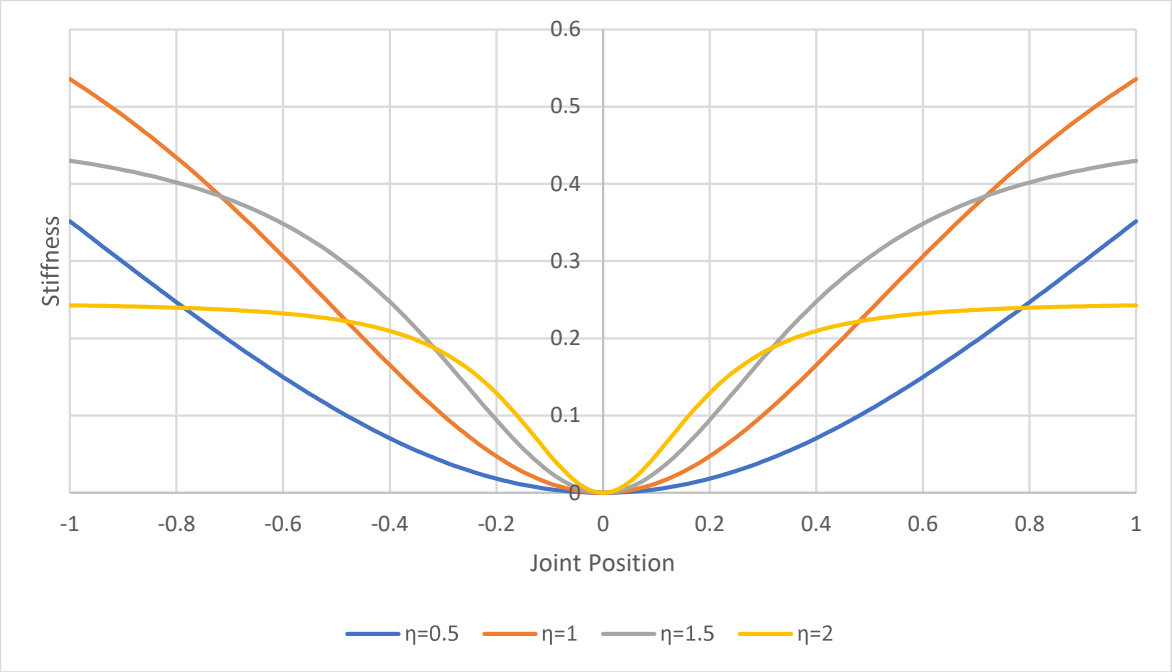


Figure 2.13. Quasi – zero stiffness mechanism parametric stiffness.

2.5. Convex Diaphragms

The aim in this thesis is to obtain quasi-zero stiffness response around 1 atm external pressure. To that end, one can use convex diaphragms (see Figure 2.14) [63].

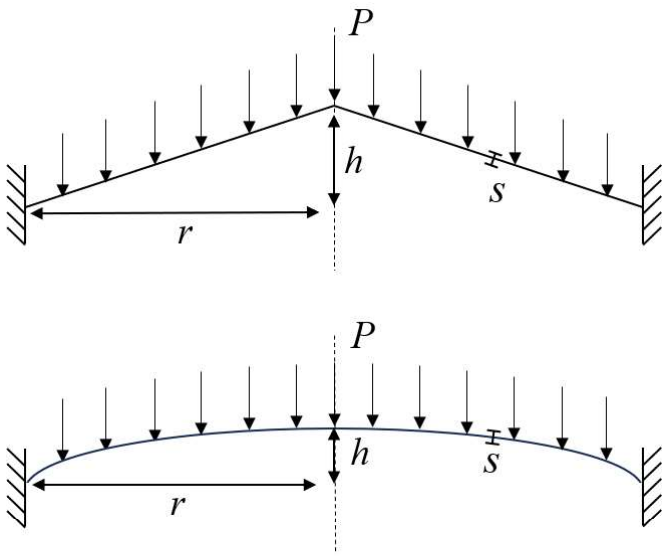


Figure 2.14. Pressure loaded convex diaphragms: (a) conical, (b) spherical.

Characteristic equations for clamped convex diaphragms are

$$\frac{Pr^4}{Es^4} = A\frac{y_0}{s} \pm B\frac{{y_0}^2}{s^2} + C\frac{{y_0}^3}{s^3}, \tag{2.32}$$

$$A = 5.86 + 3.45\frac{h^2}{s^2}; B = 6.52\frac{h}{s}; C = 2.76, \tag{2.33}$$

$$A = 5.86 + 4.88\frac{h^2}{s^2}; B = 7.72\frac{h}{s}; C = 2.76. \tag{2.34}$$

The $\pm$ sign in Equation (2.32) in front of the $\frac{{y_0}^2}{s^2}$ term depicts the stiffening effect of a convex diaphragm and – sign is used when the pressure is loaded from the convex side and + sign is used when the pressure is applied from the concave side, The constants *A*, *B* and *C* for conical and spherical diaphragms are provided in Equation (2.33) and Equation (2.34), respectively. Figure 2.15 shows pressure-displacement response of conical diaphragms for various convexity ratios *h/s* where *h* is the apex height and *s* is the diaphragm thickness. Moreover, Figure 2.16 shows pressure-displacement response of spherical diaphragms for various convexity ratios *h*/*s*.

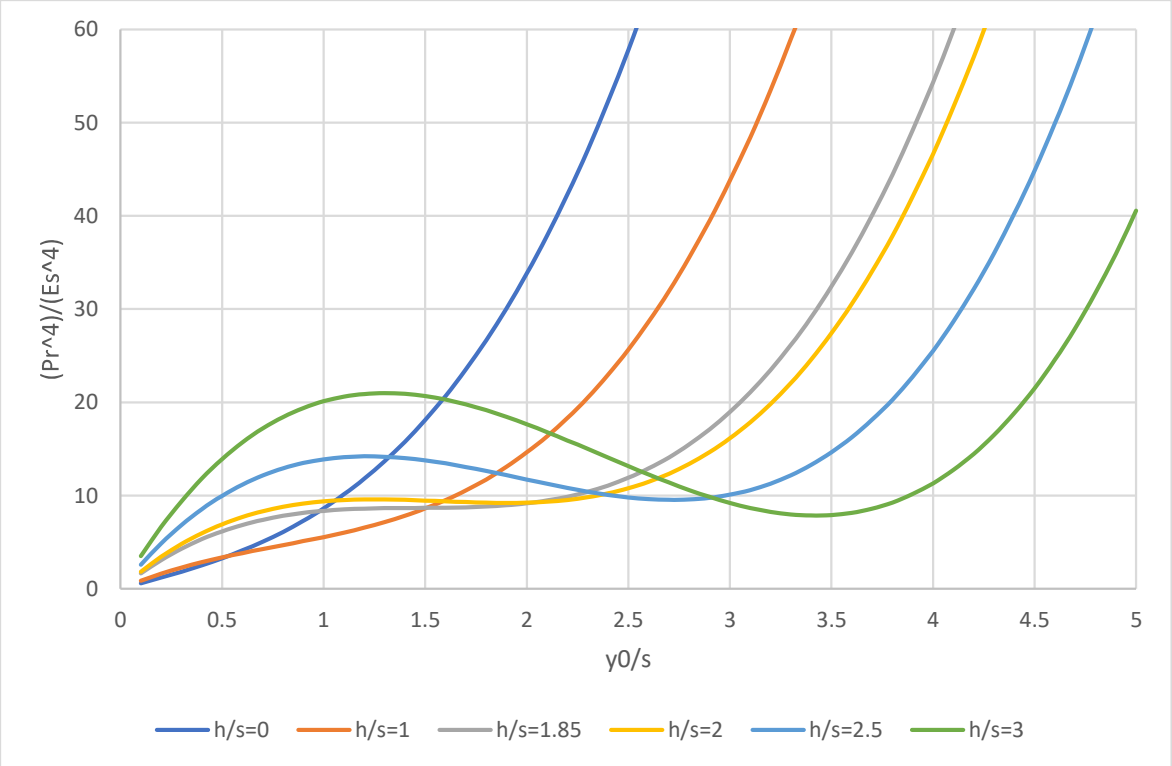


Figure 2.15. Pressure – displacement curve of conical diaphragms for various convexity ratios.

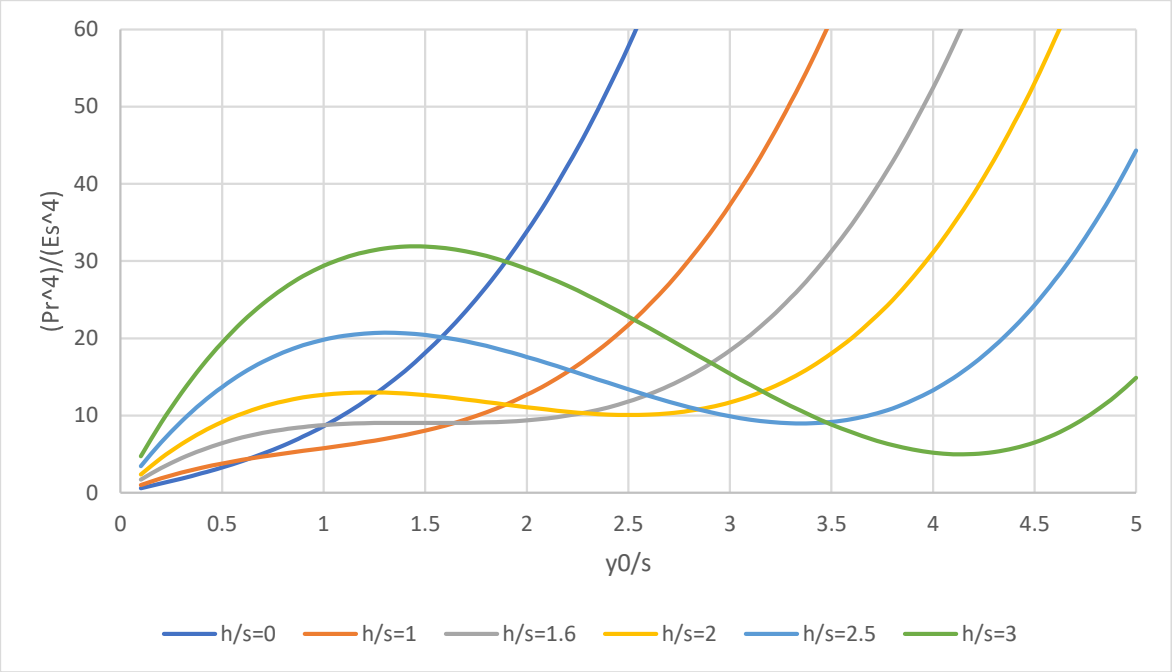


Figure 2.16. Pressure – displacement curve of spherical diaphragms for various convexity ratios.

Quasi-zero stiffness response is achieved at h=1.84s for clamped conical diaphragms and h=1.59s for clamped spherical diaphragms. Figure 2.17 and Figure 2.18 show that quasi-zero stiffness is achieved at 1 atm external pressure for s=0.777 mm and s=0.769 mm in the case of conical and spherical steel diaphragms (E=200 GPa) of 100 mm diameter.

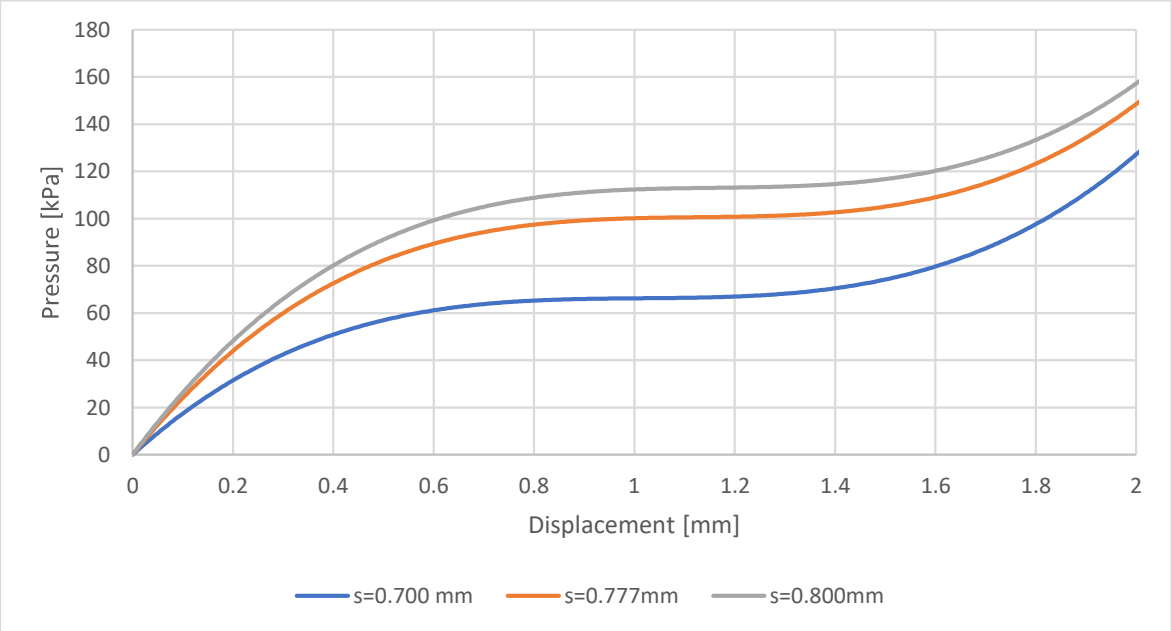


Figure 2.17. Conical diaphragm pressure – displacement curve.

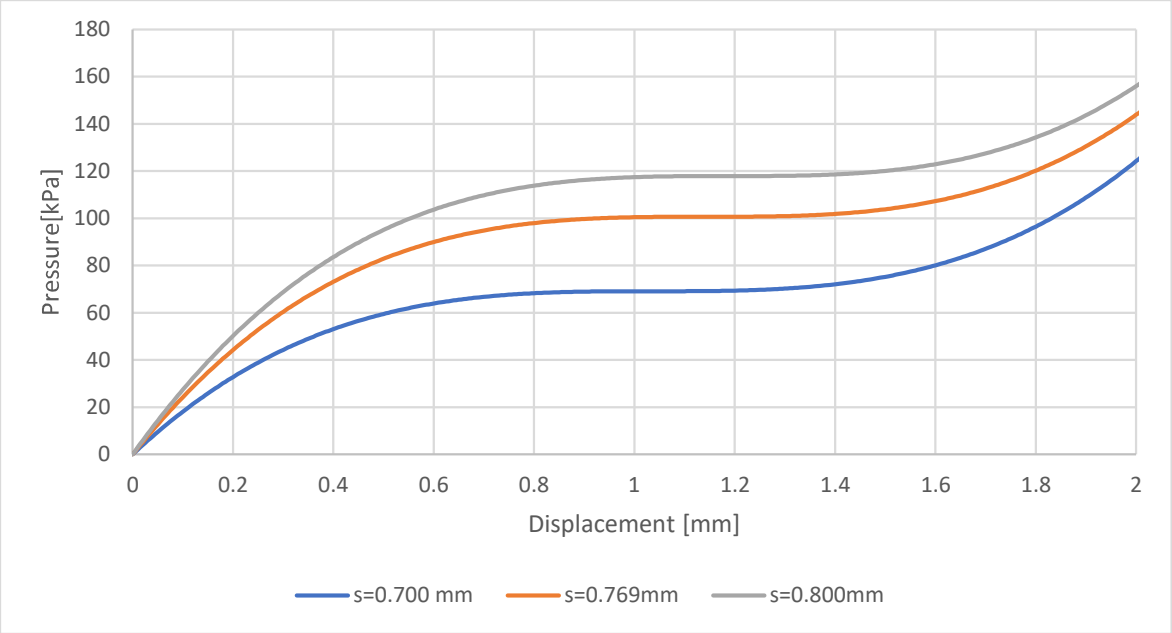


Figure 2.18. Spherical diaphragm pressure – displacement curve.

Sheet metals are generally available with 0.1mm thickness increments. Hence, the best choice is 0.7 mm sheet thickness, which gives 0.66 kPa and 0.69 kPa vacuum pressure for conical and spherical diaphragms, respectively.

Conical convex diaphragms are preferred for the ease of manufacturability compared to the spherical diaphragms. The accuracy of the given pressure – displacement mathematical solution is investigated comparatively by equivalent finite element analyses. Pressure loading of the diaphragm studies are carried out by fully elastic static structural finite element analyses. The diaphragm is subjected to incremental pressure loading and the resulting displacement of the diaphragm center is obtained. Finite element models of clamped diaphragms with specified apex height, radius and thickness are created. Diaphragm material is set to steel (E=200 GPa) accordingly. However, conical diaphragms with the ratio of h/s=1.84 are observed to undergo buckling. In order to overcome this effect and obtain quasi-zero stiffness, the finite element model of the diaphragm is updated to the ratio h/s=1.75 while keeping the diaphragm thickness constant. Pressure – displacement comparisons of finite element analyses and mathematical solutions of 0.7 mm, 0.777 mm and 0.8 mm thick conical diaphragms are shown in Figure 2.19, Figure 2.20 and Figure 2.21 respectively. Satisfactory agreement of the finite element and mathematical solutions are observed.

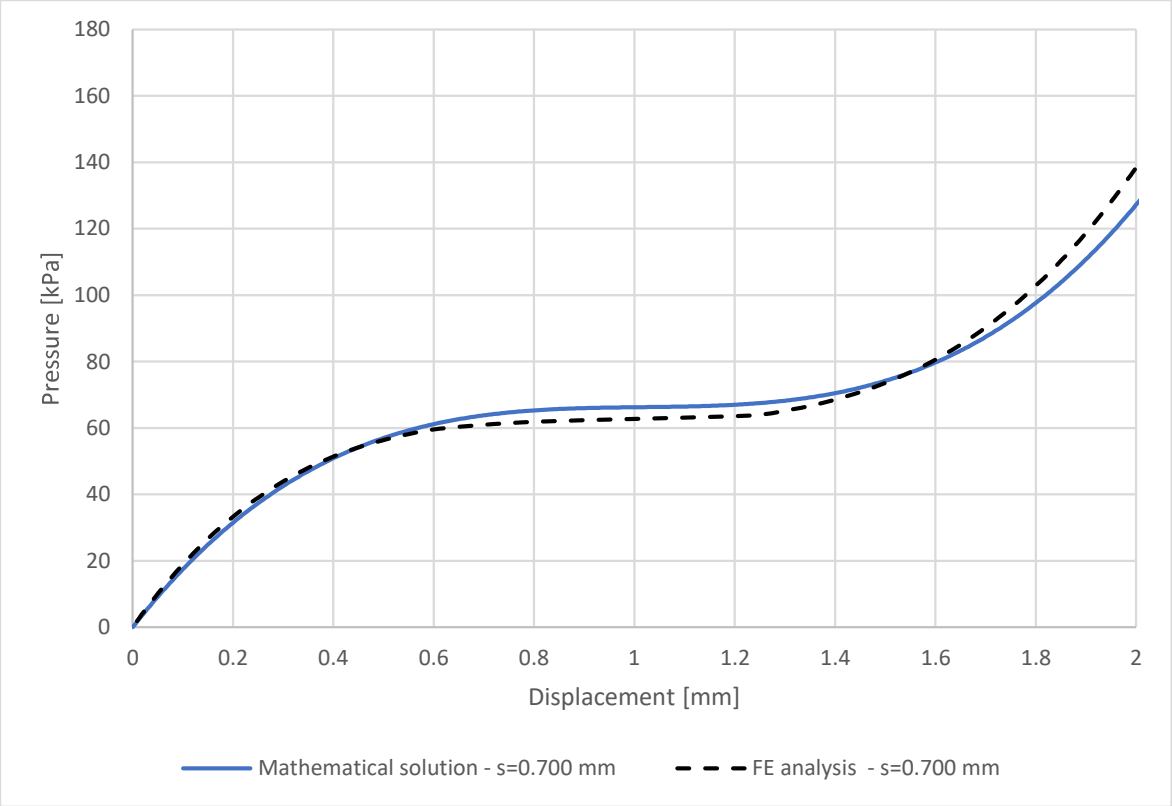


Figure 2.19. Conical diaphragm s=0.700 mm – analysis/mathematical solution comparison.

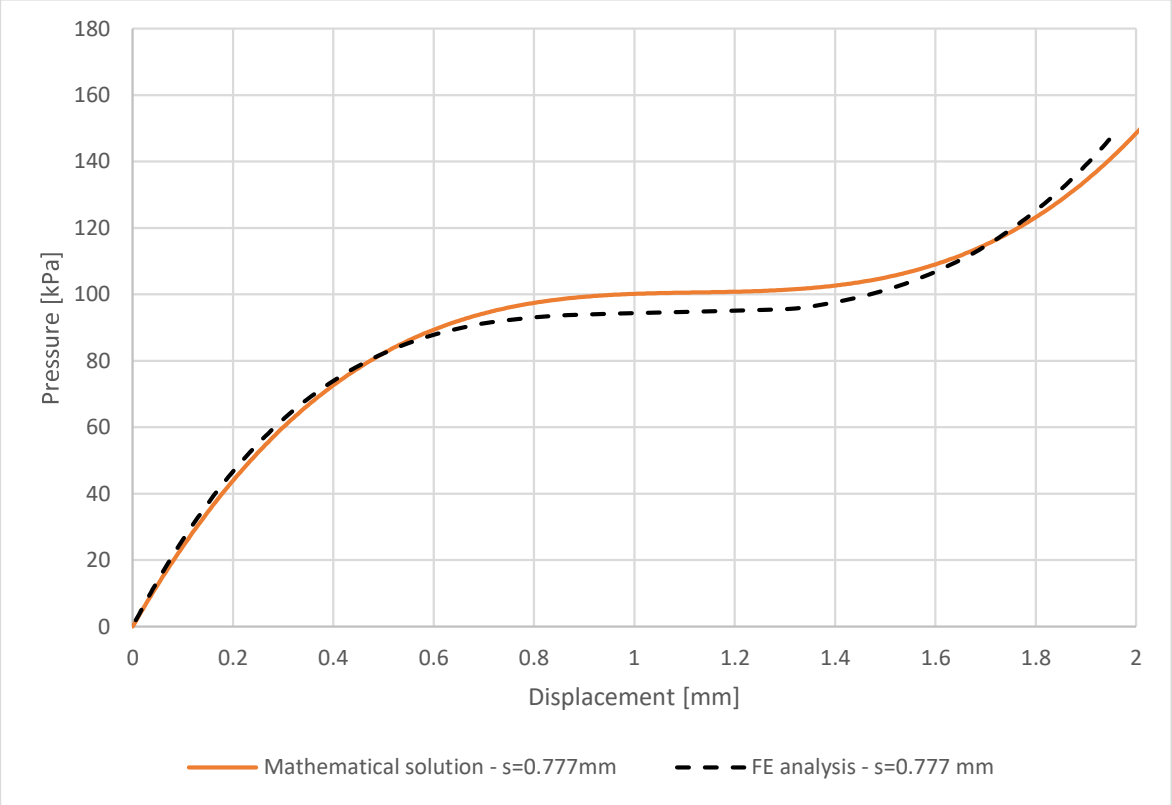


Figure 2.20. Conical diaphragm s=0.777 mm – analysis/mathematical solution comparison.

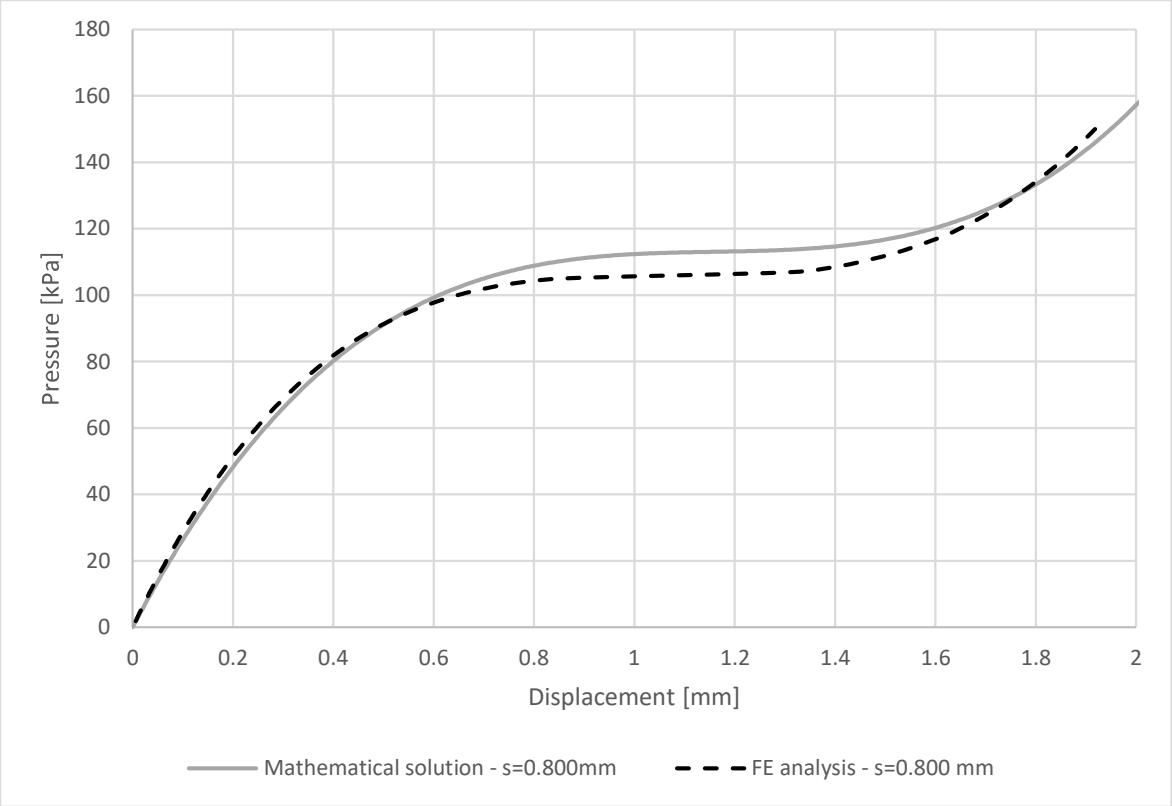


Figure 2.21. Conical diaphragm s=0.800 mm – analysis/mathematical solution comparison.

3. PROPOSED DESIGN

The proposed idea is to design a double-leaf partition structure. The impedance mismatch is created by vacuuming the enclosure to a required extent. In order to avoid structural coupling, the structure is designed to withstand the external pressure without any additional supporting members. Structural resonances at lower frequencies are avoided by tuning the design to have low transverse stiffness. Such low stiffness is achieved by utilizing quasi-zero stiffness, which in turn improves the sound insulation properties at low frequencies.

In this section, the finite element analyses are presented. Finite element studies are divided into two parts. Firstly, the effect of low stiffness and impedance mismatch incorporated double leaf partitions are analyzed. Transmission loss for such design is compared with a non-altered double leaf partitions. Secondly, optimization studies are aimed to find appropriate structural designs for quasi-zero stiffness behavior under pressure loading. The design geometry is optimized with structural and modal analyses.

3.1. Acoustic Finite Element Analyses

The objective of this thesis is to maximize the acoustic transmission loss by lowering the fundamental natural frequency and increasing the impedance mismatch. In this section, the potential benefits of this idea is examined via finite element studies. Since the problem to be solved includes both the fluid and structural media response, vibroacoustic analyses were carried out. The preferred tool for the analyses is FFT – Actran. The methodology of the studies are as follows:

- Designating the partition type and appropriate boundary conditions,
- Altering the transverse stiffness externally to replicate dynamic character of the quasi-zero stiffness presenting partitions,
- Running acoustic transmission loss analyses,
- Examining and comparing the results.

The element sizing is determined by the ability of capturing travelling waves on the media. The acoustic transmission loss analyses are to be carried out up to 5 kHz. The limiting media in this vibroacoustic problem are the solid plates. The mesh size computed to have at least 8 elements per the smallest wavelength is 5.5 mm. Therefore, the plates are modeled with 5 mm quad mesh elements. The fluid media is also modeled by the same sizing and element type to simplify the coupling between partition and cavity elements. The partitions were modeled as “Thin Shell” components, and the fluid media was modeled as “Finite Fluid” components. The altering of the transverse stiffness was achieved by modelling an external spring element between the middle node of the plate and circumference of the plate. The spring was modeled as “Discrete” component.

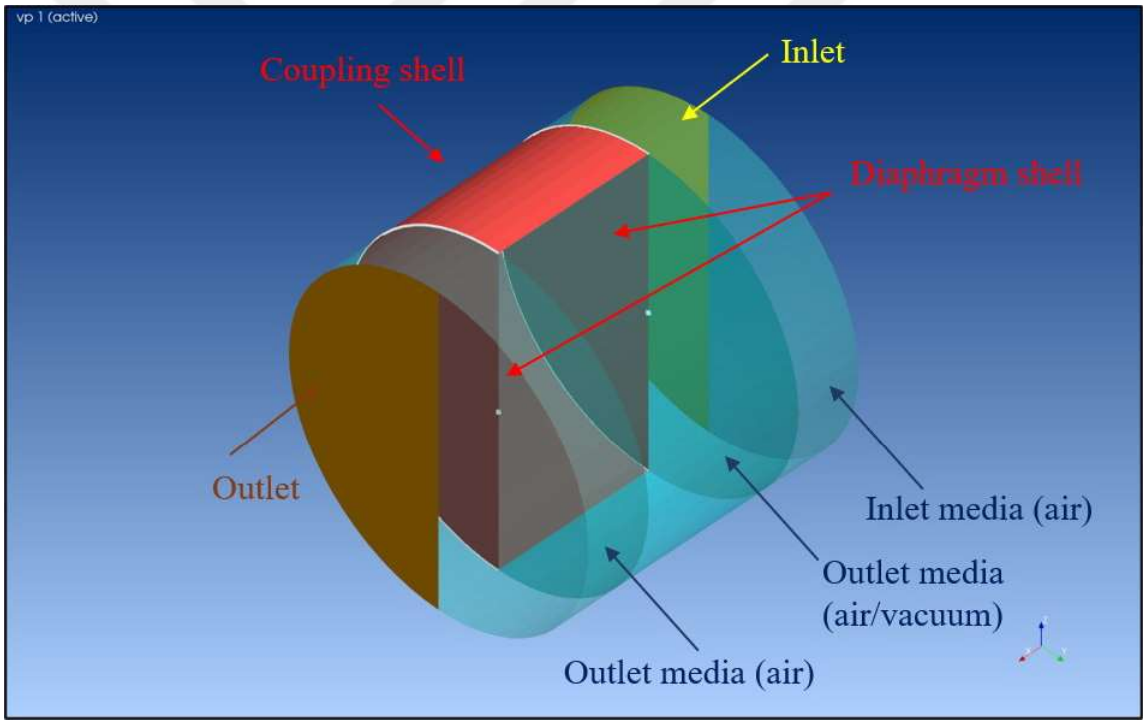


Figure 3.1. Acoustic model for transmission loss analyses.

The modal analyses were run only on the structural part of the model. The free body modes (if exist) were left of the presented solution. The same structural mesh was used on both modal and acoustic transmission loss analyses. The acoustic transmission loss analyses were defined as it is shown in the Figure 3.1. There is an inlet surface, followed by a fluid (air) media, followed by the partitions and outlet surface. Input acoustic excitation is provided as plane waves in the whole frequency region of the interest. The controlled excitations and corresponding acoustic boundary conditions were set up by the “Modal

Duct" component. The input is limited to the (0,1) mode, plane wave for circular duct. The propagating and reflecting directions on the acoustic boundaries are set free for any acoustic wave. This allowed the comparison of the acquired solution with simple analytical calculations and impedance tube measurement results.

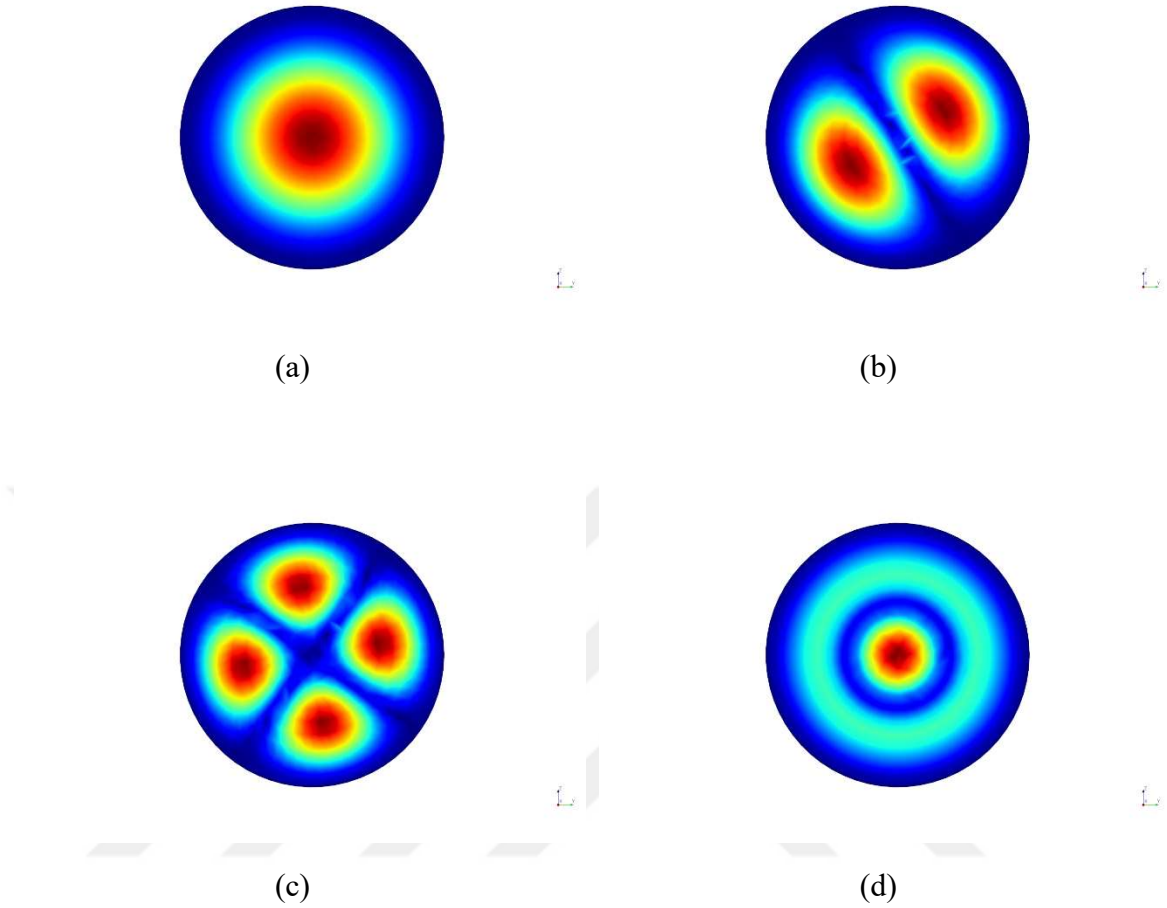
3.1.1. Structurally Uncoupled Double Partition

First model investigated is the fully uncoupled structure. This is the ideal case where the vibrations of the partition induced by the incident acoustic waves are solely transferred to the following partition by the fluid media between. Such model is an appropriate approach where the flanking transmissions could be neglected. The model consists of two 1 mm thick circular plates with 50 mm gap in between. The material is set to steel (Young Modulus: 200 GPa, Poisson Ratio: 0.3, Density: 7850 kg/m^3). The diameter of the plates is 100 mm, which is chosen for consistency throughout the thesis. Clamped boundary condition is applied to both plates on the edges.

The computed natural frequencies and the mode shape explanations are given in Table 3.1. The first natural frequency is brought down to the 1/10th of the original value. It is shown that only the first natural frequency has shifted significantly. Since the added spring element is located on the center of the plate, it was expected that it would not affect the modes with radial order greater than 0 where the center is stationary. Although this is not the case for the mode (0,2), it is only slightly altered. This is explained by the increased stiffness of this mode compared to the (0,1) mode. This is convenient in terms of observing the effect of the fundamental mode on the acoustic transmission loss. The mode shapes of the single plate are given in Figure 3.2.

Table 3.1. Natural frequencies & mode shapes of the uncoupled partition.

Mode: Order	Original Plate	Quasi-Zero Stiffness Plate
1 : (0,1)	993.9 Hz	105.8 Hz
2 : (1,1)	2080.5 Hz	2080.5Hz
3 : (2,1)	3425.6 Hz	3416.1 Hz
4 : (0,2)	3936.3 Hz	3733.3 Hz



(a) (b)

(c) (d)

Figure 3.2. Mode shapes of the uncoupled partition, (a) 1st mode shape (0,1), (b) 2nd mode shape (1,1), (c) 3rd mode shape (2,1), (d) 4th mode shape (0,2).

Transmission loss analyses were run to investigate the outcomes of the proposed vacuum and low stiffness. The vacuum for this study was kept at 80% (0.2 atm absolute pressure) level which is determined as bare plausible level in terms of applicability. The results are presented as the following comparisons:

- Comparison 1: Original plate with 1 atm and 0.2 atm cavity pressure,
- Comparison 2: Original Plate with 1 atm cavity pressure and quasi-zero stiffness plate with 1 atm cavity pressure,
- Comparison 3: Original Plate with 1 atm cavity pressure and quasi-zero stiffness plate with 0.2 atm cavity pressure.

The comparison 1 results are shown in the Figure 3.3. As it can be seen, the same dips are observed in both cases. There are only slight deviations in 3000-3500 Hz region

which is due to the cavity-structure interaction as it was shown previously in Figure 2.8. The most obvious outcome of utilizing vacuum in partition is the observed mean 14 dB increase in transmission loss throughout the whole frequency range.

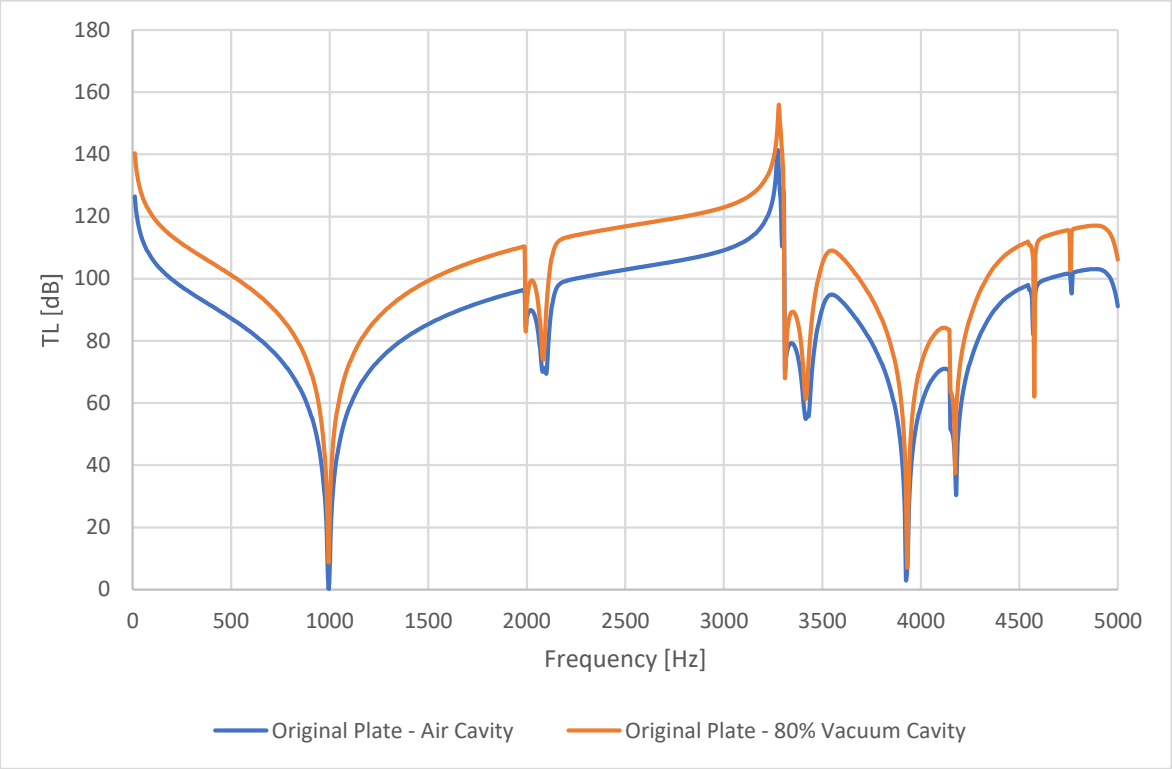


Figure 3.3. Uncoupled partition – transmission loss of original plate with 1 atm and 0.2 atm cavity pressure.

Comparison 2, shown in Figure 3.4, reveals the effect of plate stiffness on transmission loss. The first dip in both curves is due to the fundamental modes as expected. The shift of the fundamental mode towards lower frequencies has successfully improved transmission loss between 690 Hz and 3100 Hz. The dip due to the second circumferential mode also shifted, yet not significantly. The dips due to other modes and cavity-structure interaction remained the same. One of the peaks at 3275 Hz has drastically shifted to 2810 Hz, which again increases the transmission loss up to 3100 Hz. One can clearly observe that the transmission loss of a finite panel is affected by the transverse stiffness just as much as the infinite panel analytical solution (compare Figures 2.6 and 3.4). This quasi-zero stiffness plate partition performs well above the standard double leaf partition and provides promising low frequency sound insulation.

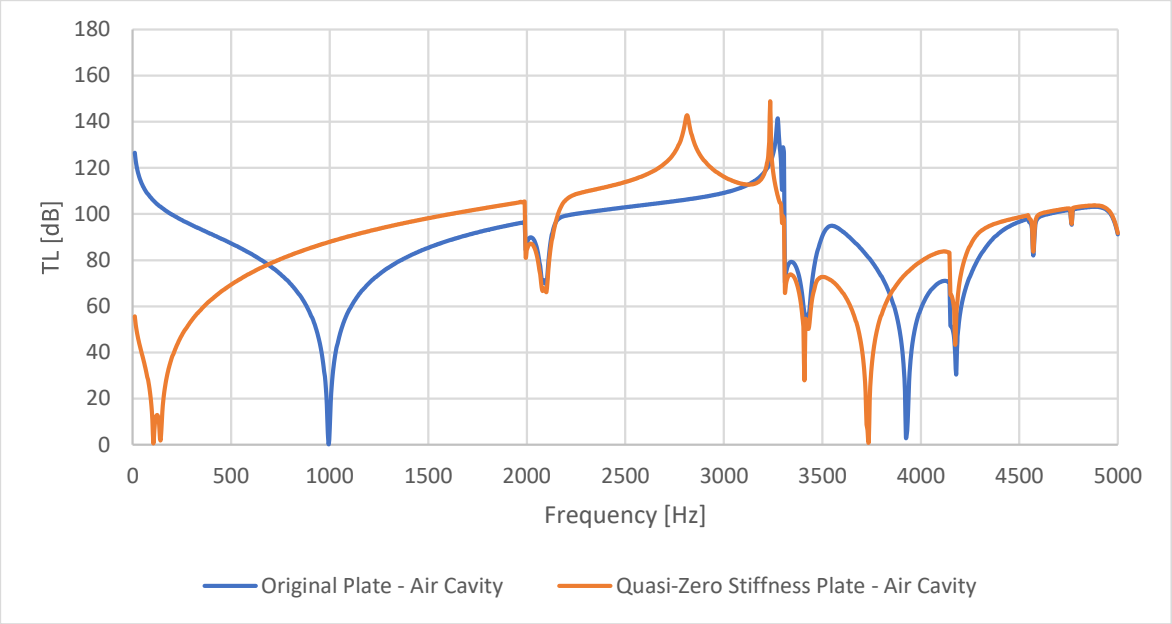


Figure 3.4. Uncoupled partition – transmission loss of original plate with 1 atm cavity pressure and quasi-zero stiffness plate with 1 atm cavity pressure.

The final comparison reveals the potential for such sound insulation structure. Transmission loss can be increased up to 100 dB around 1000 Hz and 27 dB mean increase in 550-3000 Hz frequency range. High frequency region is not investigated. Yet, the positive effect of the vacuum is expected for high frequencies, as well.

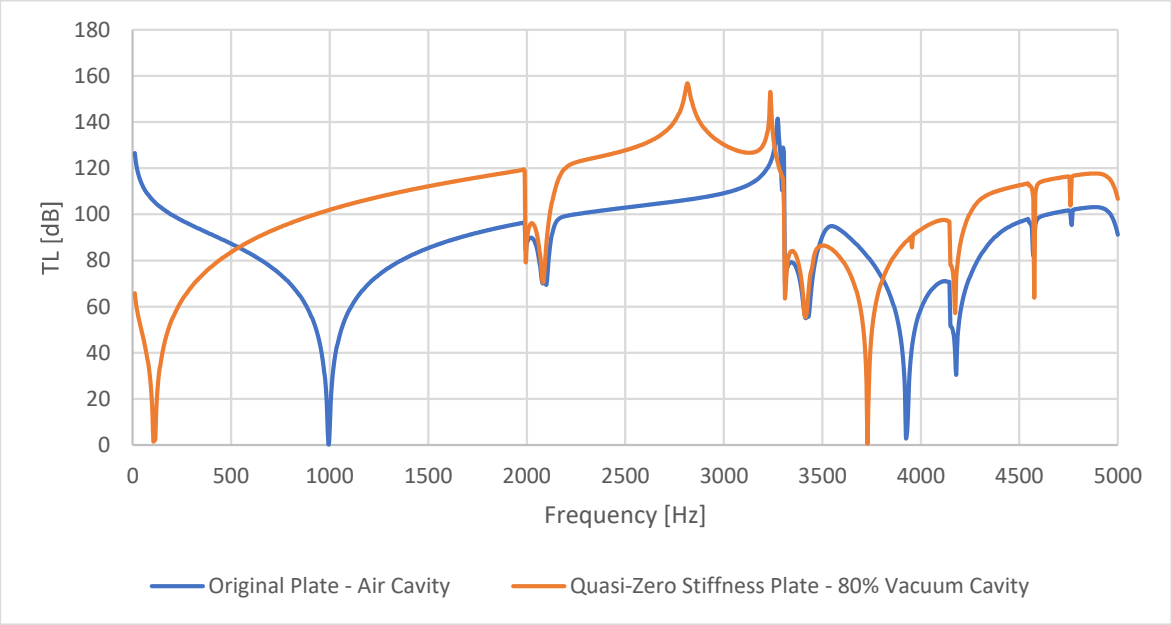


Figure 3.5. Uncoupled partition – transmission loss of original plate with 1 atm cavity pressure and zero stiffness plate with 0.2 atm cavity pressure.

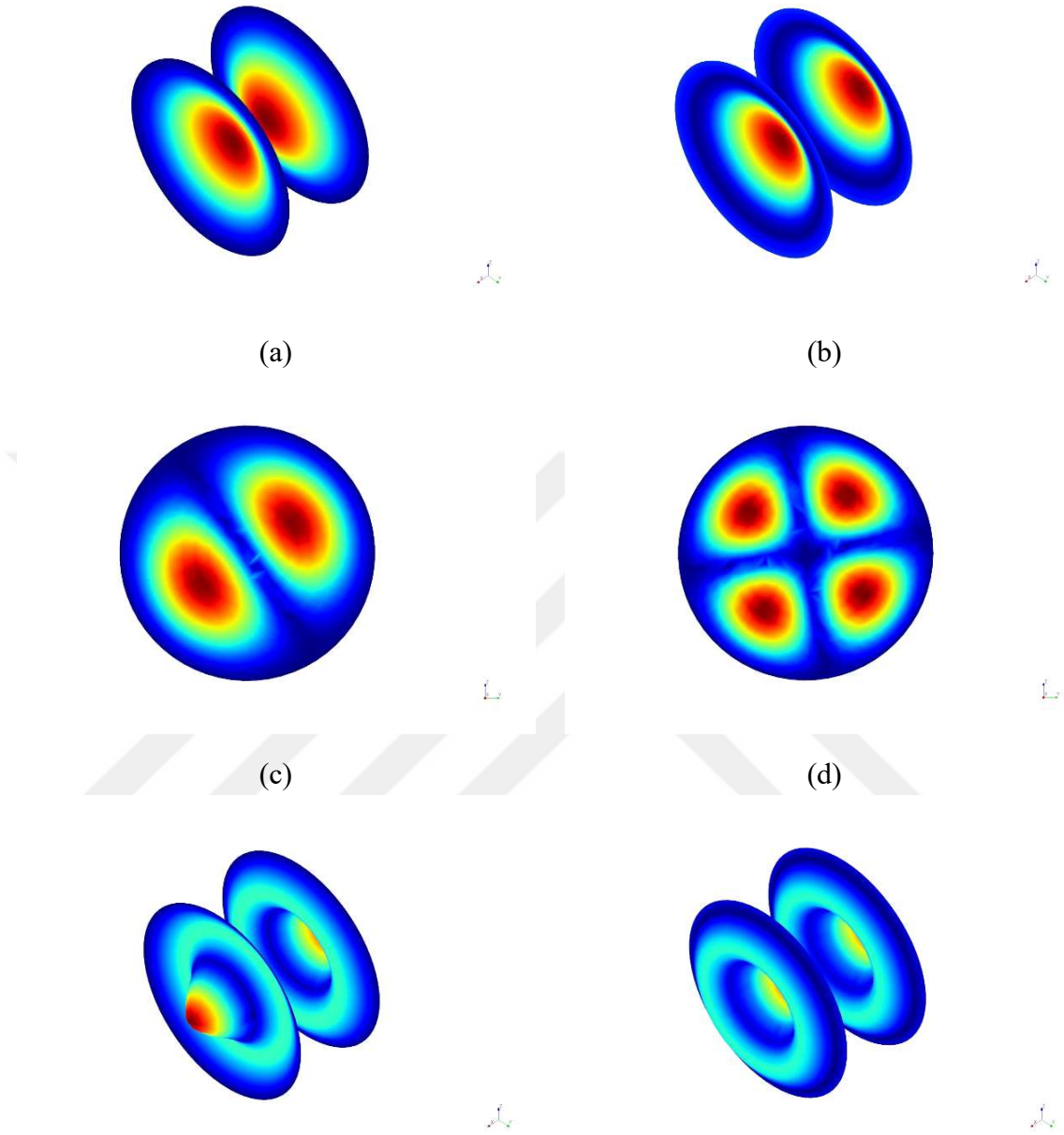
3.1.2. Structurally Coupled Double Partition

The second model of interest is the structurally coupled case. This model consists of the two diaphragms connected by an outer shell. The outer shell provides structural integrity against the external pressure loading and sustains sealing. The transmission path of the incident acoustic waves includes both the structure – cavity – structure and flanking mechanisms. This model has further importance because of the application simplicity. The structure similarly consists of two 1 mm thick circular plates with 50 mm gap in between. The material is selected as steel (Young Modulus: 200 GPa, Poisson Ratio: 0.3, Density: 7850 kg/m^3). The diameter of the plates is 100 mm. The transmission loss measurement in an impedance tube conditions are pursued. Whole model has free boundary conditions. In order to justify the presumed boundary conditions, an alternative of applying weak spring connections on the contact surfaces has been considered. Since both free and spring supported cases yielded the same outcomes in terms of modal frequencies and transmission loss curves, free boundary condition is chosen.

The computed natural frequencies and the mode shape explanations are given in Table 3.2. The first natural frequency is brought down to the 1/10th of the original value as it was in the uncoupled structure. For the mode shapes (0,1) and (0,2), in phase (IP) and out of phase (OP) motions are observed. These modes are all shifted to lower frequencies. The generated shift decreases substantially, even though the second mode is not decreased to half the original frequency. The modes where the radial orders are greater than 0 are not affected. The mode shapes of the plates are given in Figure 3.6

Table 3.2. Natural frequencies & mode shapes of the coupled partition.

Mode: Order	Original Plate	Quasi-Zero Stiffness Plate
1 : (0,1) – OP	903.6 Hz	101.3 Hz
2 : (0,1) – IP	1071.0 Hz	678.0 Hz
3 : (1,1)	1891.0Hz	1891.0Hz
4 : (2,1)	3091.6 Hz	3091.6 Hz
5 : (0,2) – OP	3618.2 Hz	3433.1 Hz
6 : (0,2) – IP	3873.2 Hz	3697.4 Hz



(a) (b)

(c) (d)

(e) (f)

Figure 3.6. Mode shapes of the coupled partition, (a) 1st mode shape (0,1– OP), (b) 2nd mode shape (0,1– IP), (c) 3rd mode shape (1,1), (d) 4th mode shape (2,1), (e) 5th mode shape (0,2 – OP), (f) 6th mode shape (0,2 – IP).

Transmission loss analyses and comparisons are the same as the previous case. The vacuum for this study was kept at 80% (0.2 atm absolute pressure level), which is determined as bare plausible level in terms of applicability. The results are presented as the following comparisons:

- Comparison 1: Original plate with 1 atm and 0.2 atm cavity pressure,
- Comparison 2: Original Plate with 1 atm cavity pressure and quasi-zero stiffness plate with 1 atm cavity pressure,
- Comparison 3: Original Plate with 1 atm cavity pressure and quasi-zero stiffness plate with 0.2 atm cavity pressure.

The first comparison in Figure 3.7 shows interesting results. Unlike the uncoupled structure, the transmission loss dips due to the radial modes are totally diminished. As for the radial modes, both the in phase and out of phase modes cause reductions in insulation. Furthermore, the reduction of the cavity medium density yields a totally different outcome in transmission loss. Increase in transmission loss seen with the uncoupled partition is not present. Yet, local enhancements can be observed by the transmission loss curve. It can be concluded for the coupled structure, the main path for acoustic transmission is not the cavity, but the flanking mechanism.

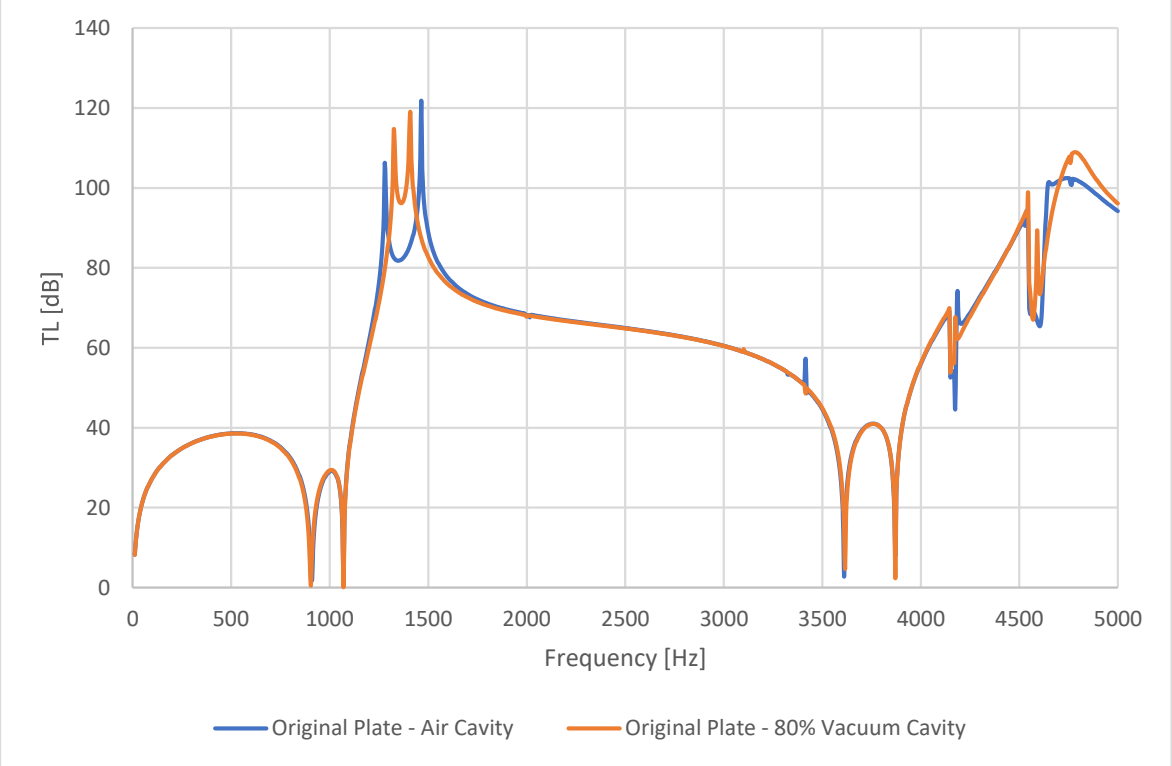


Figure 3.7. Coupled partition – transmission loss of original plate with 1 atm and 0.2 atm cavity pressure.

The shift in the fundamental plate modes has a rather intricate influence on transmission loss. In Figure 3.8, the transmission loss comparison between the quasi-zero stiffness and original partition is given. Lowering the transverse stiffness enhanced acoustic insulation between 280 Hz and 1210 Hz. On the other hand, between 1210 Hz and 3550 Hz the high stiffness system performs better. However, the aim in this thesis is to improve low frequency response so quasi-zero stiffness system is preferred.

Since the effect of vacuum is limited, Comparison 3 given in Figure 3.9 presents similar results to Comparison 2. The transmission loss increase is mainly attributed to the lowered fundamental stiffness. This concludes that for a structurally coupled sound transmission barrier, where the flanking transmission path is dominant, low frequency sound insulation is heavily dependent on the transverse diaphragm stiffness rather than cavity media.

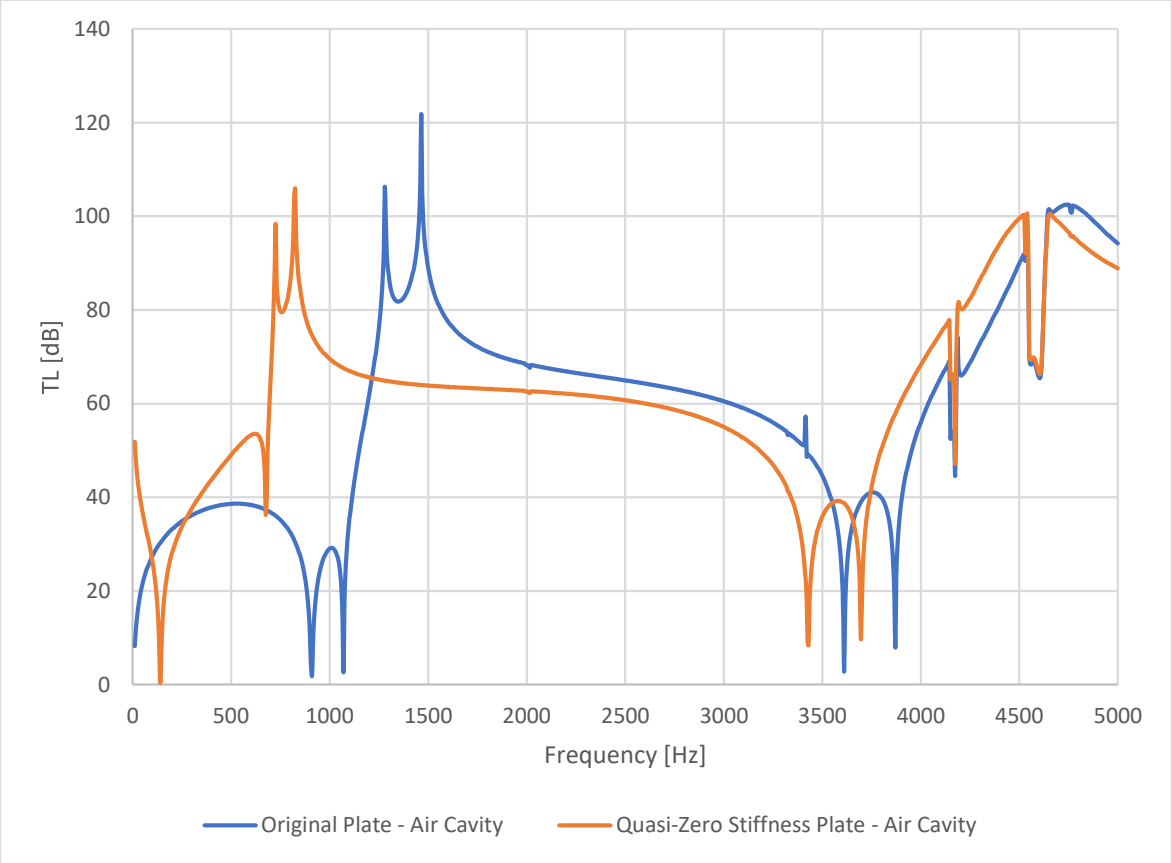


Figure 3.8. Coupled partition – transmission loss of original plate with 1 atm cavity pressure and quasi-zero stiffness plate with 1 atm cavity pressure.

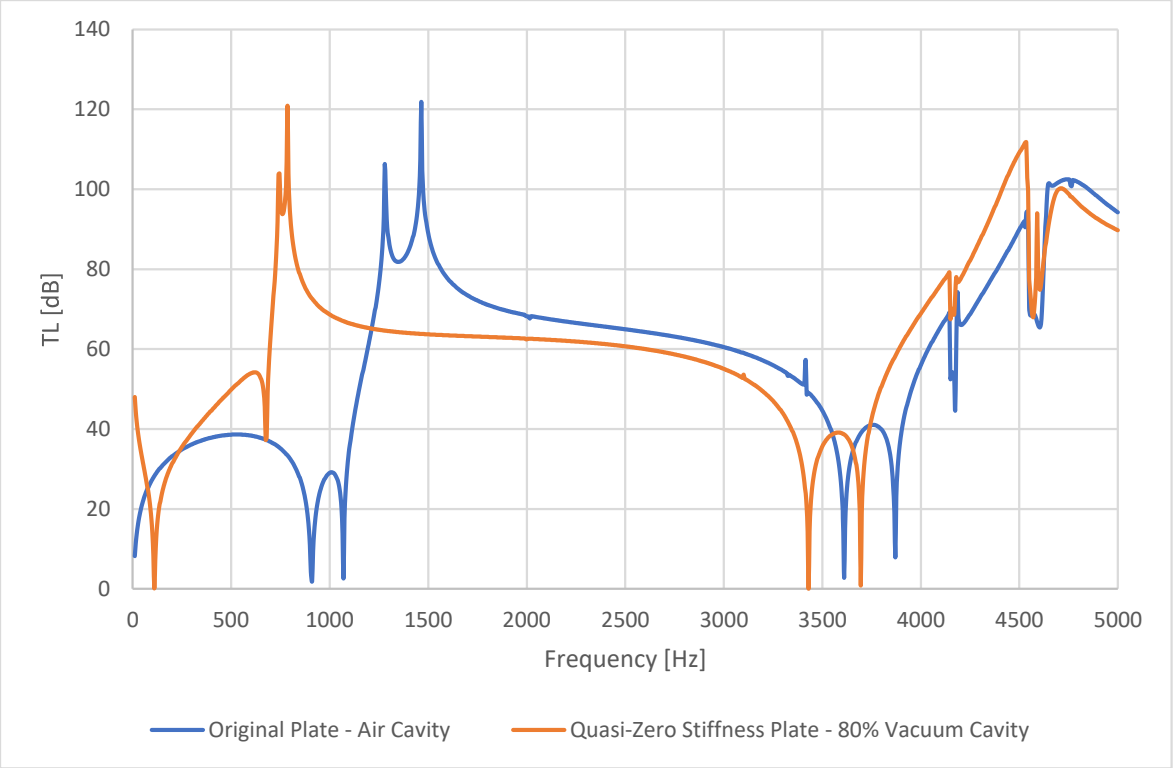


Figure 3.9. Coupled partition – transmission loss of original plate with 1 atm cavity pressure and quasi-zero stiffness plate with 0.2 atm cavity pressure.

3.2. Structural Finite Element Analyses

Structural finite element analyses were run to generate the optimal partition design. The most important property of the partition is the fundamental natural frequency. The partition must present low transverse stiffness, which lowers the natural frequency of the fundamental mode and enhances the insulation properties for low frequencies. The mode with the radial order greater than 0 is shown not to interfere with the transmission loss. However, the second circumferential mode (0,2), which is located by the mid frequency range of 3 – 5 kHz for the plates with the dimension of interest, greatly lowers the transmission loss. Therefore, an effective low frequency sound isolation partition should have a low fundamental frequency and following circumferential modes as high as possible.

The partition is conceptualized to perform under atmospheric pressure loading. With this expectation, two main criteria arise: structural integrity and sealing. The elastic limits should not be exceeded to ensure the reusability and predictability of the partition. Manageable stresses under at least 80% vacuum (or the designated optimal pressure level)

are considered. In this study, the material is selected as deep drawn 430 stainless steel, which can provide approximately 200-300 MPa yield strength. As for sealing, the partitions are thought to be better if consisted of a single body. In terms of manufacturability, the partitions are selected as monolithic lids that could be integrated to an appropriate body through o-rings.

In order to achieve low transverse stiffness under atmospheric pressure loading, a design with non – linear stiffness needs to be utilized. This can be achieved by circular geometries which can fit inside impedance tubes for acoustic measurement. The suitable designs of such traits are found to be convexly deformed plates. Various forms of convex diaphragm shapes are investigated in this section. The parametric studies were carried out with dimensions that could be achieved in prototype manufacturing.

Structural response and dynamic character of two different partitions are investigated with finite element analyses. Structural response was investigated via static structural analyses. Since the dynamic character of the partition depended heavily on the applied pressure, preloaded modal analyses were conducted to acquire the natural frequencies and mode shapes. All structural analyses were run on ANSYS Workbench software. The methodology is as follows:

- Generating the suitable partition geometry,
- Investigating how the dimensions influence the force/displacement response,
- Checking the stress levels,
- Designating the optimal dimensions for at least 80% vacuum pressure loading,
- Analyzing the mode shape and natural frequencies.

The partition is to be loaded by vacuuming the interior cavity and subjected to remaining atmospheric pressure accordingly. The force displacement response or the partition is obtained by gradual pressure loading via structural finite element analyses. Increased pressure load is applied step by step in a quasi-static manner. At each step, displacement of the feature which is associated transverse stiffness is calculated. The order to observe the varying stiffness, the loading range for all analyses is specified as 0 to 2 atm pressure.

The above analysis holds a couple of challenges. The negative stiffness property of the investigated forms, which provides lower stiffness by increased loading, also reduces the stability. Such forms tend to buckle if the dimensions are not chosen accordingly. This buckling behavior cannot be observed by pressure/force loading because the structure deforms rapidly to next stable position as shown in Figure 3.10 [64]. Displacement loading could have been applied and equivalent pressure loads could have been computed by strain energy methods. Yet for the load levels which the partition deforms in a rather complex manner reduces the accuracy of such assumptions. For this purpose, only the dimensions that does not snap under the gradual pressure loading are presented throughout this thesis. The loading is such that the effecting direction changes with the deformation of the structure. The partition under the relatively high magnitudes of pressure loading is expected to deform significantly. Such deformation alters both the structures stiffness and the direction of the applied load. Appropriate computational methods are employed to obtain accurate results.

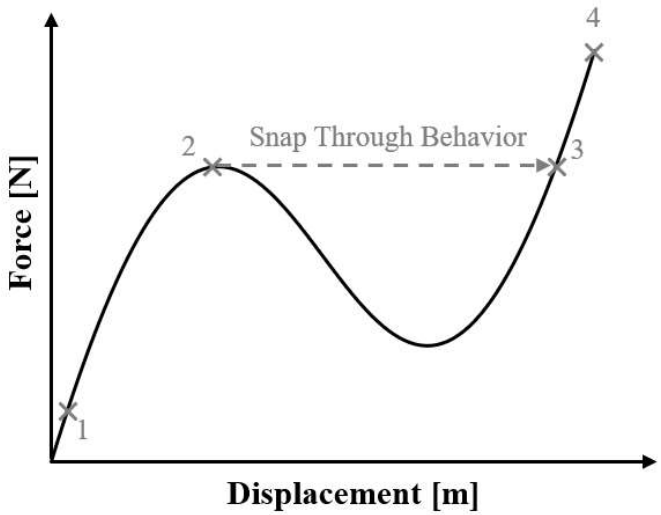


Figure 3.10. Snap through behavior of buckled structure.

After the force – displacement investigations, the optimum partition dimensions for low stiffness by at least 80% vacuum (0.2 atm absolute pressure) are designated. Mode shapes and natural frequencies of the partition in such loading is computed by preloaded modal analyses. The transverse stiffness and the natural frequency changes drastically in the critical loading range. Gradual pressure loading with 0.005 atm is applied to closely examine this range. In order to capture the optimum pressure load for the lowest attainable stiffness,

consecutive modal analyses were run at each loading step. Maximum Von Mises stresses and natural frequencies are computed for each loading step. The mode shape and occurring Von Mises stress maps are obtained for further investigations.

The mesh size for all presented computations is 0.8 mm. The material definition is fully elastic. Even though the stresses may rise above the yielding limit at full scale load, it is assured/controlled that the region of interest (low stiffness region) remains under the yield strength. Therefore, the method of observing the effect of various dimensions on stiffness behavior by force – displacement response is kept valid. Nonlinear computations are utilized by the "large deflection" option.

3.2.1. Truncated Conical Diaphragm

The diaphragm is modeled as a lid for practical applicability. Outer diameter is set to 100 mm as it was in the initial acoustic analyses. The height of the outer cylindrical wall is set to 10 mm. A radius of 1 mm is created between the outer wall and edges of the diaphragm to reduce the stress concentration. The geometry is generated as a surface and modeled as a thin shell in finite element analyses. The surface normal of the diaphragm points towards positive y direction. The thin shell definition of the given surface is set to graduate from the bottom surface. The material is selected as fully elastic steel (Young Modulus: 200 GPa, Poisson Ratio: 0.3, Density: 7850 kg/m^3).

Loads and boundary conditions are applied in the same manner for both static structural and preloaded modal analyses. The general view of the diaphragm is provided with loads and boundary conditions applied in Figure 3.11. The structural load is applied as uniformly distributed pressure on the outer surfaces. The displacement response to track the stiffness behavior is chosen as the inner diameter edge. Since this feature is axisymmetric, the downward displacement derived is constant through. Equivalent boundary condition for the lid being tight fitted to a rigid outer shell is applied as clamped from the edges of the edges of the outer wall. The dimensions to be altered through investigation are diaphragm thickness, apex height and inner radius. These dimensions are shown on the diaphragm cross section in Figure 3.12.

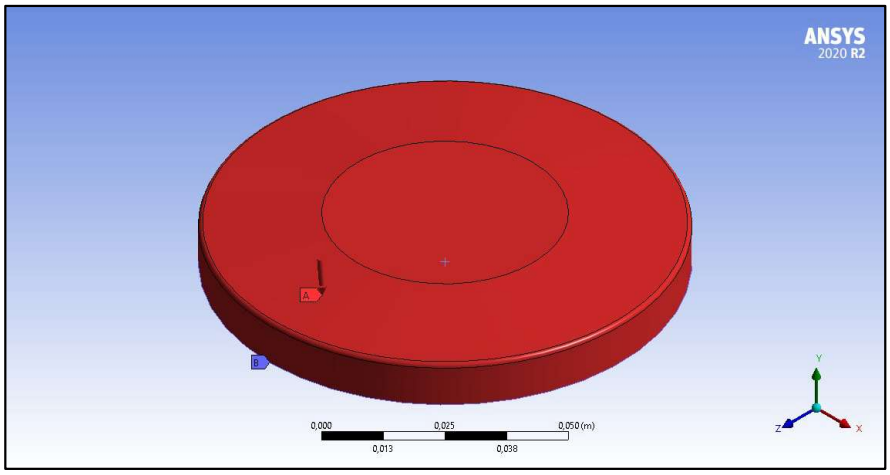


Figure 3.11. General view of the truncated conical diaphragm.

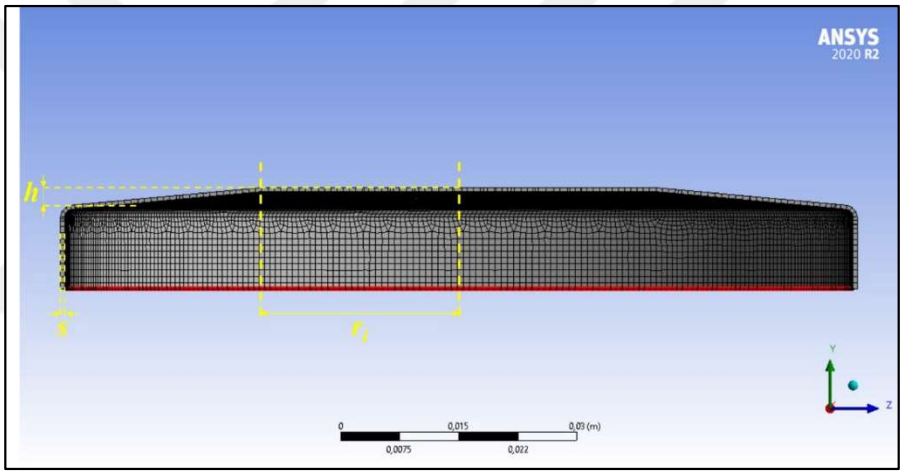


Figure 3.12. Truncated conical diaphragm dimensions.

First investigation is the effect of diaphragm thickness. 4 cases are presented in Figure 3.13 where the thickness is increased by 0.025 mm increments. The apex height and inner radius dimensions are fixed at 2.1 mm and 25 mm, respectively. As thickness increases, both stiffness and static load capacity increases. For low thickness values such as 0.55 mm, snap action is observed which can be seen as flat portion on the curve.

Next investigation is the effect of apex height. 4 cases are presented in Figure 3.14 where the apex height is decreased by 0.1 mm increments. The thickness and inner radius dimensions are fixed at 0.55 mm and 25 mm respectively. As the apex height decreases, stiffness increases but static load capacity decreases. Apex height greater than 2.1 mm causes the diaphragm to snap.

Final investigation is the effect of inner diameter. 4 cases are presented in Figure 3.15 where the inner diameter is increased by 1 mm increments. The thickness and apex height dimensions are fixed at 0.55 mm and 2.1 mm respectively. As the inner diameter increases, stiffness and static load capacity also increases. Inner radius of less than 25 mm causes the diaphragm to snap.

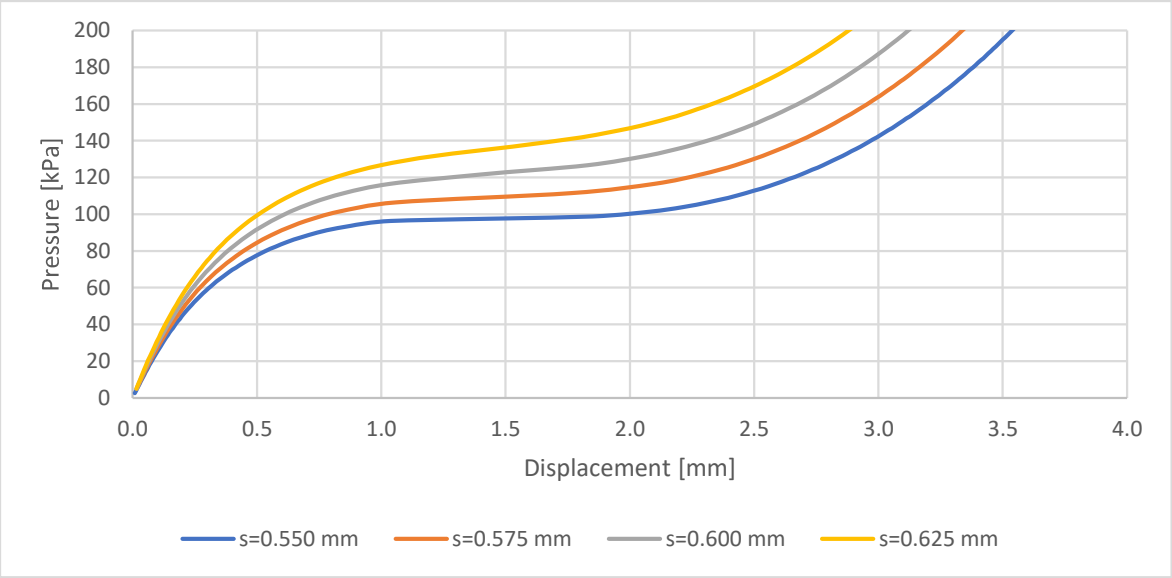


Figure 3.13. Effect of diaphragm thickness on pressure – displacement curve of truncated conical diaphragm for h=2.1 mm and r_i=25 mm.

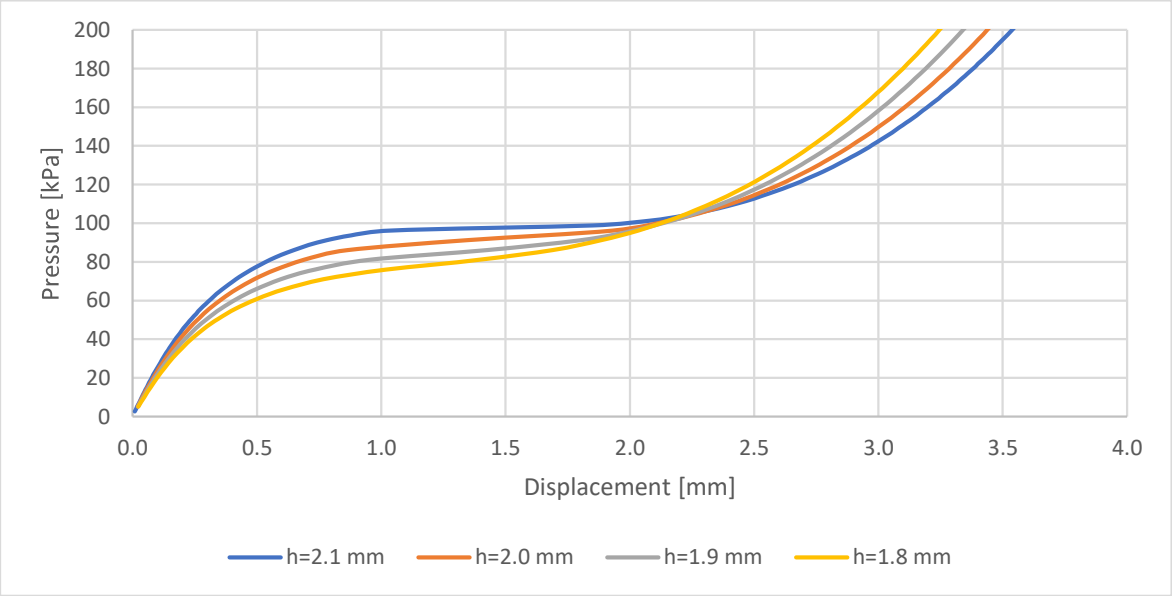


Figure 3.14. Effect of apex height on pressure – displacement curve of truncated conical diaphragm for s=0.55 mm and r_i=25 mm.

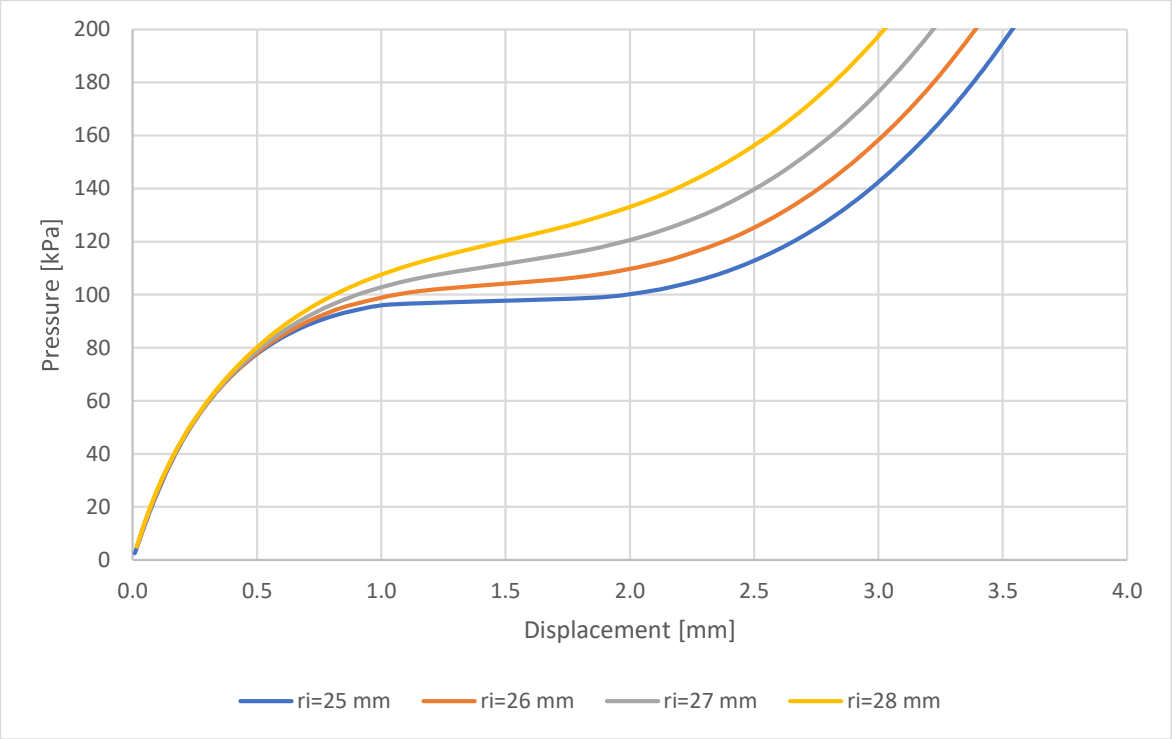


Figure 3.15. Effect of inner radius on pressure – displacement curve of truncated conical diaphragm for s=0.55 mm and h=2.1 mm.

Consecutive preloaded modal analysis results for the optimum case (s = 0.55 mm, h = 2.1 mm, r_i = 25 mm) are carried out. The applied pressure ranges from 80% to 100% vacuum. Computed natural frequencies and stresses are provided in Figure 3.16 and Figure 3.17, respectively. The critical pressure for the given diaphragm is computed as 96.5% vacuum. The first natural frequency decreases up to the critical pressure load and proceeds to increase above the critical pressure. This trend is followed by the second mode as well, yielding the lowest frequency at critical pressure loading. The gradually increasing maximum stress escalates rather rapidly when the pressure reaches the critical value. The maximum stress under this load is 408 MPa, which is above the expected elastic limit. Nevertheless, finite element analyses are conducted assuming elastic deformations. The stress plot of this load step is given in Figure 3.18. Here, the maximum Von Mises stress is seen to occur on the vicinity of the inner radius edge and the inner surface of the circumference radius. The mode shape plots for the critical pressure are provided in Figure 3.19.

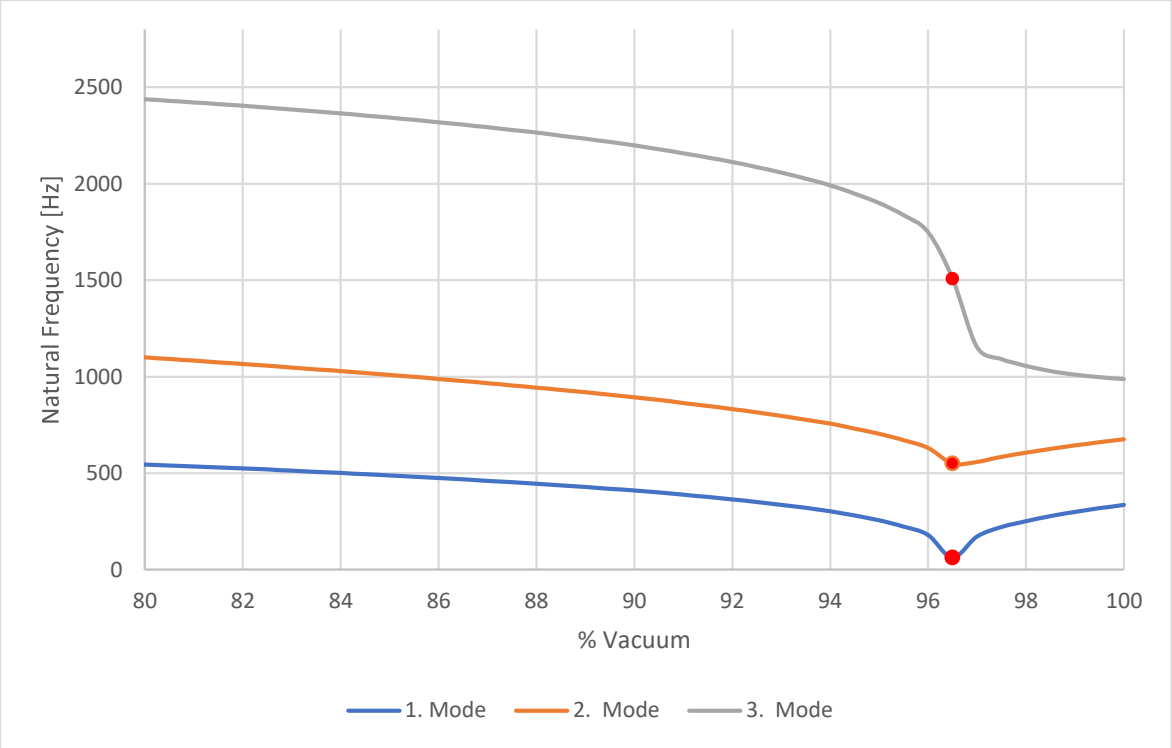


Figure 3.16. Natural frequencies with incremental pressure loading (96.5% vacuum; 63 Hz, 550.3 Hz, 1508.5 Hz).

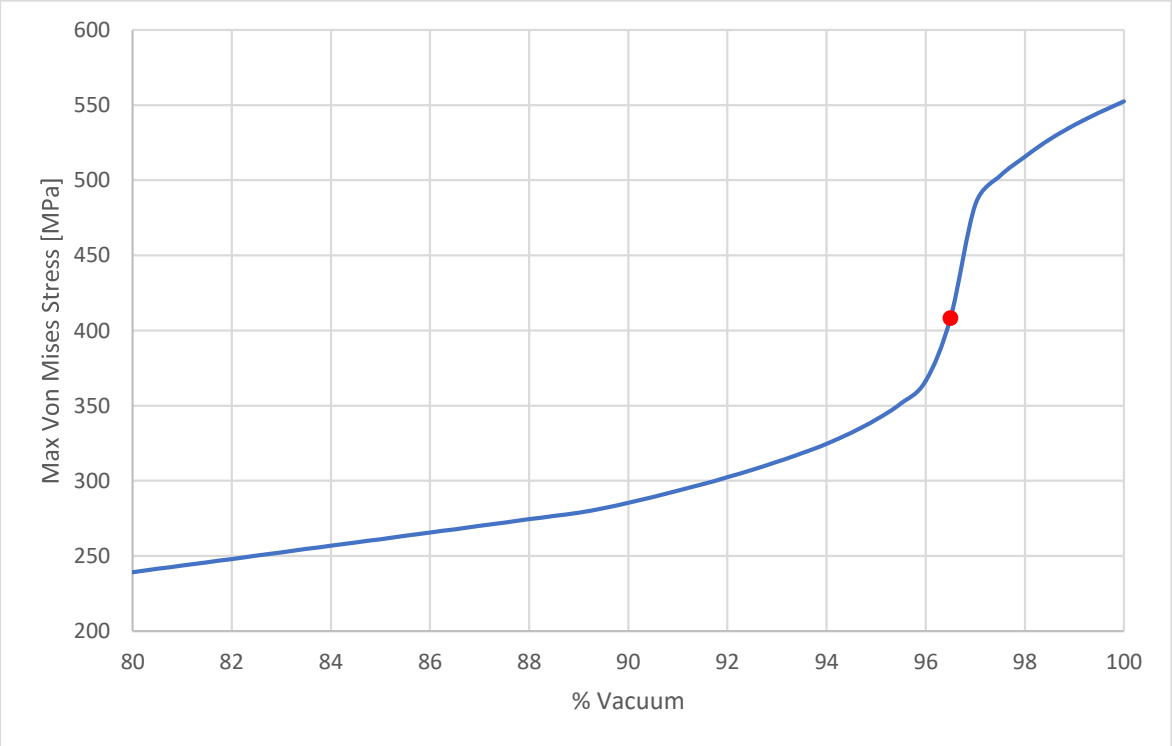


Figure 3.17. Max von Mises stress with incremental pressure loading (96.5% vacuum; 408.1 MPa).

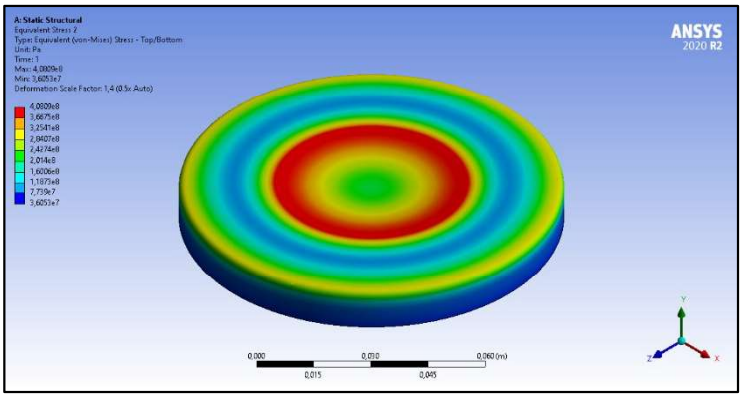
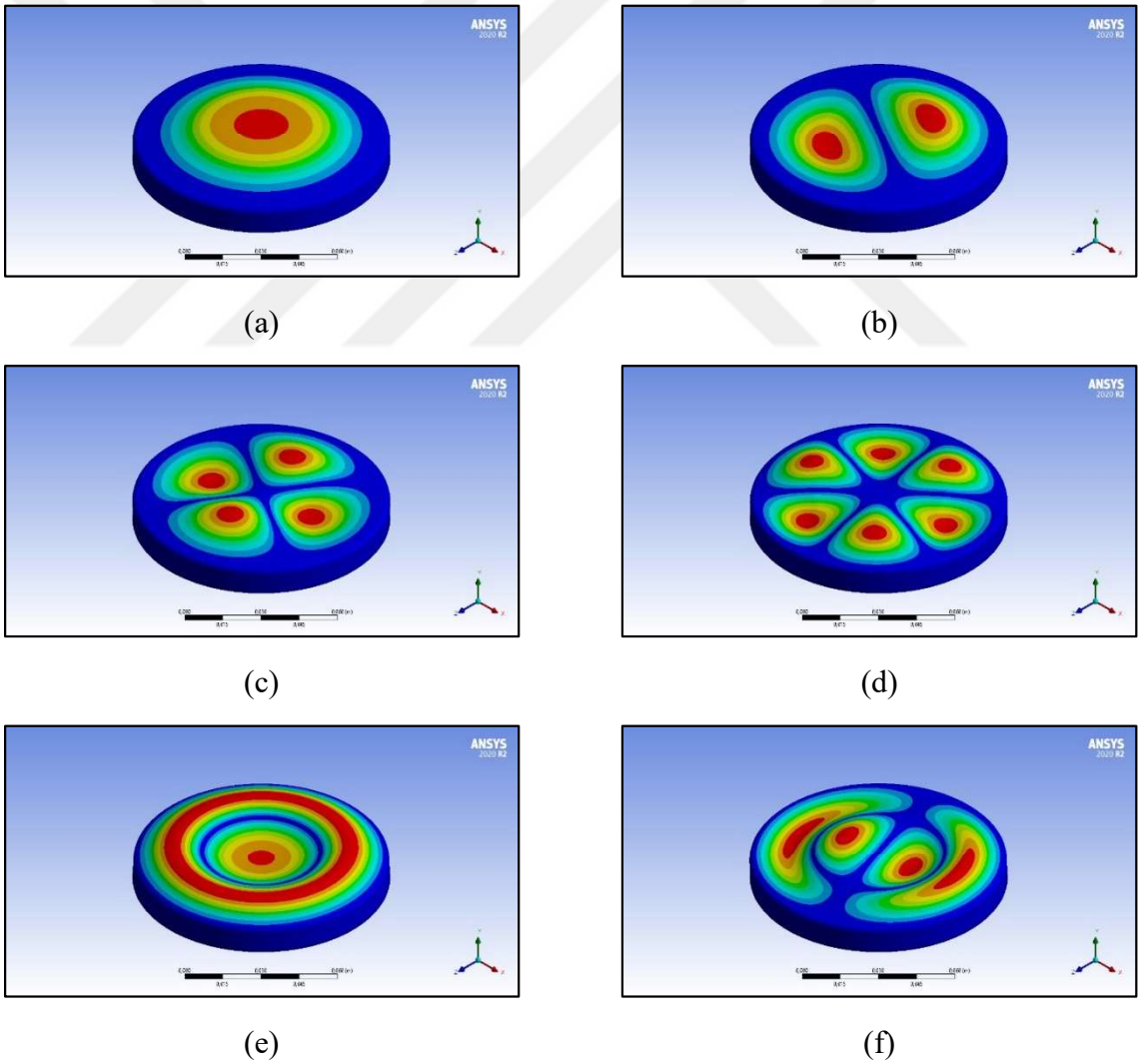


Figure 3.18. Von Mises stresses of the critically loaded truncated conical diaphragm.



(a) (b)

(c) (d)

(e) (f)

Figure 3.19. Mode shapes of the critically loaded truncated conical diaphragm, (a) 1st mode shape, (b) 2nd mode shape, (c) 3rd mode shape, (d) 4th mode shape, (e) 5th mode shape, (f) 6th mode shape.

3.2.2. Conical Diaphragm

The diaphragm is modeled as a lid and the outer radius is set to 50 mm. The height of the outer wall is set to 10 mm. A radius of 1 mm is created between the outer wall and edges of the diaphragm. The tip of the conic shape is rounded by 1 mm radius tangential sphere for ease of convergence. The geometry is generated as a surface and modeled as a thin shell. The surface normal of the diaphragm points towards positive *y* direction. The thin shell definition of the given surface is set to graduate from the bottom surface. The material is set to fully elastic steel (Young Modulus: 200 GPa, Poisson Ratio: 0.3, Density: 7850 kg/m^3).

Loads and boundary conditions are applied in the same manner for both static structural and preloaded modal analyses. The general view of the diaphragm is provided with loads and boundary conditions applied in Figure 3.20. The structural load is applied as uniformly distributed pressure on the outer surfaces. The displacement response to track the stiffness behavior is chosen as the boundary of the tangential spherical surface around the tip of the cone peak. Equivalent boundary condition for the lid being tight fitted to a rigid outer shell is applied as clamped from the edges of the outer wall. The dimensions to be altered through investigation are thickness, apex height and inner radius. These dimensions are shown on the diaphragm cross section in Figure 3.21.

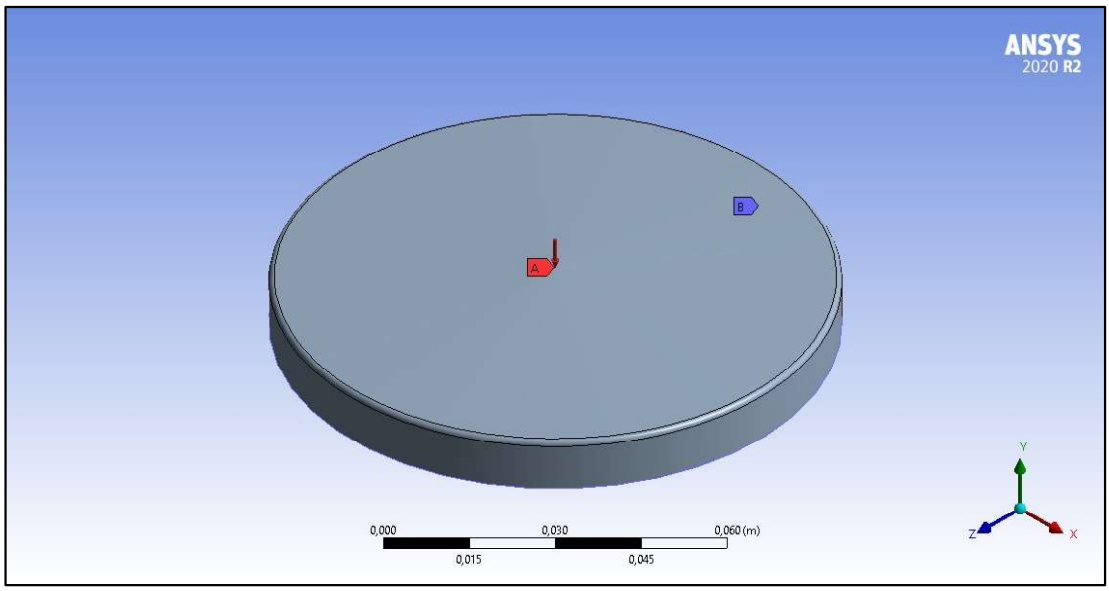


Figure 3.20. Conical diaphragm general view.

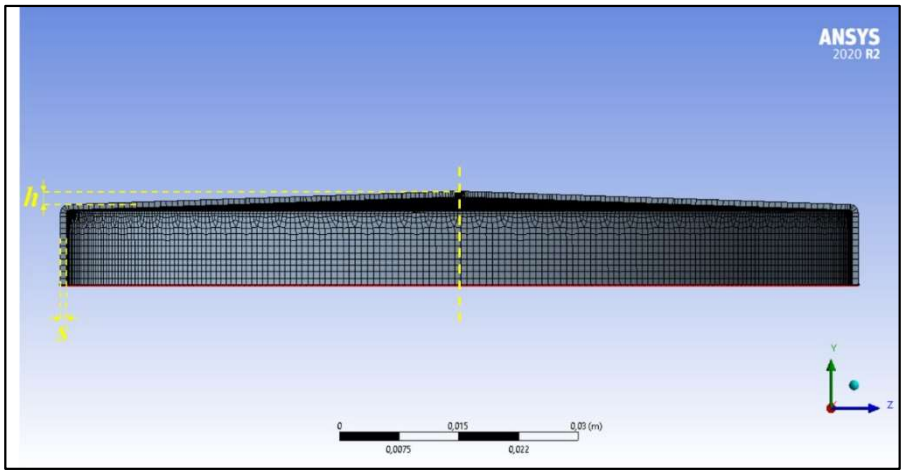


Figure 3.21. Conical diaphragm dimensions.

First investigation is the effect of diaphragm thickness. 4 cases are presented in Figure 3.22 where the thickness is increased with 0.025 mm increments. The apex height is fixed at 1.8 mm. As thickness increases, both stiffness and static load capacity increases. Thickness values less than 0.7 mm causes the diaphragm to snap. Notice that quasi-zero stiffness is achieved around $h = (1.8/0.7)s = 2.57s$. In Section 2.5, clamped conical diaphragms were investigated and quasi-zero stiffness was achieved at $h = 1.84s$. Hence, convexity ratio (h/s) for the finite element model of the lid shaped diaphragm is 40% higher compared to the clamped conical diaphragm in Section 2.5.

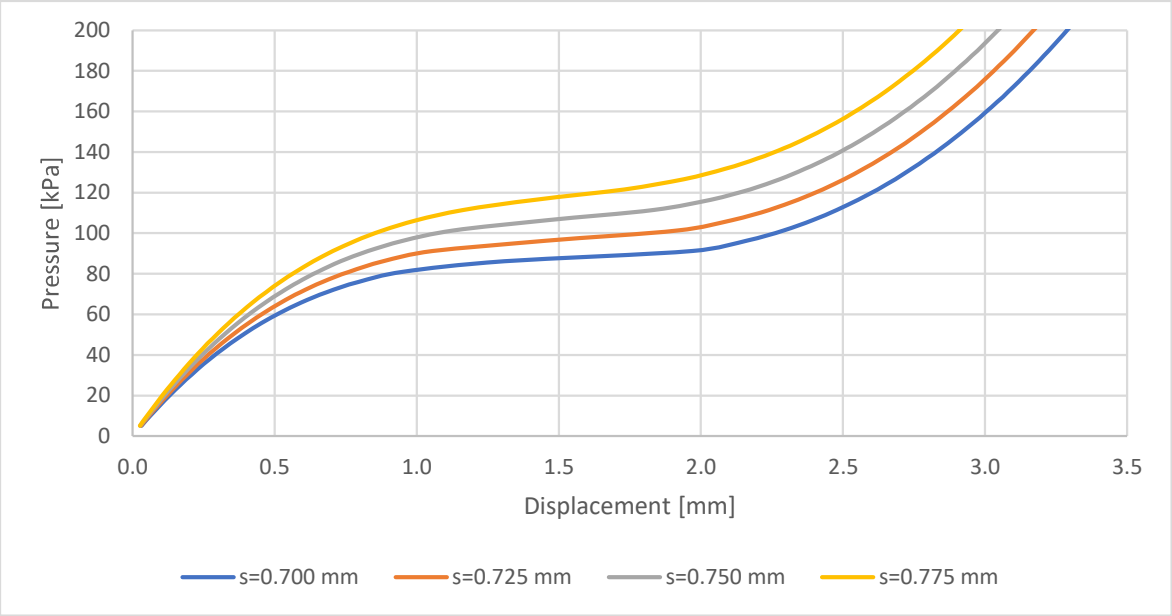


Figure 3.22. Effect of diaphragm thickness on pressure – displacement curve of conical diaphragm for h=1.8mm.

Next investigation is the effect of apex height. 4 cases are presented in Figure 3.23. where the apex height is decreased with 1 mm increments. The thickness is fixed at 0.7 mm. As the apex height decreases, stiffness increases while static load capacity decreases. The displacement range where quasi-zero is observed narrows down with decreased apex height.

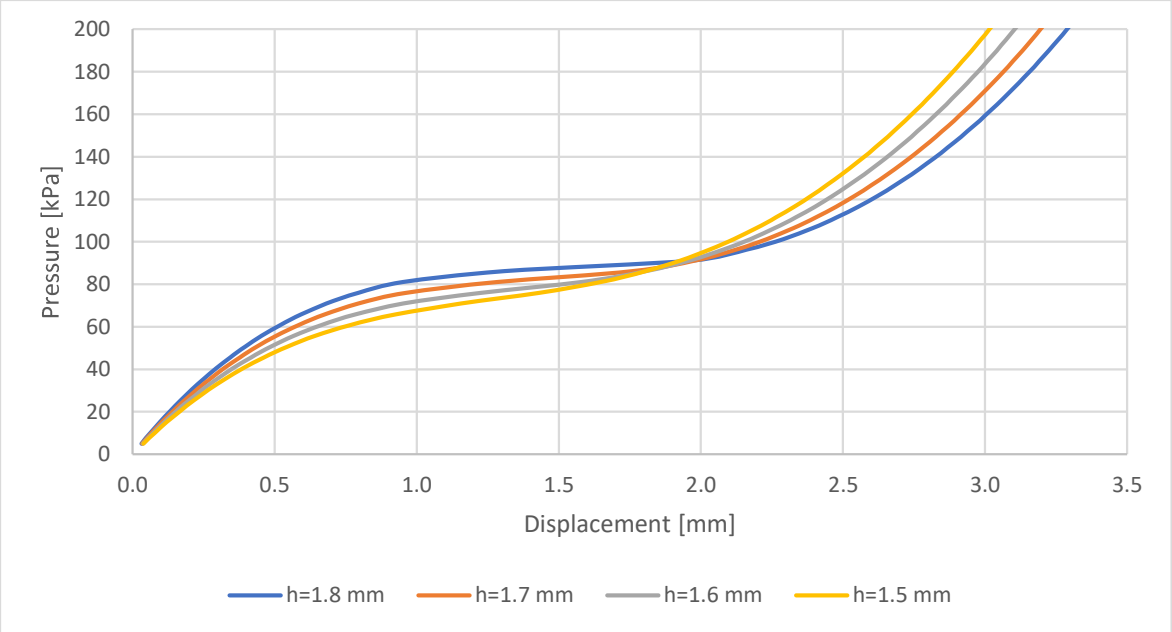


Figure 3.23. Effect of diaphragm apex height on pressure – displacement curve of conical diaphragm for s=0.7mm.

Preloaded modal analysis results for the optimum case (s = 0.7 mm, h = 1.85 mm) are carried out. The applied pressure ranges from 80% to 100% vacuum. Computed natural frequencies and stresses are provided in Figure 3.24 and Figure 3.25. The critical pressure for the given diaphragm is computed as 86% vacuum. The first natural frequency decreases up to the critical pressure load and proceeds to increase above the critical pressure. Obtained fundamental natural frequency is 117.6 Hz. Second mode shape also yields the minimum frequency by the critical pressure loading. The maximum stress read under this load is 298 MPa, which is manageable compared to the truncated conical diaphragm. The stress plot of this load step is given in Figure 3.26. Here, the maximum Von Mises stress is seen to occur below the apex region and inner surface of the circumference radius. The stress levels rise excessively beyond the critical pressure. However, finite element analyses are conducted assuming elastic deformations. The mode shape plots for the critical pressure are provided in Figure 3.27.

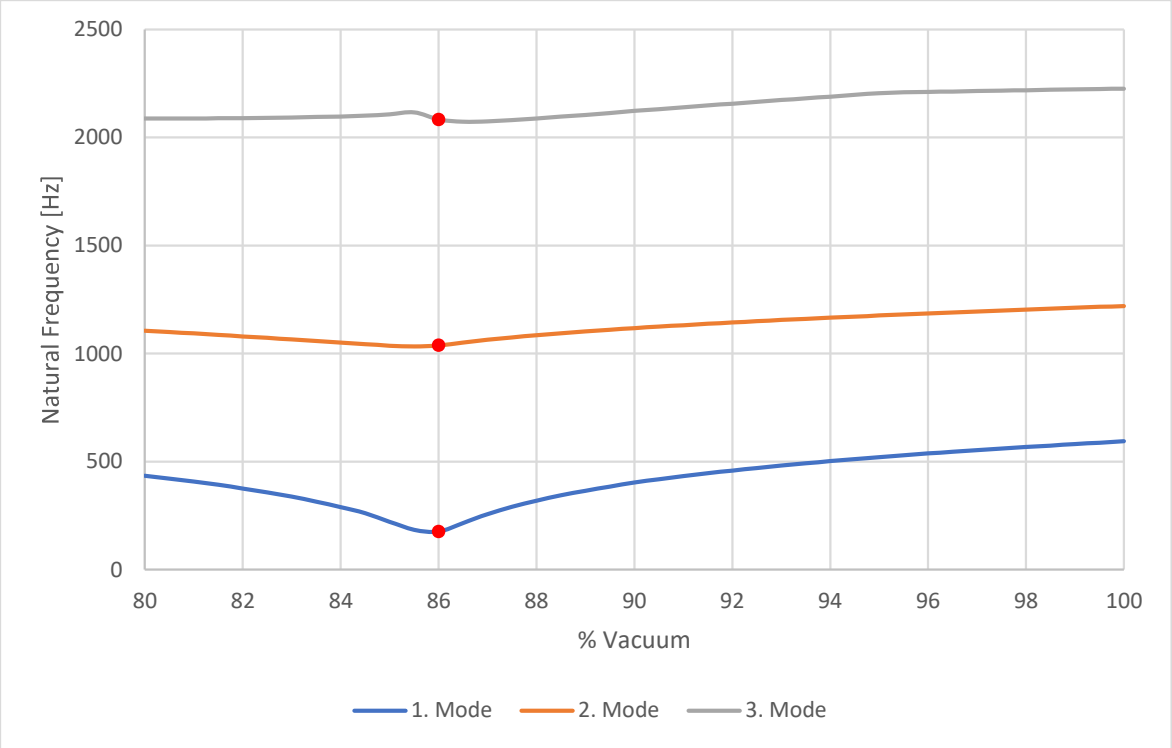


Figure 3.24. Natural frequencies with incremental pressure loading (86% vacuum; 117.6 Hz, 1013.5 Hz, 2098.6 Hz).

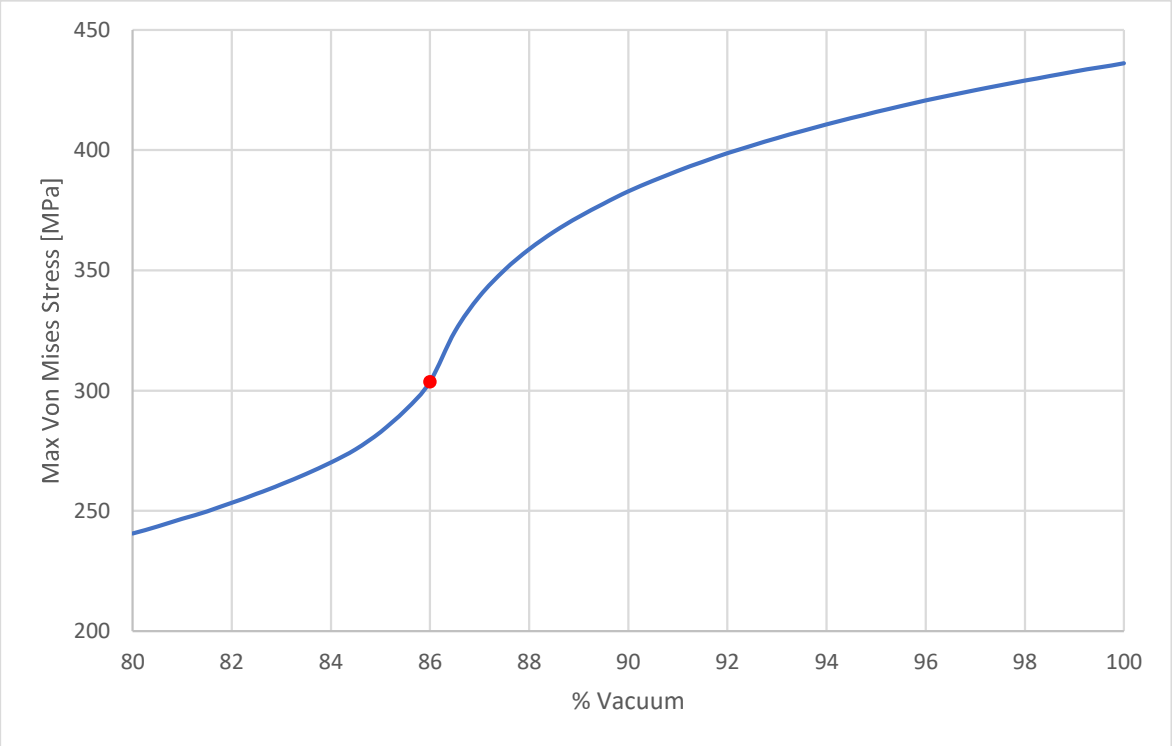


Figure 3.25. Max von Mises stress with incremental pressure loading (86% vacuum; 298.3 MPa).

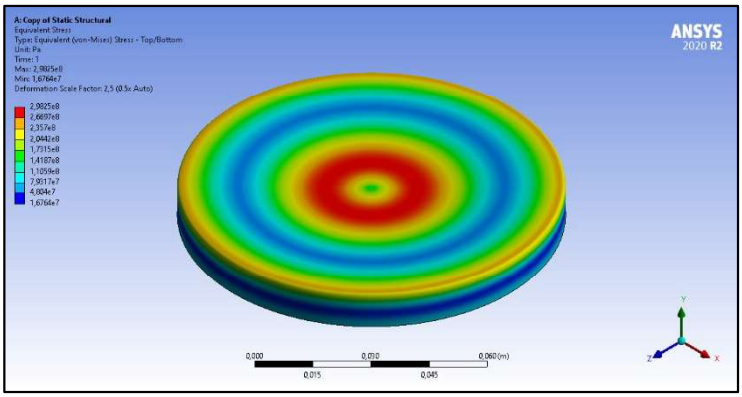
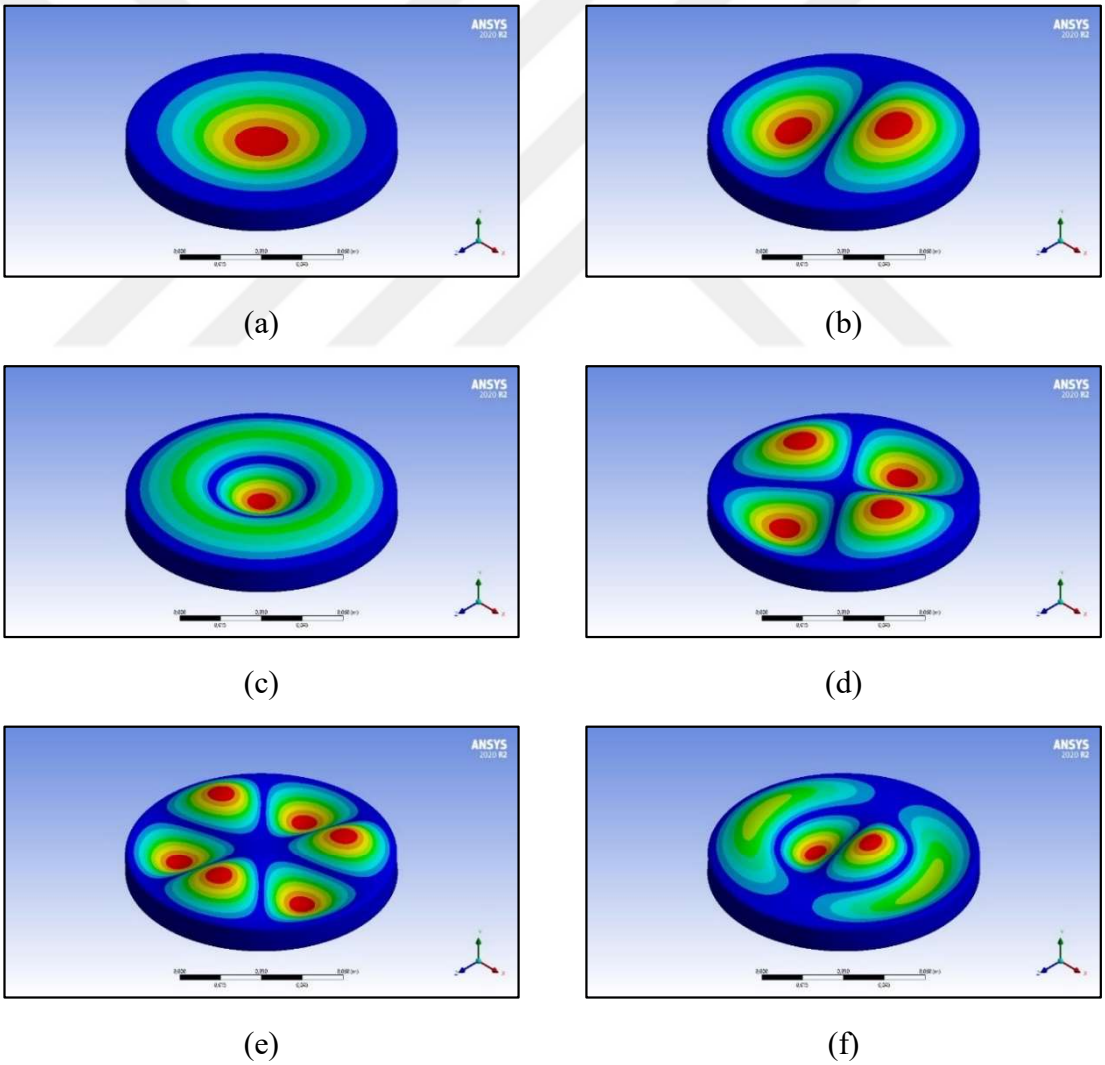


Figure 3.26. Von Mises stresses of the critically loaded conical diaphragm.



(a) (b)

(c) (d)

(e) (f)

Figure 3.27. Mode shapes of the critically loaded conical diaphragm, (a) 1st mode shape, (b) 2nd mode shape, (c) 3rd mode shape, (d) 4th mode shape, (e) 5th mode shape, (f) 6th mode shape.

4. EXPERIMENTAL STUDIES

Manufactured prototypes, measurement methods and experimental results are presented in this section. Three specimens have been manufactured. The configurations and dimensions of each specimen are described. Achieved transmission loss characteristics by tuning the non – linear stiffness diaphragm to the critical vacuum load is shown.

4.1. Manufactured Prototypes and Test Setup

The transmission loss measurements are carried out via the commercial impedance tube TestSens. The measurement setup is shown in Figure 4.1. The measurements are done in accordance with ASTM E-1050 and ISO 10534-2. The impedance tube consists of 4 parts. The acoustic plane wave excitation is provided by a speaker source in the first (far left) part of the tube. Circular specimens are placed in the sample holder part, which is the 3rd part of the tube. 2 microphones are placed before (on the 2nd part of the tube) the sample holder and 2 microphones are placed after (on the 4th part of the tube) the sample holder. GRAS 46BD ¼" CCP Pressure Standard microphones were utilized in the measurements. Transmission loss calculations are completed in the TestSens software by the transfer function method. Computed curves were export as narrowband spectra for additional investigations.



Figure 4.1. Transmission loss measurement test setup.

Three specimens have been manufactured. The outer diameters of the specimens should be slightly less than 100 mm to fit inside the impedance tube. Specimen 1 initially had 102 mm diameter. Roll forming was used to reduce its outer diameter to 99.5 mm, which is ideal in terms of fitting smoothly. Outer diameters of specimens 2 and 3 are 99.1 mm and 93.75 mm respectively, leaving some space between the sample holder surface. Paper tape is applied to these specimens to fill the gaps. The specimen's dimensions of interest are given in Table 4.1. Conical shape of the diaphragm is presented by a close-up image of Specimen 1 in Figure 4.2. The specimens and the mentioned outer diameter adjustment can be seen in Figure 4.3.

Table 4.1. Specimen dimensions.

Dimension/Specimen	**Specimen 1**	**Specimen 2**	**Specimen 3**
Diaphragm Thickness	0.7 mm	0.5 mm	0.7 mm
Apex height	1.9 mm	1.2 mm	2 mm
Cavity Width	70 mm	62 mm	53 mm
Bottom Thickness	22 mm	24 mm	23 mm
Outer Diameter	99.5 mm	99.1 mm	93.75 mm



Figure 4.2. Close up view of Specimen 1 showing the conical shape of the diaphragm.



(a)



(b)



(c)

Figure 4.3. Manufactured specimens left to right: 1, 2, 3, (a) assembled specimens, (b) disassembled specimens (top views) (c) disassembled specimens (bottom views).

The top surfaces of the specimens are conical diaphragms and the bottom surfaces are of thick flat walls. In other words, the specimens bear one active surface in terms of insulation by lowered stiffness. Manufacturing the conical diaphragms with exact dimensions was a challenge. The manufactured specimens with one active diaphragm provide a more controlled testing approach considering the results depend heavily on only the one active diaphragm rather than two. Specimen 1 consists of a lid shaped diaphragm and a cylindrical cup shaped body. The cylindrical wall thickness is 6 mm and the bottom wall thickness is 22 mm. The lid fits to the cup through an o-ring that provides sealing. This cup structure is constructed from aluminum and the diaphragm material is steel. Specimens 2 and 3 on the other hand are designed such that the thick surface below is disk shaped. The diaphragms of these specimens are the top surface of an inverted cup shaped structure, which fits to the mentioned thick disk shaped bottom surface through o-rings. The bottom surfaces of Specimens 2 and 3 are made of 24 and 23 mm thick aluminum. Diaphragm and the conjoined outer wall are of steel and share the same thickness. All specimens have valves in their bottom surfaces so that vacuum pump can be used to reduce the pressure inside. The critical pressures of Specimen 1 and 3 are 70% and 80% vacuum, respectively. For these pressure levels, self-sealing of the valves are satisfactory. The critical pressure level of Specimen 2 is 10% vacuum and the valve cannot provide adequate sealing. In order to ensure proper sealing, a leaf spring is added that can exert compressive force on the valve.

95% vacuum can be achieved with the pump whose pumping speed can be controlled by a signal generator providing square wave control signal (see Figure 4.4a). In Figure 4.4b, the vacuum hose is attached to the valve to perform vacuum operation. When vacuumed, the transverse stiffness and accordingly the first natural frequency of the diaphragm decreases. The critical vacuum to obtain the lowest possible natural frequency depends on the specimen's geometric properties. The transverse stiffness of these specimens in comparison are Specimen 2 < Specimen 1 < Specimen 3. Although the minimum attainable natural frequency and critical vacuum vary, all specimens deform similarly under pressure loading. The diaphragm deformation under maximum and critical vacuum conditions of Specimen 1 are presented in Figure 4.5. The pump can provide maximum 95% vacuum. For this vacuum level, center of the lid moves to a lower level than the edges, generating a concave shape (see Figure 4.5a). This concave shape provides large stiffness. However, at the critical

vacuum level of 70%, center of the lid is at the same height with the edges (see Figure 4.5b) and this condition provides low stiffness.



(a) (b)

Figure 4.4 (a) Vacuum setup, (b) specimen vacuum application.



(a) (b)

Figure 4.5. Deformation under vacuum, (a) maximum vacuum (95%), (b) critical vacuum (70%).

Measuring solid/stiff samples is not a common practice for impedance tubes. For common measurements, the natural frequency of the sample is desired to be left out for

further material characterization studies. Conversely, observing the natural frequencies of the specimens is desired for the presented measurements. Hence, the diaphragm of the specimen should vibrate freely and the vacuum cavity should not rattle inside the impedance tube. Care is taken to ensure suitable contact between these surfaces. The outmost diameter of the specimen body is formed to be 0.5 – 1 mm less than the inner diameter of the impedance tube. Contact between the two bodies is achieved through o-rings placed on the outer surface of the specimens. This contact allows a rattle-free and air-tight fitting. The fitting of Specimen 1 is shown in Figure 4.6.



(a) (b)

Figure 4.6. Specimen fitting in impedance tube sample holder.

4.2. Experimental Results and Validation

Specimens were put under test in three different configurations: no vacuum, critical vacuum and full vacuum. The specimen cavity at no vacuum configuration is kept at atmospheric pressure. The critical vacuum configuration is the cavity pressure which the lowest possible fundamental frequency is obtained. Critical vacuum levels for each specimen are found by examining change in the first natural frequency with changing cavity pressure. As shown in Section 3.2, the fundamental frequency decreases with the increased vacuum up the critical pressure then increases after this level. In order to tune the specimen, full vacuum is applied to ensure concave shape of the diaphragm. Then, the valve is used to

release pressure gradually until the first natural frequency of the lid achieves minimum value. As the pressure is released, the concave shape of the lid gradually becomes flat and the center of the lid achieves the same height as the edges as shown in Figure 4.5b. During incremental pressure releases, the lid is tapped and its sound is analyzed by a spectrum analyzer. It is seen that the fundamental mode of the lid is minimized when its shape becomes as in Figure 4.5b. Moreover, it is observed that all three specimens have stayed perfectly elastic even after the applied full vacuum load.

For each specimen configuration, three transmission loss measurements are completed. Those three measurements were taken with the specimen placed in different axial positions in the sample holder. Three obtained transmission loss curves are then averaged linearly. The consistency of the three measurements and the averaged curve can be seen in Figure 4.7. Averaging provides better representation of the scatter as well as ruling out the local deviations on the transmission loss curves.

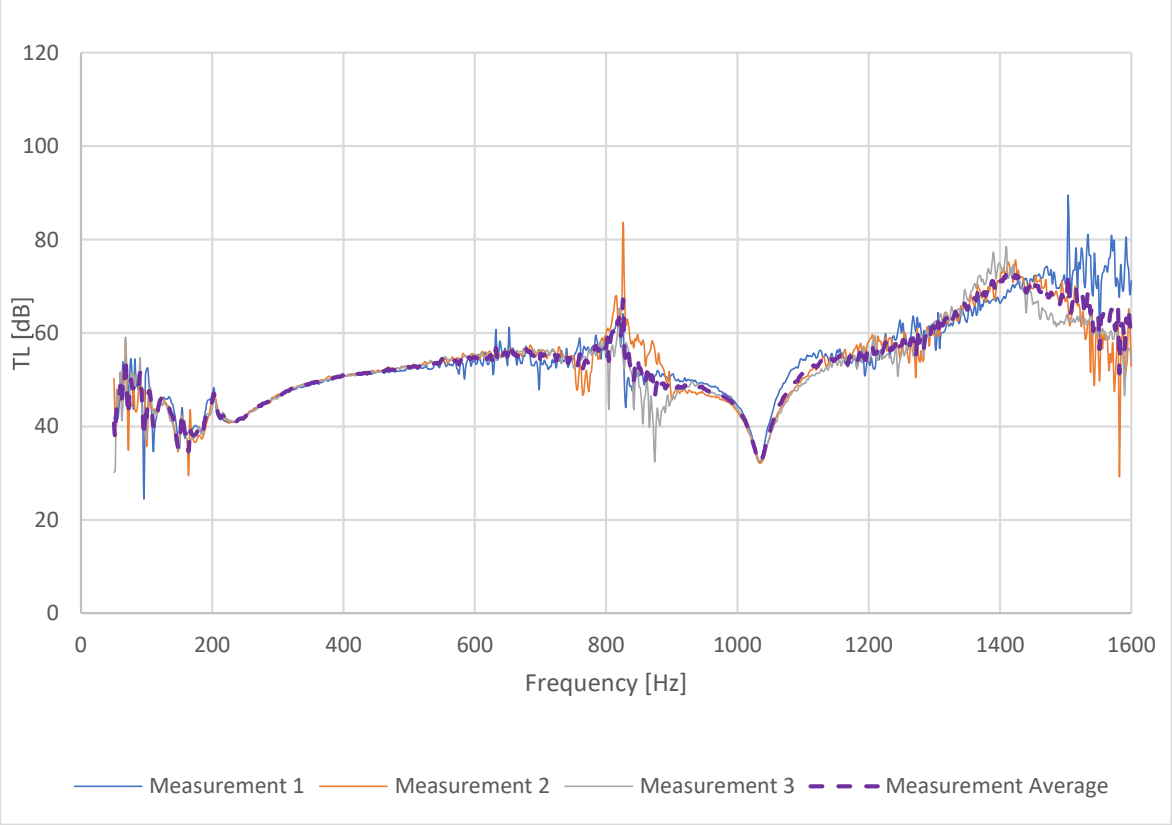


Figure 4.7. Transmission loss measurement – averaging.

Amplifier setting for the acoustic excitation element is set by prior measurements shown in Figure 4.8. The receiving side microphones are exposed to very low levels of sound pressure with low amplifier gain, which decreases the signal to noise ratio. Whereas high gain resulted in disorders in low frequency region. Averaging of each measurement is set to 96 buffers and the narrowband spectra resolution is set to 2 Hz. The valid range of transmission loss measurement for the given specimen and duct dimension is 1600 Hz.

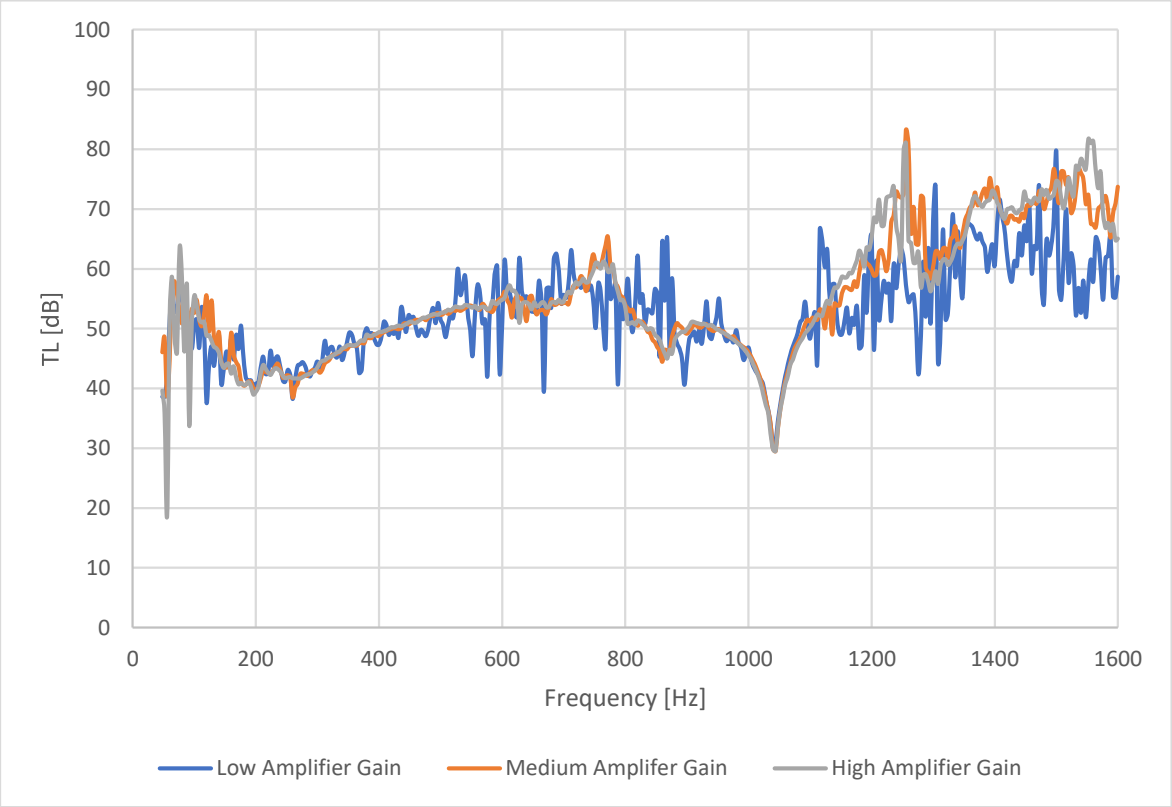


Figure 4.8. Transmission loss measurement – amplifier gain setting.

Measured transmission loss curves for Specimen 1, 2 and 3 are given in Figure 4.9, Figure 4.10 and Figure 4.11, respectively. For Specimen 1, the fundamental natural frequency for no vacuum condition is at 1034 Hz. The transmission loss reduction at this frequency is followed by a subtle increase, yielding maximum transmission loss at 1424 Hz. Observed transmission behavior shifts to the left with the application of vacuum. Fundamental natural frequency drops down to 738 Hz and 238 Hz with full and critical vacuum applications. The critical pressure of 70% vacuum (0.3 atm absolute pressure inside) provides an average transmission loss increase of 12.24 dB between 268 Hz – 1288 Hz compared to the no vacuum case. Maximum transmission loss difference is achieved at 318

Hz with 36.4 dB. With 1020 Hz bandwidth (268 Hz – 1288 Hz), Specimen 1 presents the widest frequency range in which transmission loss is enhanced compared to the no vacuum case. Specimen 1 under full vacuum starts to perform better than the no vacuum case after 856 Hz. As the aim in this thesis is to achieve high transmission loss at low frequencies, the critical vacuum case provides the best result.



Figure 4.9. Transmission loss measurements of Specimen 1.

The diaphragm thickness of Specimen 2 is 0.5mm, which is thinner than the other two specimens (0.7 mm). Therefore, Specimen 2 is the least stiff specimen with fundamental natural frequency of 704 Hz at ambient pressure. The first natural frequency can be lowered to 166 Hz by just 10% vacuum (0.9 atm absolute pressure inside). This is the lowest fundamental frequency acquired in this study. Compared to the no vacuum case, critical pressure loading of Specimen 2 increases transmission loss between 210 Hz – 810 Hz. The average provided enhancement in this 600 Hz bandwidth is 11.4 dB with the maximum of 27.1 dB at 698 Hz. Vacuuming the specimen to the full extent however results in a vast isolation decrease up to 1326 Hz. As the diaphragm is thin (0.5 mm), full vacuum generates a deep concave shape, which in turn results in a high fundamental frequency. It is also

observed that the fundamental frequency at the critical vacuum of 10% is greatly influenced by the slight changes in the temperature. Since the air density inside the cavity is close to the ambient air density, slight change in temperature can increase the pressure inside and moves the diaphragm away from its equilibrium position. This was not the case for the other specimens since much higher level of vacuum was required to achieve equilibrium position. In summary, higher vacuum level provides a more robust sound insulation structure.

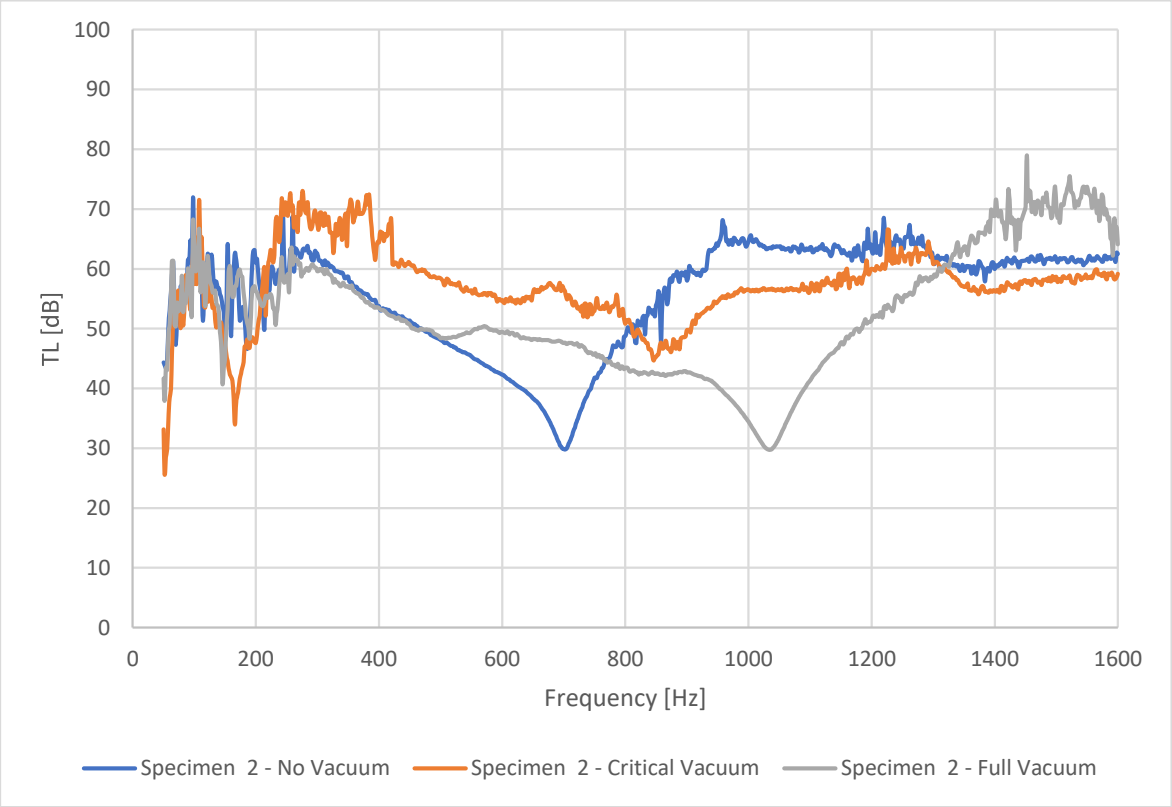


Figure 4.10. Transmission loss measurements of Specimen 2.

Specimen 3 has the fundamental natural frequency at 966 Hz. Its fundamental natural frequency can be lowered to 282 Hz under 80% vacuum (0.2 atm absolute pressure inside). An average of 11.43 dB increase in transmission loss compared to no vacuum case is obtained between 320 Hz – 1160 Hz. This bandwidth of 840 Hz is slightly narrower than 1020 Hz of Specimen 1. The maximum transmission loss increase acquired is 40.3 dB at 376 Hz, which is the greatest difference obtained in this study. When vacuumed to the full extent, fundamental natural frequency reaches 866 Hz, which is close to the no vacuum case. This specimen has the same diaphragm thickness (0.7 mm), but smaller diameter than Specimen 1 (93.75 mm vs 99.5 mm). Consequently, it is stiffer than Specimen 1 and requires a higher

critical vacuum level (80% vs 70%). As Specimen 3 is the stiffest specimen, full vacuum does not generate a deep concave shape, which in turn results in a relatively low fundamental frequency compared to the other specimens.

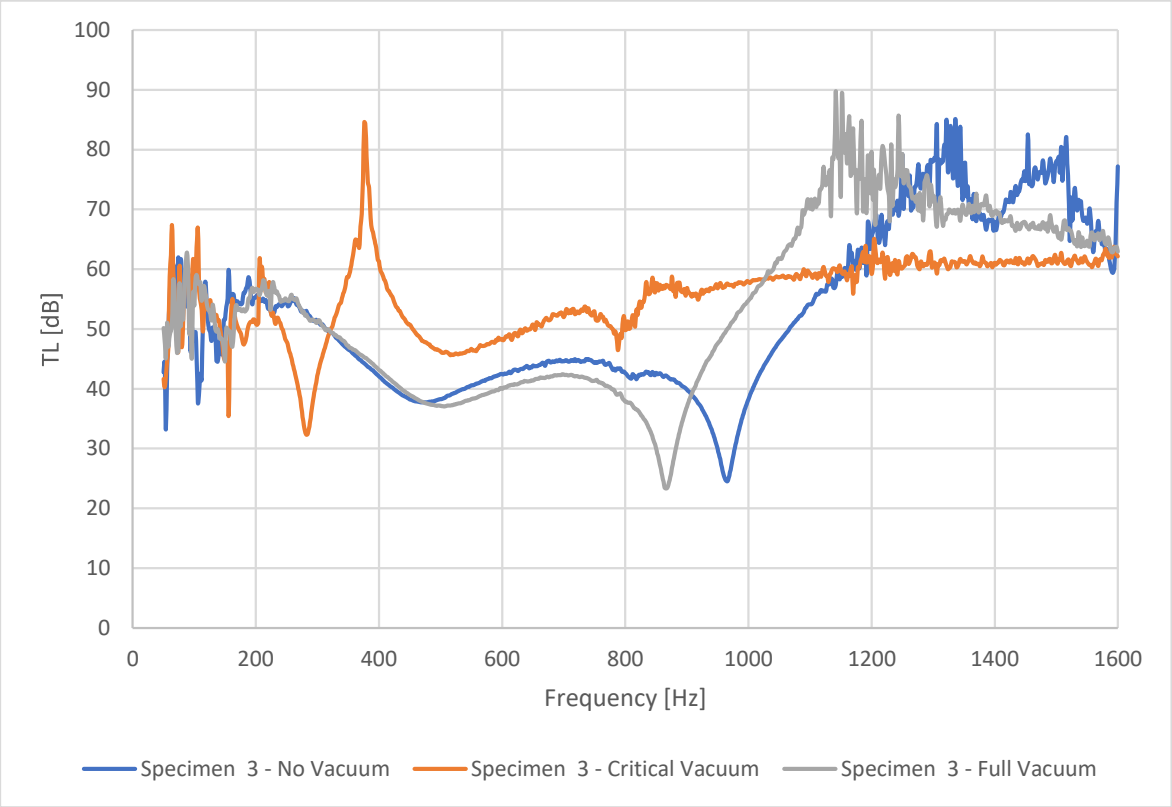


Figure 4.11. Transmission loss measurements of Specimen 3.

Acoustic finite element analyses are carried out to investigate the accuracy of the previously shown models. Specimen 1 is chosen for this validation study since it yielded the greatest bandwidth (1020 Hz) of transmission loss increase and ensured best fitting due with the outer diameter of 99.5 mm. Existing structurally coupled double partition finite element model is updated to represent Specimen 1. Aluminum material properties and appropriate dimensions are assigned to the coupling shell and the bottom surface. Diaphragm is modeled by the flat shell and existing external spring stiffness is tuned to obtain the fundamental natural frequencies of the specimen various vacuum conditions. Acoustic finite element analyses transmission loss curves of Specimen 1 are presented in Figure 4.12. Analysis and measurement transmission loss comparison of the no vacuum, critical vacuum and full vacuum conditions are given in Figure 4.13, Figure 4.14 and Figure 4.15, respectively.

Since the sound transmission and radiation in the frequency region of interest are influenced mainly by the fundamental mode (0,1) of diaphragm, the finite element model yielded fairly similar results with the experimentally measured curves. The trends of the transmission loss curves are in very good agreement with experiments. For all the cases, the dips due to the fundamental resonance modes are accurately predicted. Although the anti-resonance peak frequencies are accurately predicted in the no vacuum and full vacuum conditions, the experimental peak transmission loss values are not high as in the finite element model. The critical vacuum condition shows a more pronounced anti-resonance peak, however, there is some mismatch between the experimental and finite element anti-resonance frequencies. This mismatch is attributed to the change in stiffness of the lid due to the deformed shape of the diaphragm under pressure load, which cannot be exactly represented in the finite element model. Nevertheless, the general trends of all cases are predicted quite well with the finite element model.

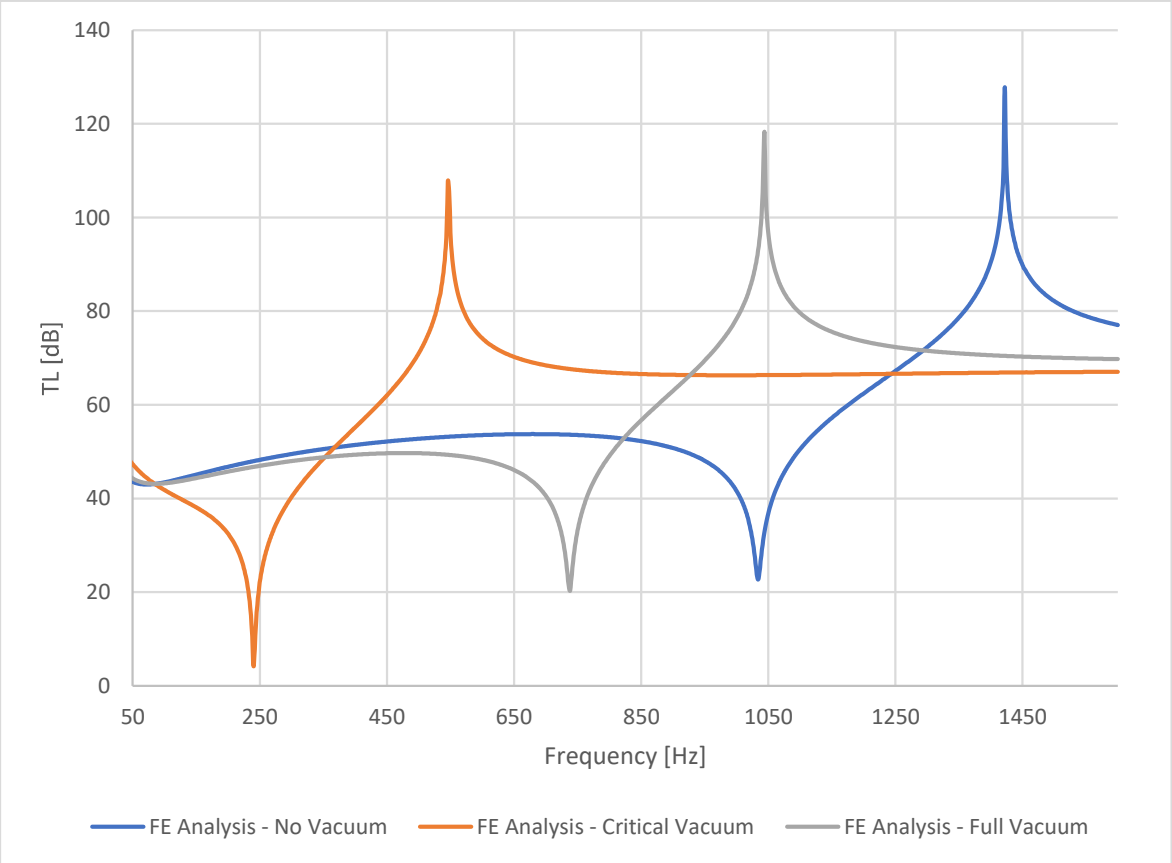


Figure 4.12. Specimen 1 – FE transmission loss analyses.

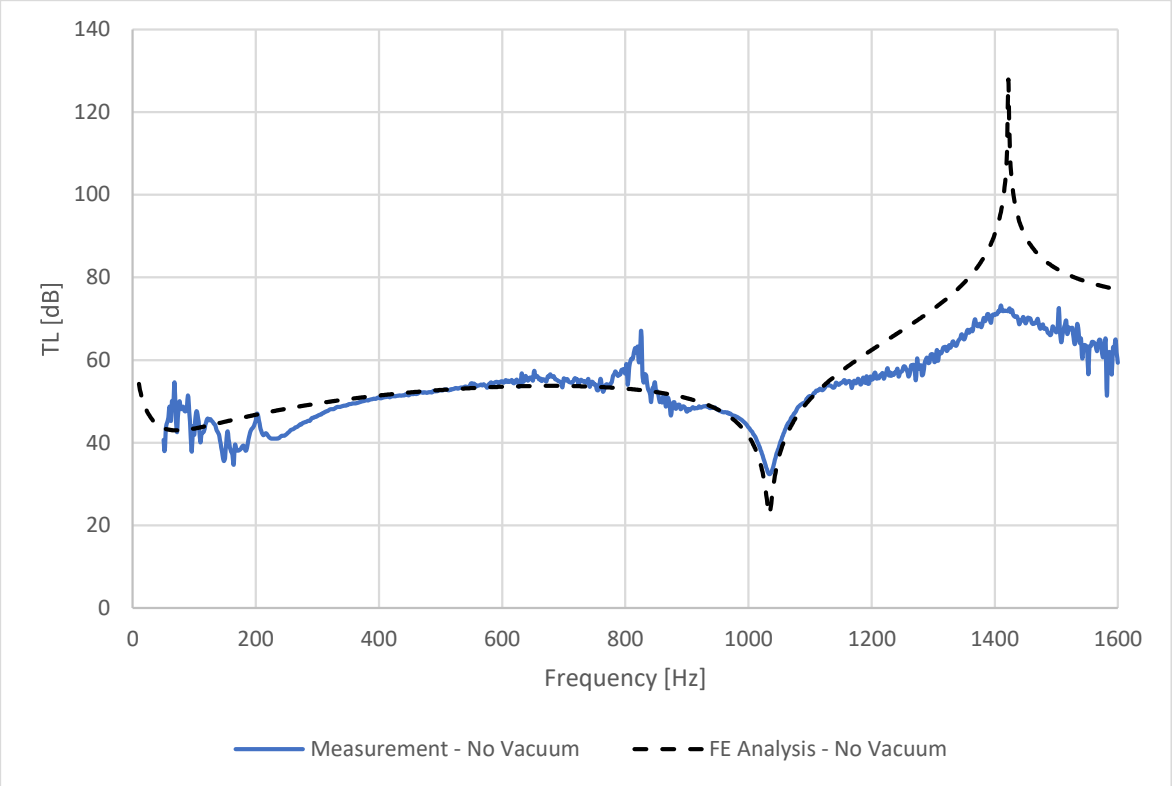


Figure 4.13. Specimen 1 no vacuum transmission loss – analysis/measurement comparison.

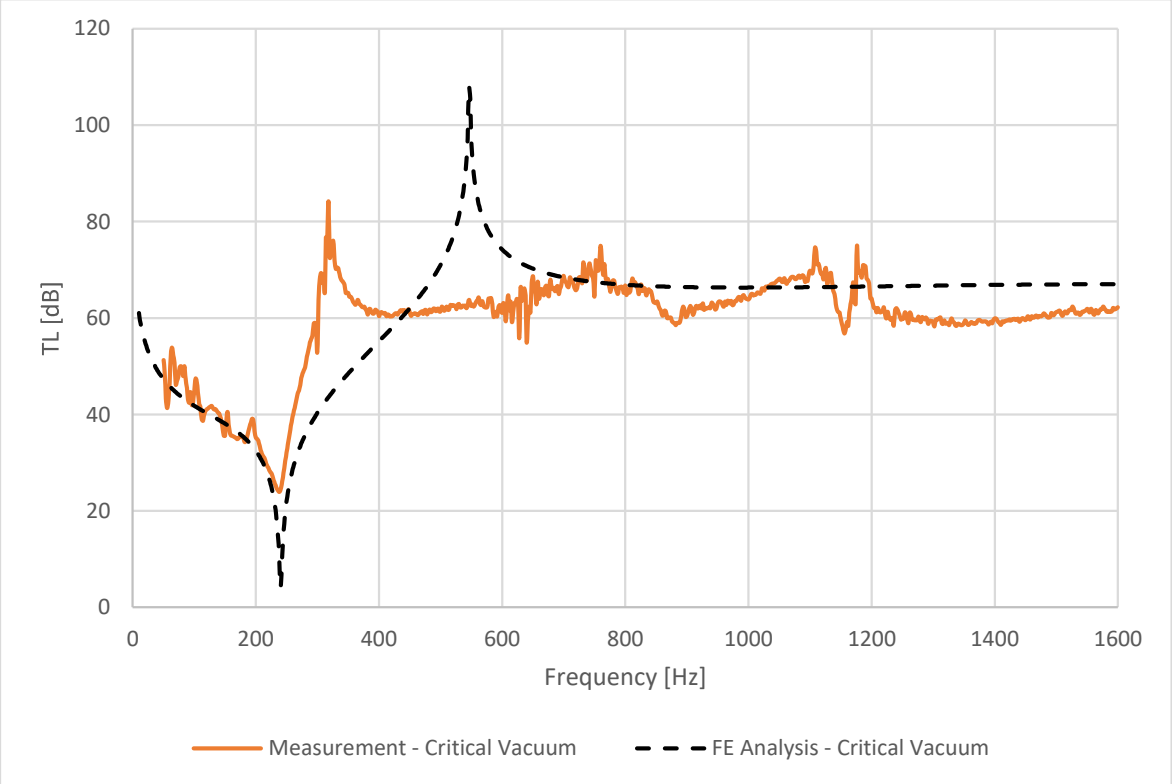


Figure 4.14. Specimen 1 critical vacuum transmission loss – analysis/measurement comparison.

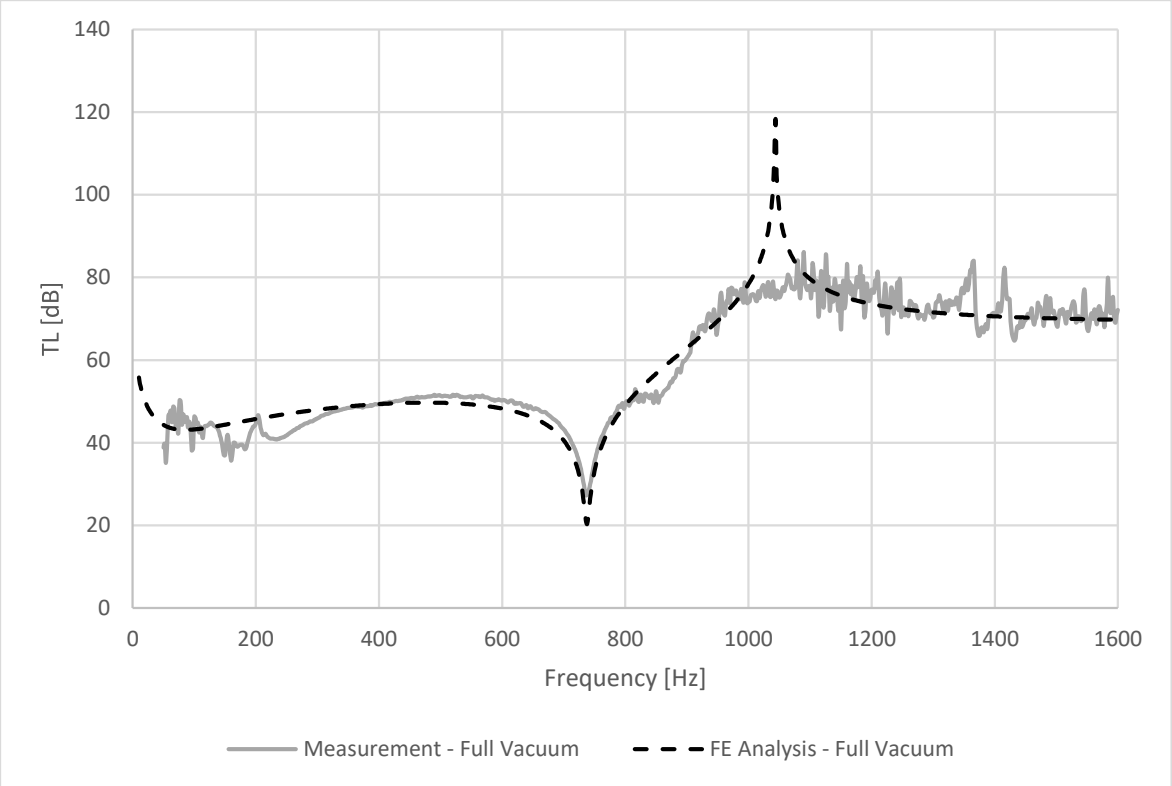


Figure 4.15. Specimen 1 full vacuum transmission loss – analysis/measurement comparison.

5. CONCLUSION

A novel sound insulation structure design is studied in this thesis. Proposed structure consists of an enclosed volume with convex shaped diaphragm. The novel design incorporates quasi-zero stiffness and vacuum (impedance mismatch), focusing mainly on low frequency sound insulation. Structure-borne and air-borne sound transmission is aimed to be reduced. Vacuum cavity is incorporated to create impedance mismatch, reducing the air-borne sound transmission. Quasi-zero stiffness behavior is utilized to obtain lowered fundamental natural frequency whilst supporting the static pressure load due to vacuum. Analytical models for double leaf partitions are investigated to estimate the effect of vacuum cavity on sound insulation capability. Lumped quasi-zero stiffness mechanism models are derived and presented. Convex shaped diaphragms are investigated and existing analytical solutions for quasi-zero stiffness behavior are studied. Then, acoustic and structural finite element studies are conducted. Lowered fundamental natural frequency is found to successfully improve transmission loss at low frequencies. Yet, vacuumed cavity only provides enhancement when flanking transmission is not present. Truncated conical and conical diaphragms are investigated for quasi-zero stiffness operation. It is found that conical diaphragms provide lower stresses at critical pressure loading level. Finally, three specimens are manufactured to experimentally validate the findings. Transmission loss measurements are carried out in an impedance tube. It is shown that when the critical vacuum level is achieved, the fundamental natural frequencies of the convex conical diaphragms significantly decrease in all three specimens. Moreover, the low frequency sound transmission loss characteristics of the specimens are improved by at least 10dB compared to the no vacuum cases. The improved low frequency response is mainly due to the quasi-zero stiffness behavior of the diaphragm. Vacuum level is shown to provide limited contribution to transmission loss due to the flanking transmission. Though increased vacuum is found to improve robustness by making the structure less susceptible to changes in environmental conditions such as temperature. As future work, diaphragm geometry and material can be altered to achieve quasi-zero stiffness at higher vacuum levels. If flanking transmission can be reduced while maintaining structural integrity and elastic deformations under high level of vacuum (preferably > 99%) the full potential of using vacuum with quasi-zero stiffness diaphragm can be unveiled.

REFERENCES

1. Occupational Safety and Health Administration, “Noise Exposure and Hearing Conservation”, 2018, https://www.osha.gov/sites/default/files/publications, accessed on January 1, 2024.

2. Özgüven, N., *Endüstriyel Gürültü Kontrolü*, TMMOB Makina Mühendisleri Odası, Ankara, 1985.

3. Standard Test Method for Laboratory Measurement of the Insertion Loss of Pipe Lagging Systems, ASTM E1222, ASTM International, Pennsylvania, 2016.

4. Measurement of Insertion Loss of Ducted Silencers Without Flow - Laboratory Survey Method, ISO 11691, BSI Standards Limited, Geneva, 2020.

5. Field Measurement of Sound Insulation in Buildings and of Building Elements, ISO 16283, BSI Standards Limited, Geneva, 2014.

6. Standard Test Method for Impedance and Absorption of Acoustical Materials Using a Tube, Two Microphones and a Digital Frequency Analysis System, ASTM E1050, ASTM International, Pennsylvania, 2019.

7. Determination of Acoustic Properties in Impedance Tubes, ISO 10534, BSI Standards Limited, Geneva, 2023.

8. Standard Test Method for Laboratory Measurement of Airborne Sound Transmission Loss of Building Partitions and Elements, ASTM E90-09, ASTM International, Pennsylvania, 2016.

9. Acoustics - Laboratory Measurement of Sound Insulation of Building Elements, ISO 10140, BSI Standards Limited, Geneva, 2021.

10. Measurement of Sound Insulation in Buildings and of Building Elements Using Sound Intensity, ISO 15186, BSI Standards Limited, Geneva, 2000.

11. Bies, D. A. and C. H. Hansen, *Engineering Noise Control Theory and Practice*, Fourth Edition, Spon Press, Abingdon, 2009.

12. Long, M., *Architectural Acoustics*, Elsevier, San Diego, 2005.

13. Kim, Y. H., *Sound Propagation: an Impedance Based Approach*, John Wiley & Sons, Noida, 2010.

14. Patil, A. R. and G. M. Goetchius, "Effect of Damping on Sound Transmission Loss Through Automotive Body Panels", *Proceedings of the 2009 SAE Noise and Vibration Conference*, Illinois, USA, p. 2009-01-2202, 2009.

15. Huang, S., Y. Li, J. Zhu and D. P. Tsai, "Sound-Absorbing Materials", *Physical Review Applied*, Vol. 20, No. 1, p. 010501, 2023.

16. Lee, F. C. and W. H. Chen, "Acoustic Transmission Analysis of Multi-Layer Absorbers", *Journal of Sound and Vibration*, Vol 284, No. 2, pp. 612-634, 2001.

17. Gulia, P. and A. Gupta, "Enhancing the Sound Transmission Loss Through Acoustic Double Panel Using Sonic Crystal and Porous Material", *The Journal of the Acoustical Society of America*, Vol 144, No. 3, pp. 1435-1442, 2018.

18. Chiang, Y. K. and Y. S. Choy, "Acoustic Behaviors of the Microperforated Panel Absorber Array in Nonlinear Regime Under Moderate Acoustic Pressure Excitation", *The Journal of the Acoustical Society of America*, Vol. 143, No. 1, pp. 538-549, 2018.

19. Ning, J. F., S. W. Ren and G. P. Zhao, "Acoustic Properties of Micro-Perforated Panel Absorber Having Arbitrary Cross-Sectional Perforations", *Applied Acoustics*, Vol. 111, pp. 135-142, 2016.

20. Romero-García, V., G. Theocharis, O. Richoux, A. Merkel, V. Tournat and V. Pagneux, "Perfect and Broadband Acoustic Absorption by Critically Coupled Subwavelength Resonators", *Scientific Reports*, Vol. 6, No. 1, p. 19519, 2016.

21. Wang, Y., H. Zhao, H. Yang, J. Zhong, D. Zhao, Z. Lu and J. Wen, "A Tunable Sound-Absorbing Metamaterial Based on Coiled-Up Space", *Journal of Applied Physics*, Vol. 123, No. 18, p. 185109, 2018.

22. Kurtze, G. and B. G. Watters, "New Wall Design for High Transmission Loss or High Damping", *The Journal of the Acoustical Society of America*, Vol. 31, No. 6, pp. 739-748, 1959.

23. Moore, J. A. and R. H. Lyon, "Sound Transmission Loss Characteristics of Sandwich Panel Constructions", *The Journal of the Acoustical Society of America*, Vol. 89, No. 2, pp. 777-791, 1991.

24. Isaac, C. W., M. Pawelczyk and S. Wrona, "Comparative Study of Sound Transmission Losses of Sandwich Composite Double Panel Walls", *Applied Sciences*, Vol. 10, No. 4, p. 1543, 2020.

25. Sergio, P., C. Fernando, F. Raul, R. Sohel and P. Fernando, "Acoustical Behavior of Hybrid Composite Sandwich Panels", *Key Engineering Materials*, Vol. 634, pp 455-464, 2014.

26. Proença, M., A. Neves e Sousa, M. Garrido and J. R. Correia, "Acoustic Performance of Composite Sandwich Panels for Building Floors: Experimental Tests and Numerical-Analytical Simulation", *Journal of Building Engineering*, Vol. 32, No. 5, p. 101751, 2020.

27. Birman, V. and G. A. Kardomatea, "Review of Current Trends in Research and Applications of Sandwich Structures", *Composites Part B*, Vol.142, No. 3, pp. 221-240, 2018.

28. Wan, Z., L. Yaoguang, X. Chen, H. Wu, F. Yin, R. Gao, Y. Li and T. Zhao, "Experimental and Numerical Investigations of the Vibration and Acoustic Properties of Corrugated Sandwich Composite Panels", *Applied Sciences*, Vol. 12, No. 17, p. 8553, 2022.

29. S. J. Robinson and R. E. Collins, "Evacuated Windows – Theory and Practice", *ISES Solar World Congress*, Kobe, 1989.

30. Glass in Building – Vacuum Insulating Glass, ISO 19916, BSI Standards Limited, Geneva, 2018.

31. Lux, C., B. Nusser and P. Schober, "Experimental Investigations on Airborne Sound Insulation of Vacuum Insulating Glazing (VIG)", *INTER-NOISE and NOISE-CON Congress and Conference Proceedings*, South Korea, Seoul, Vol. 261, No. 5, pp. 1412-1423, 2020.

32. Ashmore, N., C. Densil and C. Kocer, "Acoustic Properties of Vacuum Insulating Glazing", *Australian Acoustical Society, Acoustics 2015*, Australia, Hunter Valley, pp. 1-9. 2015.

33. Nugroho, A. C., D. Cabrera and C. Kocer, "Improving the Airborne Sound Insulation Properties of Vacuum Insulating Glazing Using Dissimilar Pane Thickness and a Laminated Pane: Experimental Results", *Journal of Physics: Conference Series*, Vol. 1075, No. 1, p. 012063, 2017.

34. Collins, R. E., G. M. Turner, A. C. Fischer-Cripps, J. Z. Tang, T. M. Simko, C. J. Dey, D. A. Clugston, Q. C. Zhang and J. D. Garrison, "Vacuum Glazing—A New Component for Insulating Windows". *Building and Environment*, Vol 30, No. 4, pp 459-492, 1995.

35. Cauberg, J. J. M. and M. J. Tenpierik, "Sound Reduction of Vacuum Insulation Based Building Panels", *19th International Congress on Acoustics,* Madrid, Spain, pp. 1-6. 2007.

36. Maysenholder, W., “Sound Transmission Loss of Vacuum Insulation Panels”, *Journal of the Acoustical Society of America*, Vol. 123, No. 5, p. 3815, 2008.

37. Walters, S. and S. Dance, “Noise Control Potential of Vacuum Isolation Panels”, In *INTER-NOISE and NOISE-CON Congress and Conference Proceedings*, Australia, Melbourne, Vol. 249, No. 8, pp. 1-10. 2014.

38. Rickards, M. J., “Braced Sound Barrier Vacuum Panel”, U.S. Patent 20080289898 A1, November 27, 2008. Available: https://patents.google.com/patent/US20080289898A1, accessed on January 1, 2024.

39. Rickards, M. J. “Thermoacoustic Barrier Vacuum Panel”, U.S. Patent 20090162599 A1, June 25, 2009. Available: https://patents.google.com/patent/US20090162599A1, accessed on January 1, 2024.

40. Molyneux, W. G., "Supports for Vibration Isolation", *Aeronautical Research Council Current Papers*, Vol. 332, p. 19022, 1957.

41. Carrella, A., M. J. Brennan and T. P. Waters, "Optimization of a Quasi-Zero-Stiffness Isolator", *Journal of Mechanical Science and Technology*, Vol. 21, pp. 946-949, 2007.

42. Qiu, J., J. H. Lang and A. H. Slocum, "A Curved-Beam Bistable Mechanism", *Journal of Microelectromechanical Systems*, Vol. 13, No. 2, pp. 137-146, 2004.

43. Platus, D. L., "Negative- Stiffness- Mechanism Vibration Isolation Systems", *SPIE Conference on Current Developments in Vibration Control for Optomechanical Systems*, Denver, pp. 98-105, 1999.

44. Ye, K., J. C. Ji and T. Brown, "Design of a Quasi-Zero Stiffness Isolation System for Supporting Different Loads", *Journal of Sound and Vibration*, Vol. 471, p. 115198, 2020.

45. Li, Y. and D. Xu, "Vibration Attenuation of High Dimensional Quasi-Zero Stiffness Floating Raft System", *International Journal of Mechanical Sciences*, Vol. 126, pp. 186-195, 2017.

46. Wang, K., J. Zhou, Y. Chang, H. Ouyang, D. Xu and Y. Yang, "A Nonlinear Ultra-Low Frequency Vibration Isolator with Dual Quasi-Zero-Stiffness Mechanism", *Nonlinear Dynamics*, Vol. 101, pp 755–773, 2020.

47. Zhou, J., K. Wang, D. Xu, H. Ouyang and Y. Fu, "Vibration Isolation in Neonatal Transport by Using a Quasi-Zero-Stiffness Isolator", *Journal of Vibration and Control*, Vol. 24, No. 15, pp. 3278-3291, 2017.

48. Ma, Z., R. Zhou and Q. Yang, "Recent Advances in Quasi-Zero Stiffness Vibration Isolation Systems: An Overview and Future Possibilities", *Machines*, Vol. 10, No. 9, p. 813, 2022.

49. Kocak, K. and C. Yilmaz, "Design of a Compliant Lever-Type Passive Vibration Isolator with Quasi-Zero-Stiffness Mechanism", *Journal of Sound and Vibration*, Vol. 558, p. 117758, 2023.

50. Meng, Q., X. Yang, W. Li, E. Lu and L. Sheng, "Research and Analysis of Quasi-Zero-Stiffness Isolator with Geometric Nonlinear Damping", *Shock and Vibration*, Vol. 2017, pp. 1-9, 2017.

51. Zhou, J., H. Pan, C. Cai and D. Xu, "Tunable Ultralow Frequency Wave Attenuations in One-Dimensional Quasi-Zero-Stiffness Metamaterial", *International Journal of Mechanics and Materials in Design*, Vol. 17, pp. 285-300, 2021.

52. Zhang, Q., D. Guo and G. Hu, "Tailored Mechanical Metamaterials with Programmable Quasi-Zero-Stiffness Features for Full-Band Vibration Isolation", *Advanced Functional Materials*, Vol. 31, No. 33, p. 2101428, 2021.

53. Fan, H., L. Yang, Y. Tia and Z. Wang, "Design of Metastructures with Quasi-Zero Dynamic Stiffness for Vibration Isolation", *Composite Structures*, Vol. 243, p. 112244, 2020.

54. Paradeisiotis, A., M. Kalderon and I. Antoniadis, "Advanced Negative Stiffness Absorber for Low-Frequency Noise Insulation of Panels", *AIP Advances*, Vol. 11, No. 6, p. 065003, 2021.

55. Wang, D., Q. Zhang and G. Hu, "Low Frequency Waterborne Sound Insulation Based on Sandwich Panels with Quasi-Zero-Stiffness Truss Core", *Journal of Applied Mechanics*, Vol. 90, No. 3, p. 031006, 2022.

56. Skakoon, J., "Self-Help", *Mechanical Engineering Magazine Select Articles*, Vol. 145, No. 3, pp. 46-49, 1998.

57. Kinsler, L. E., A. R. Frey, A. B. Coppens and J. V. Sanders, *Fundamentals of Acoustics*, Fourth Edition, John Wiley & Sons, Venice, 2000.

58. Reynolds, D. D., *Engineering Principles of Acoustics: Noise and Vibration Control*, Allyn and Bacon, Boston, 1981.

59. Trevathan, J. W. and J. R. Pearse, "Resonant and Non-Resonant Sound Transmission through a Finite Panel", *Building Acoustics*, Vol. 13, No. 1, pp. 13-22, 2006

60. London, A., "Transmission of Reverberant Sound Through Double Walls", *The Journal of the Acoustical Society of America*, Vol. 22, No. 2, pp. 270-279, 1950

61. Inman, D., J., *Engineering Vibration*, Fourth Edition, Pearson, Englewood Cliffs, 2014.

62. Robertson, W. S. P., B. Cazzolato and A. Zander, "Planar Analysis of a Quasi-Zero Stiffness Mechanism Using Inclined Linear Springs", *Proceedings of Acoustics 2013 – Victor Harbor*, Australia, pp. 1-6, 2013.

63. Giovanni, D., *Flat and Corrugated Diaphragm Design Handbook*, Routledge, New York, 1982.

64. Hu, N. and R. Burgueño, " Buckling-Induced Smart Applications: Recent Advances and Trends", *Smart Materials and Structures*, Vol 24, No. 6, p. 063001, 2015.

APPENDIX A: SOUND TRANSMISSON LOSS MEASUREMENT CURVES

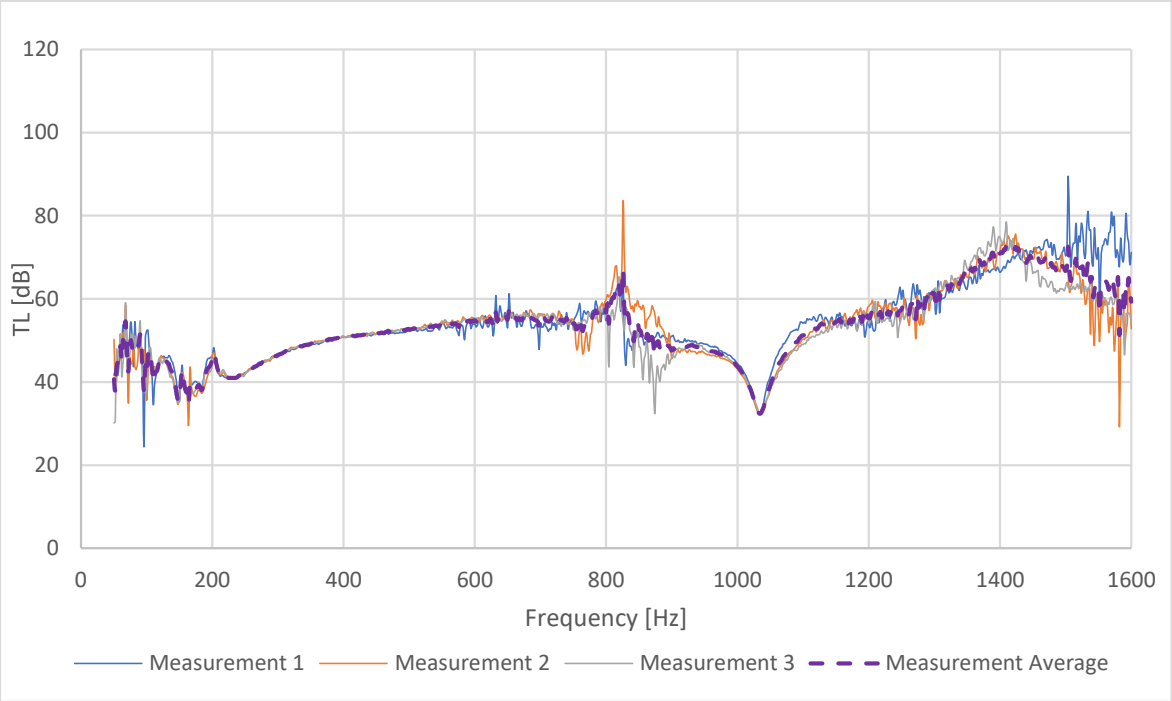


Figure A. 1. Transmission loss measurements of Specimen 1 – no vacuum.

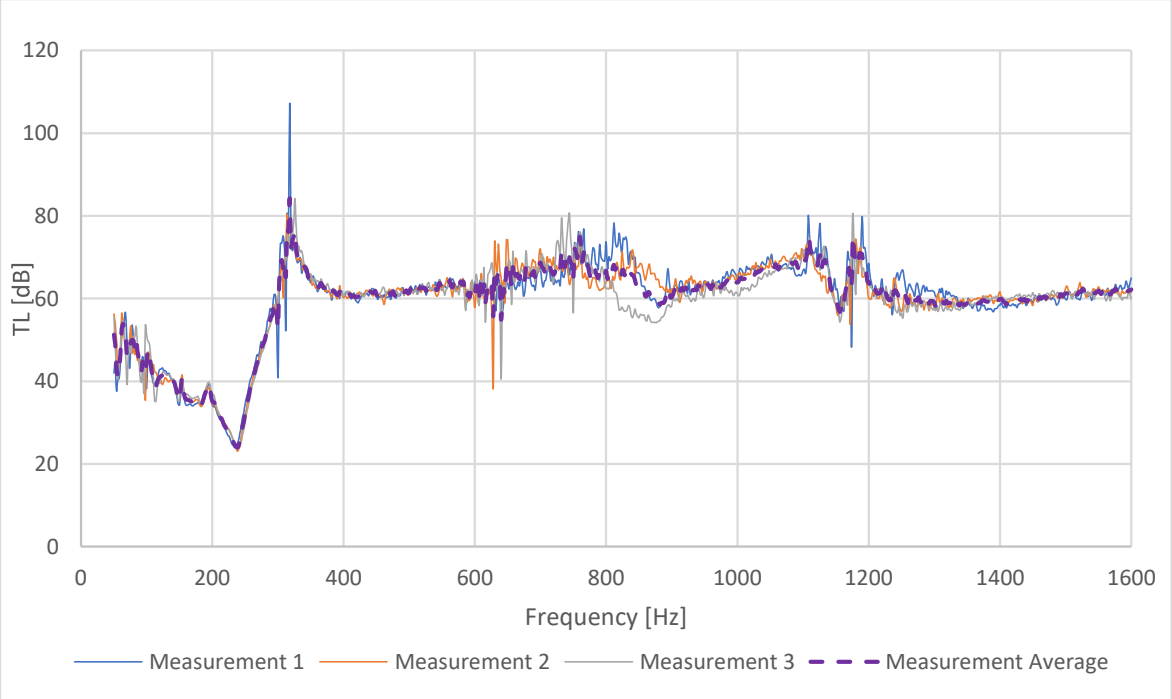


Figure A. 2. Transmission loss measurements of Specimen 1 – critical vacuum.

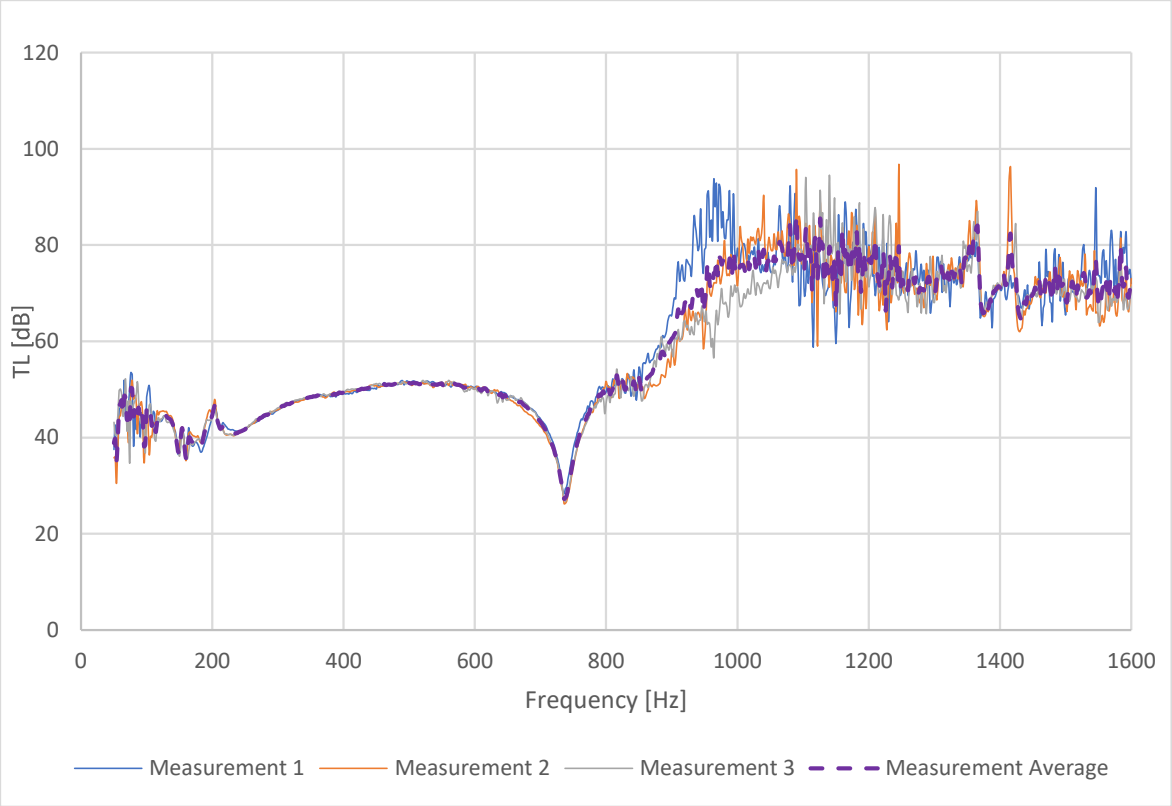


Figure A. 3. Transmission loss measurements of Specimen 1 – full vacuum.

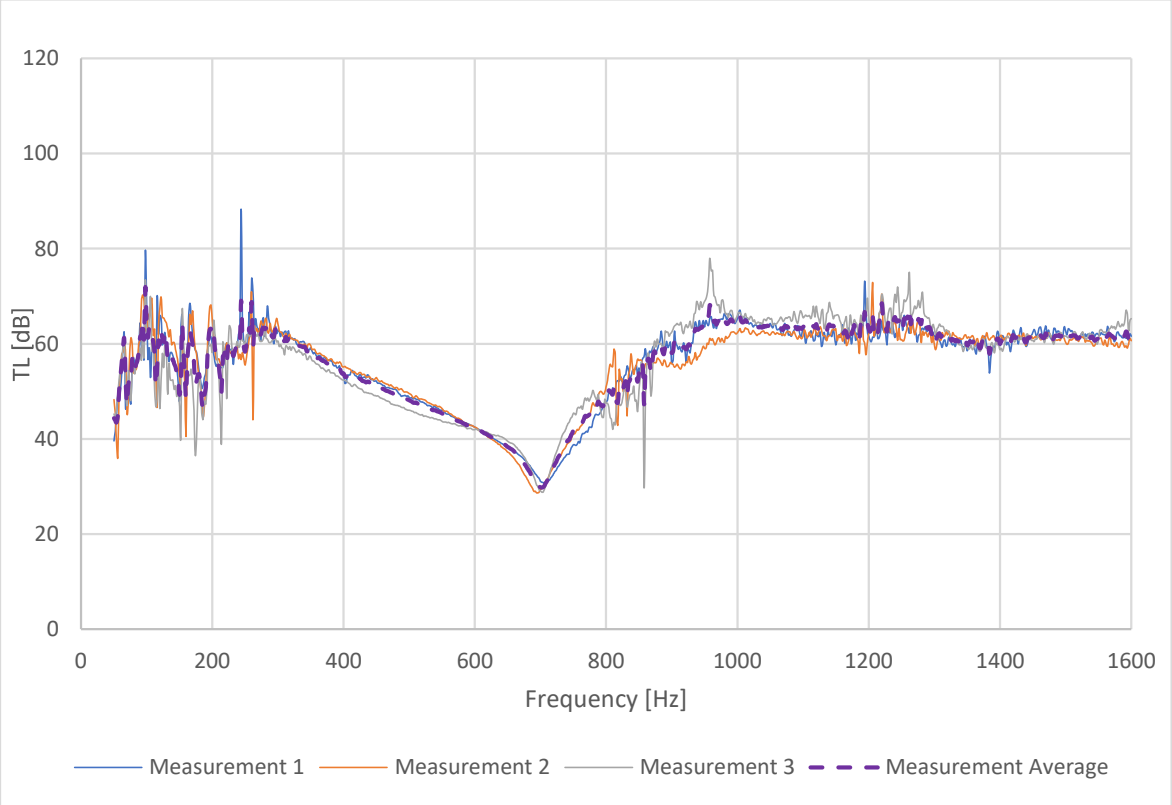


Figure A. 4. Transmission loss measurements of Specimen 2 – no vacuum.

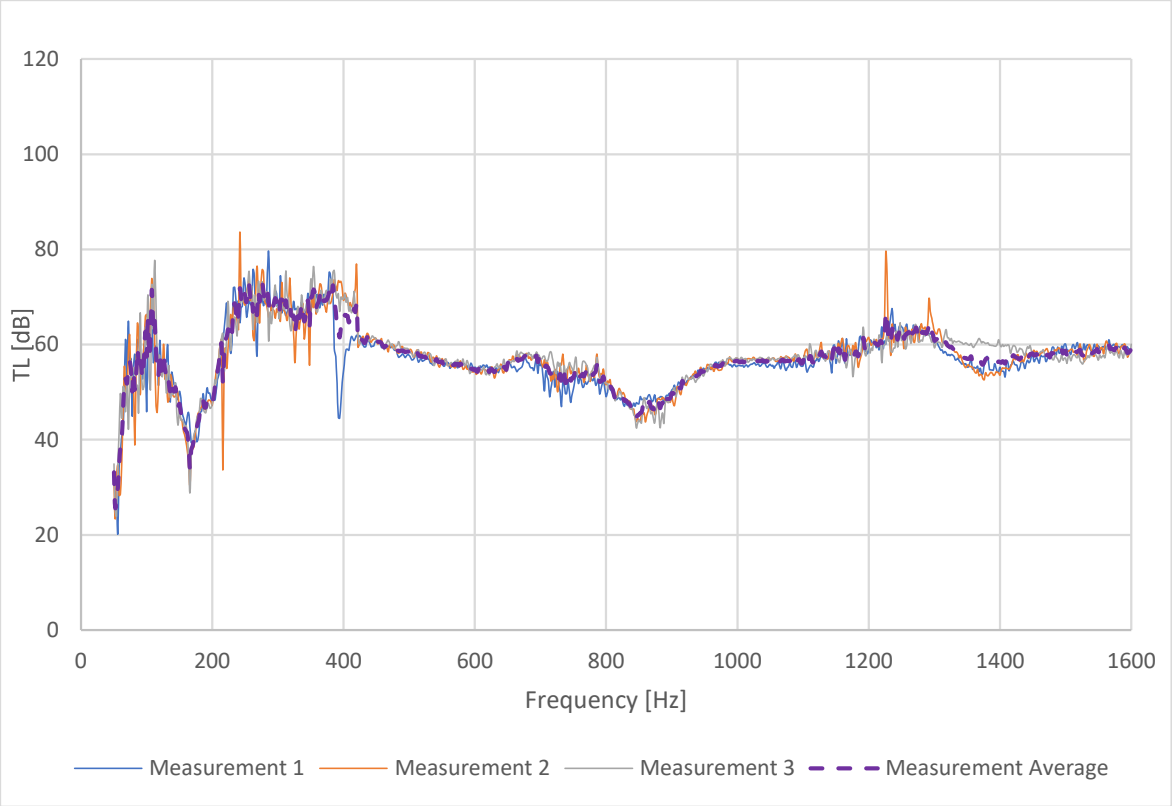


Figure A. 5. Transmission loss measurements of Specimen 2 – critical vacuum.

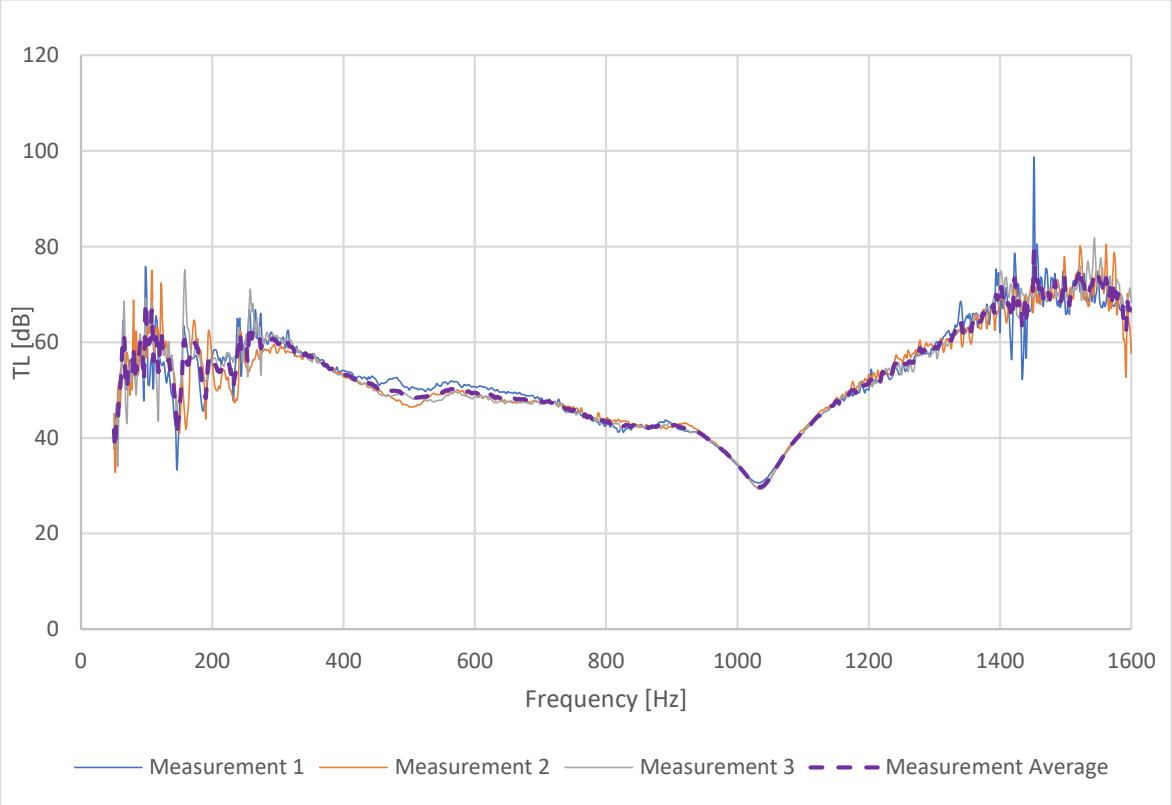


Figure A. 6. Transmission loss measurements of Specimen 2 – full vacuum.

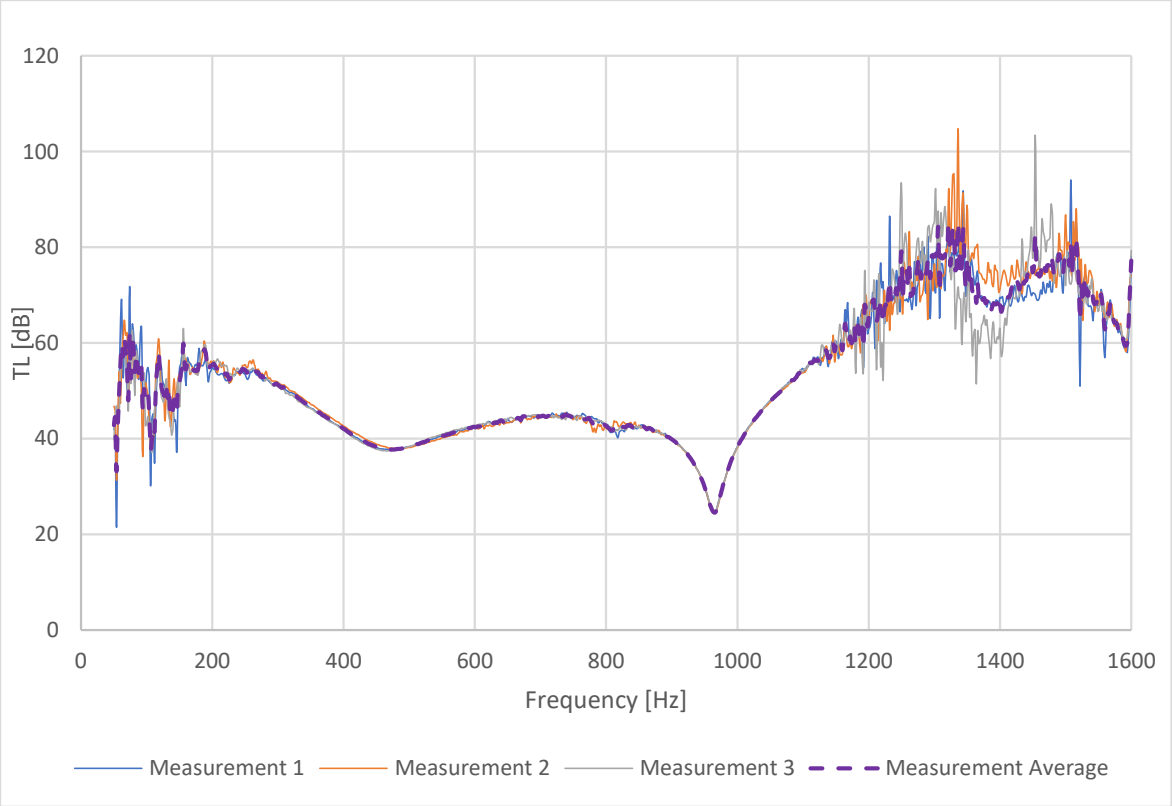


Figure A. 7. Transmission loss measurements of Specimen 3 – no vacuum.

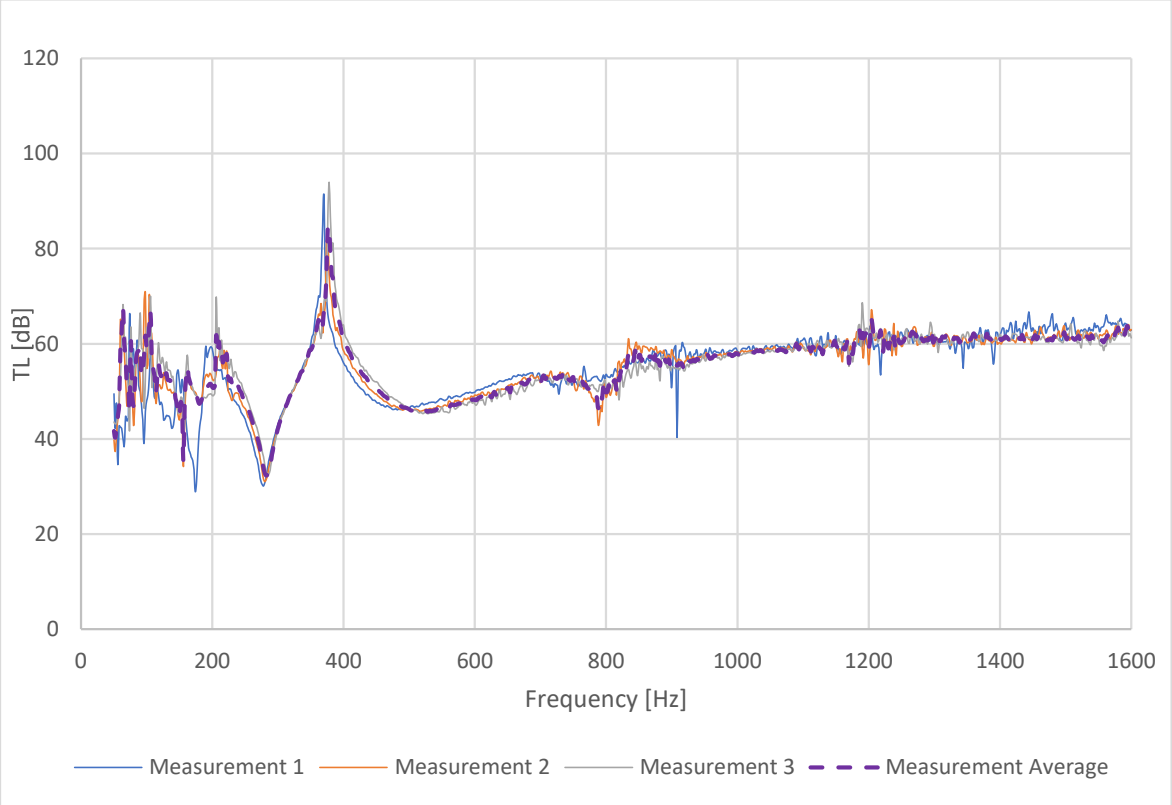


Figure A. 8. Transmission loss measurements of Specimen 3 – critical vacuum.

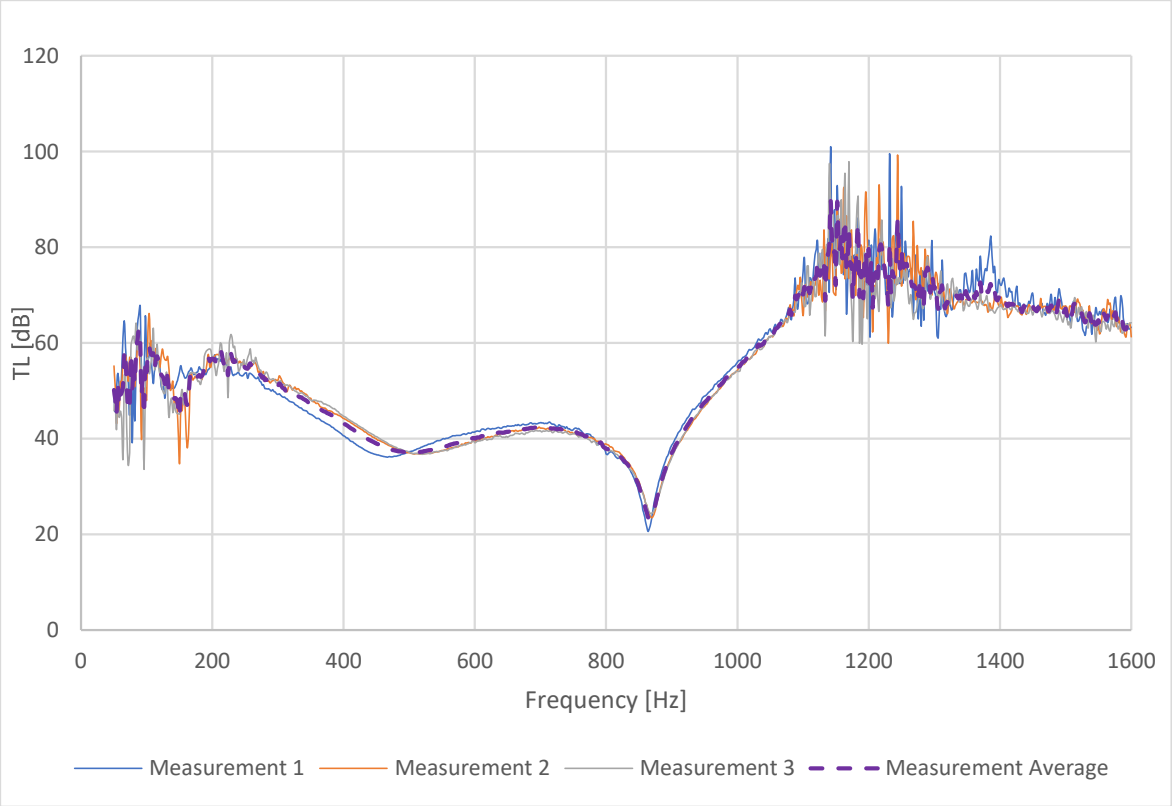


Figure A. 9. Transmission loss measurements of Specimen 3 – full vacuum.